

**The Plasma Physics Processes that Drive Ring Current Enhancements  
during Geomagnetic Storms and Substorms**

Michele Diane Cash

A dissertation  
submitted in partial fulfillment of the  
requirements for the degree of

Doctor of Philosophy

University of Washington

2012

Robert M. Winglee, Co-Chair

Erika M. Harnett, Co-Chair

Michael Mc Carthy

Program Authorized to Offer Degree:  
Department of Earth and Space Sciences



University of Washington

**Abstract**

The Plasma Physics Processes that Drive Ring Current Enhancements  
during Geomagnetic Storms and Substorms

Michele Diane Cash

Chairs of the Supervisory Committee:  
Professor Robert Winglee  
Professor Erika Harnett  
Department of Earth and Space Sciences

Geomagnetic storms result when energetic particles of solar and ionospheric origin fill Earth's inner magnetosphere and create a strong westward current, known as the ring current. This dissertation presents results from investigating the plasma dynamics that contribute to the development of Earth's ring current from ionospheric outflow of  $H^+$  and  $O^+$  ions, and the role of ring current enhancements in the generation of geomagnetic storms and substorms. Modeling was carried via a combined multifluid and particle approach, which enables us to resolve the small-scale dynamics that are key to particle energization within the context of the global magnetosphere. The results presented in this dissertation substantially contribute to our understanding of the development and composition of the ring current during geomagnetic storms and substorms, and offer insight into the ionospheric sources regions for ring current ions, as well as the processes through which these particles are energized, injected, and trapped within the inner magnetosphere.

This thesis presents results that show how small-scale particle dynamics within the current sheet, boundary layers, and reconnection regions drive the acceleration of ring current particles within the larger global context of the magnetosphere. Small-scale structures within the magnetotail are shown to be more important in determining when particles are accelerated than the time after particles are initialized in the ionosphere. It is also found that after a period of southward IMF, in which particle energization is observed, a northerly turning of the IMF is necessary in order to trap energetic particles in orbit around

the Earth and form a symmetric ring current. Asymmetries in the acceleration mechanisms between ionospheric  $H^+$  and  $O^+$  ions were observed with oxygen ions convecting duskward according to the cross-tail current and gaining more energy than protons, which moved earthward on reconnecting field lines and were accelerated closer to the plasma sheet inner boundary.

# TABLE OF CONTENTS

<b>LIST OF FIGURES</b>	<b>iii</b>
<b>LIST OF TABLES</b>	<b>v</b>
<b>Chapter 1: Introduction</b>	<b>1</b>
1.1 Introduction to Solar-Terrestrial Physics .....	3
1.1.1 Solar Wind .....	4
1.1.2 Interplanetary Magnetic Field.....	5
1.1.3 Magnetosphere.....	5
1.1.4 Ionosphere.....	8
1.1.5 Current Systems.....	10
1.2 Magnetospheric Storms and Substorms .....	11
1.3 Scope of Dissertation .....	14
<b>Chapter 2: The Ring Current</b>	<b>17</b>
2.1 Previous Modeling and Open Questions.....	18
2.2 Questions to be Addressed .....	24
<b>Chapter 3: Numerical Methods</b>	<b>26</b>
3.1 Multifluid Model.....	26
3.2 Particle Tracking .....	29
<b>Chapter 4: Ring Current Formation during Substorm Conditions</b>	<b>31</b>
4.1 Overview .....	32
4.2 Boundary and Initial Conditions .....	32
4.2.1 Particle Initialization.....	34
4.3 Particle Energization .....	35
4.4 Northward Turning of IMF .....	45
4.5 Resolving the Thin Current Sheet .....	50
4.6 Calculated Particle Flux .....	54
4.7 Summary .....	58
<b>Chapter 5: Storm Time Production of Ring Current Ions</b>	<b>60</b>
5.1 Overview .....	61
5.2 Boundary and Initial Conditions .....	62
5.3 Energization and Trapping of Ring Current Ions.....	65
5.4 Relative Contribution of Ionospheric Source Regions.....	72
5.5 Energy Density Contribution from $H^+$ and $O^+$ .....	81
5.6 Summary .....	86
<b>Chapter 6: Importance of Temperature Anisotropies in Ring Current Development</b>	<b>89</b>
6.1 Overview .....	89
6.2 Motivation .....	90
6.3 Comparison of Temperature Anisotropies .....	91
6.3.1 Particle Initialization.....	92
6.3.2 Moments of the Ion Distribution Function.....	93
6.4 Results .....	94
6.5 Summary .....	106

<b>Chapter 7: Space Weather Implications for Extrasolar Planets</b>	<b>109</b>
7.1 Overview.....	109
7.2 Background.....	110
7.2.1 EGP Detection Methods.....	110
7.2.2 Planetary Magnetic Fields.....	110
7.2.3 Future of EGP Characterization.....	112
7.2.4 UV Stellar Continuum.....	112
7.3 Auroral Emission from EGPs.....	113
7.3.1 Solar System Analogues: Jupiter as a Template.....	113
7.3.2 Sample of EGPs.....	114
7.4 Parameters and Assumptions.....	117
7.4.1 Known Planetary Parameters.....	117
7.4.2 Unknown Planetary Parameters.....	117
7.4.3 Known Stellar Parameters.....	119
7.4.4 Unknown Stellar Parameters.....	119
7.5 Predictive Model.....	123
7.5.1 Planetary Magnetic Dipole Moment.....	123
7.5.2 Magnetopause Distance.....	125
7.5.3 Stellar Wind Power.....	126
7.5.4 Auroral Brightness.....	127
7.5.5 Integrated Flux.....	128
7.5.6 Contrast Ratio.....	129
7.6 Observing Auroral Emissions.....	129
7.6.1 UV Auroral Emissions.....	130
7.6.2 Current and Future UV Instruments.....	132
7.7 Results.....	135
7.7.1 The UV Advantage.....	139
7.7.2 Detecting a Solar System Analogue.....	140
7.8 Discussion and Conclusions.....	141
7.8.1 Model limitations.....	143
7.8.2 Future Observing Prospects.....	144
<b>Chapter 8: Summary and Future Work</b>	<b>145</b>
8.1 Summary of Major Findings.....	145
8.2 Recommendations for Future Work.....	149
<b>Bibliography</b>	<b>151</b>

## LIST OF FIGURES

	Page
Figure 1.1 The solar-terrestrial system.....	3
Figure 1.2 Cross-section view of Earth's magnetosphere.....	6
Figure 1.3 Atmospheric profile for neutral gas and for ionized gas. ....	9
Figure 1.4 Daytime ionospheric and atmospheric composition.....	10
Figure 1.5 Three-dimensional cutaway view of the magnetosphere.....	11
Figure 1.6 Graphical representation of the ring current.....	13
Figure 1.7 Example of a typical depression in Earth's surface magnetic field.....	14
Figure 4.1 Time evolution of a single injection of $O^+$ ions.....	37
Figure 4.2 High-resolution image of Figure 4.1c.....	38
Figure 4.3 Hall component of the electric field.....	41
Figure 4.4 Time evolution of a single injection of $H^+$ .....	42
Figure 4.5 Time evolution of down tail region.....	44
Figure 4.6 Velocity flow vectors for $H^+$ and $O^+$ fluids from the multifluid model.....	45
Figure 4.7 Time evolution for the case when IMF is southward for the entire run.....	46
Figure 4.8 Time evolution of ionospheric for case when IMF turns northward.....	48
Figure 4.9 Comparison of high resolution vs. low resolution.....	49
Figure 4.10 Hall component of the electric field with low resolution.....	51
Figure 4.11 Comparison of high resolution vs. low resolution with time.....	52
Figure 5.1 Evolution of the magnetic field and outflowing oxygen ions.....	63
Figure 5.2 Solar wind conditions on 10 March 1998.....	64
Figure 5.3 Parameters used to monitor conditions for the 10 March 1998 storm.....	66
Figure 5.4 Foot point mapping of ring current ions mapped back to the polar cap.....	67
Figure 5.5 Results for hydrogen and oxygen ions for the main phase of the storm.....	68
Figure 5.6 Results for oxygen ions during the smaller decrease in <i>Dst</i> .....	73
Figure 5.7 Results for hydrogen ions during the smaller decrease in <i>Dst</i> .....	74
Figure 5.8 Results for oxygen during the main phase of the storm.....	77
Figure 5.9 Results for hydrogen ions during the main phase of the storm.....	78
Figure 5.10 $O^+$ contribution to the ring current from five ionospheric outflow regions.....	82
Figure 5.11 $H^+$ contribution to the ring current from five ionospheric outflow regions.....	83
Figure 5.12 Ring current energy density contribution from $H^+$ and $O^+$ .....	84
Figure 6.1 Density plots from the isotropic and anisotropic multifluid codes.....	95
Figure 6.2 Pressure plots from the isotropic and anisotropic multifluid codes.....	96
Figure 6.3 Temperature anisotropy plots in <i>x</i> , <i>y</i> , and <i>z</i> directions for hydrogen ions.....	99
Figure 6.4 Temperature anisotropy plots in <i>x</i> , <i>y</i> , and <i>z</i> directions for oxygen ions.....	100
Figure 6.5 Temperature anisotropies for hydrogen ions.....	102
Figure 6.6 Pitch angle distribution for hydrogen ions in the ring current.....	103
Figure 6.7 Temperature anisotropies for oxygen ions.....	104
Figure 6.8 Pitch angle distribution for oxygen ions in the ring current.....	105
Figure 7.1 Planetary magnetic moment for 6 bodies in our solar system.....	124

Figure 7.2 Spectrum of Jupiter's aurora in the UV .....	131
Figure 7.3 Integrated system throughput for SBC/PR110LP .....	134
Figure 7.4 COS FUV effective areas and throughputs .....	135

## LIST OF TABLES

	Page
Table 1-1 Observed properties of the solar wind near the orbit of Earth.....	4
Table 1-2 Typical near-tail plasma and field parameters.....	7
Table 4-1 Simulation results obtained at 0310 UT.....	56
Table 7-1 Values for the extrasolar planets of interest.....	115
Table 7-2 Stars hosting extrasolar planets.....	116
Table 7-3 Planetary parameters of interest for known extrasolar planets.....	116
Table 7-4 Stellar parameters of interest for stars known to host extrasolar planets.....	122
Table 7-5 Scaling laws for calculating planetary magnetic dipole moment.....	124
Table 7-6 Predicted stellar wind power for selected EPGs.....	127
Table 7-7 UV auroral emission in the Werner Band.....	137
Table 7-8 UV auroral emission in the Lyman Band.....	138
Table 7-9 Detecting a solar system analogue at various distances from Earth.....	140
Table 7-10 Time required to collect 1,000 photons using the JWST.....	141
Table 7-11 Time required to collect 1,000 photons from several known EPGs.....	142

## ACKNOWLEDGEMENTS

The research presented in this thesis was supported by several grants and fellowships including NSF IGERT Grants No. DGE-0504219 and No. DGE-9870713 through the Astrobiology Program at the University of Washington, Seattle. Additional funding was supplied by the NVIDIA Innovation Fellowship (2008-2009), Howard A. Coombs Fellowship (2010), Marie Farrel Endowment (2011), and NASA Earth and Space Sciences Fellowship Grant No. NNX11AP80H (2011-2012). NASA Grants No. NNX10AK96G and No. NNX07AP66G and NSF Grant No. 0617654 also supported sections of the research presented in this dissertation.

I also would like to acknowledge the people who helped make this research possible. This research could not have been accomplished without resources and guidance provided by my advisors: Professor Robert Winglee and Professor Erika Harnett. For their support and encouragement over the past five years, I would also like to thank my fellow graduate students; in particular, I would like to acknowledge the following people: Aariah Kidder, Breanyn MacInnes, Cihan Akcay, and Charlotte Christensen. For their help on the work presented in Chapter 7, I would like to acknowledge the following people: Professor Eric Agol, Professor Walt Harris, Dr. Glida Ballester, and Dr. Lotfi Ben-Jaffel.

I would especially like to thank my parents, Norman and Theresa Cash, who helped foster and guided my interest in science and experimentation from an early age, teaching me to explore and question. Finally, I would like to thank my fellow physicist and husband, Jonathan Wrobel, for his unwavering support, guidance, and understanding. He has taught me that anything is possible with enough planning, creativity, organization and determination.

## Chapter 1: Introduction

The space environment is dominated by plasma, consisting of energetic charged particles that move through space under the influence of electric and magnetic fields. While near the surface of our planet matter tends to be in a solid, liquid, or gaseous state, the vast majority of the universe by volume (>99.9%) is comprised of plasma, which is an electrically neutral, highly ionized gas composed of roughly equal numbers of ions and electrons. As humans venture away from the neutral surface of the Earth, we are immersed in a highly dynamic and complex environment filled with ionized particles that are moving, flowing, and reacting to the constant and ever-changing electric and magnetic fields that fill the voids of space.

The existence of space plasmas and their dynamic nature creates what is known as *space weather*, activity in Earth's near-space environment that has been affecting man-made technological systems since the advent of electricity-based technology [Bothmer and Daglis, 2007]. In modern times, space weather has become increasingly problematic with our enhanced reliance on satellites and space-based systems [Choi et al., 2011]. Rapid and intense fluctuations in the space climate result in severe space weather or space storms. Such *geomagnetic storms*, as they are called, can significantly impact society both economically and socially through effects on space-borne assets, as well as effects on Earth-bound equipment and infrastructure.

There are two mechanisms through which geomagnetic storms present hazards. First, there are the effects due to the energetic particles themselves, which primarily affect objects in orbit. These particles can damage spacecraft solar panels, cause electrical charging of the spacecraft, and shorten satellite operational lifetimes [Brautigam, 2002]. Intense radiation doses can also cause biological damage in astronauts via genetic mutations, increased risk of cancer and early death. Second, there are the effects due to geomagnetically induced currents (GICs), which are large-scale currents induced by the changing surface magnetic

field that result during geomagnetic storms. Thus, satellites in space are not the only technological systems to be affected by the fluctuating conditions in Earth's near-space environment; ground-based systems such as power grids, oil lines, and natural gas pipelines can be affected by space weather as well.

The severity of space weather effects depends on the strength of the geomagnetic storm. Minor storms are common, resulting in increased auroral displays and radio propagation interference. Larger storms, while occurring less frequently, have the potential for more serious consequences due to the inter-connectedness of present-day infrastructure. An example of the social and economic impact of large-scale GICs is the 13 March 1989 geomagnetic storm that left six million people in Quebec without power for nine hours and resulted in significant economic loss [*Bothmer and Daglis, 2007*].

The above examples are just some of the reasons why we want to better understand space weather and geomagnetic storms. As we increasingly rely on modern infrastructure susceptible to space weather effects and as we continue to expand our human presence in space, a comprehensive understanding of space weather becomes progressively more important. In order to protect ourselves from space weather hazards, we need to further develop our understanding of the source of the energetic particles in the ring current and the processes through which they are energized, injected, and trapped in the ring current region. Such knowledge is imperative for deciphering the dynamics and characteristics of large geomagnetic storms and would allow for improved design of space-borne equipment, as well as enhanced operation of these systems and those that rely on them. For these reasons, characterizing our space environment and the dynamics that drive this complex system is essential as humans leave the confines of our planet and venture further into the expanse of outer space and spend more time living and working in space plasmas.

In order to specify, predict, and mitigate the effects of space weather, a comprehensive understanding is needed of the various components of the solar-terrestrial system and its interactions. The study of Earth's near-space environment, of space weather, and of the

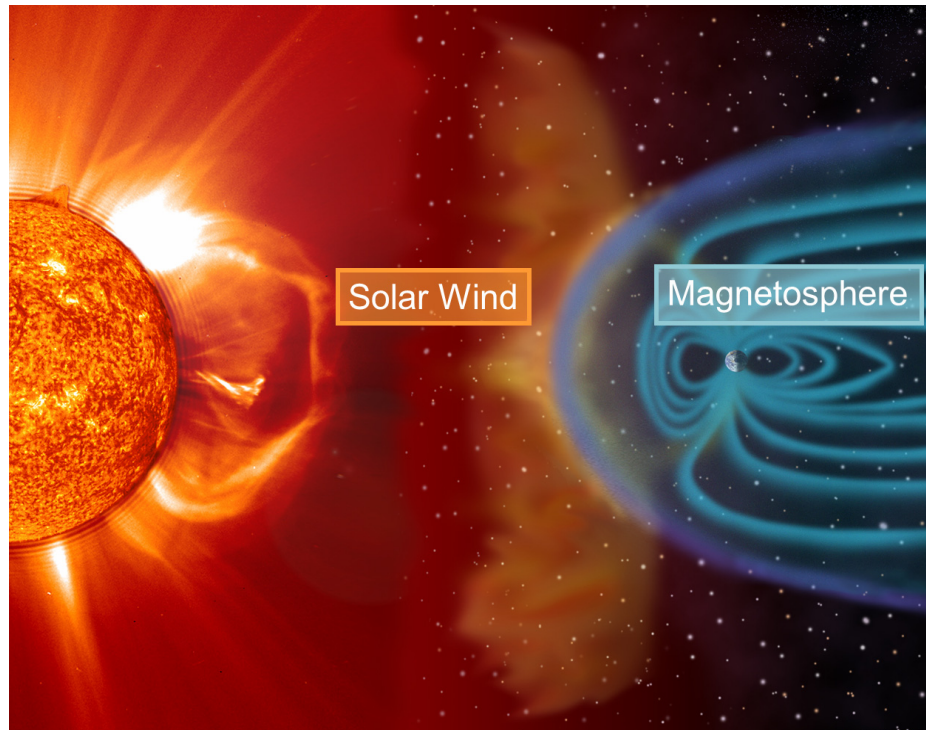


**Figure 1.1** Artist's depiction of the solar-terrestrial system. Energetic particles originating from the Sun comprise the solar wind and are shown in orange impacting the Earth's magnetosphere (blue and purple structure). The bow shock is shown in purple and the blue lines represent Earth's magnetic field lines [Adapted from NASA image].

related plasma physics and coupled interactions is known as *heliophysics*. The field of heliophysics deals with the complex connections between the solar wind, interplanetary magnetic field (IMF), magnetosphere, and ionosphere. This thesis focuses on a sub-discipline within the larger context of heliophysics, namely the ring current, but for completeness and due to the inter-connectivity of all these fields, this initial chapter will first provide the large-scale picture.

## **1.1 Introduction to Solar-Terrestrial Physics**

Within the solar-terrestrial system there are several diverse plasma regions each with distinct properties in terms of energy, density, and composition. The solar wind and IMF, which are generated by the Sun, interact with Earth's magnetic field to create the magnetosphere (Figure 1.1), while solar ultraviolet radiation ionizes Earth's upper

atmosphere create another plasma environment, the ionosphere. In the following sections, each of these regions will be discussed.

### 1.1.1 Solar Wind

The first important component in the solar-terrestrial system is the solar wind, which is a stream of ionized solar particles that flow from the Sun. The solar wind consists of two components: the flowing solar plasma and the entrained solar magnetic field known as the interplanetary magnetic field (IMF). The main constituents of the solar wind are  $H^+$  and  $^4He^{++}$ , with roughly 95% of the typical ion density comprised of protons. The remainder of the plasma is composed of ionized Helium ( $\sim 5\%$ ) and trace amounts of highly ionized C, O, Fe, Mg, and Ne [Parks, 2004]. The solar wind has a typical number density of  $\sim 10\text{ cm}^{-3}$  and a temperature of 10 eV; these densities and temperatures are much lower than those in the solar corona ( $\sim 10^6\text{ cm}^{-3}$  and  $10^2\text{ eV}$  respectively), and higher than those in interstellar space ( $\sim 1\text{ cm}^{-3}$  and  $0.1\text{ eV}$  respectively) [Kivelson and Russell, 1995]. Typical values for the solar wind plasma at Earth are given in Table 1-1. During storm times these values can increase significantly, resulting in densities  $>10\text{ cm}^{-3}$  and velocities  $>1000\text{ km/s}$ .

**Table 1-1** Observed properties of the solar wind near the orbit of Earth (1 AU) from *Baumjohann and Treumann* [2006] and *Kivelson and Russell* [1995].

Parameter	Observed Value
Proton density	$6.6\text{ cm}^{-3}$
Electron density	$7.0\text{ cm}^{-3}$
Helium density	$0.3\text{ cm}^{-3}$
Flow speed (nearly radial)	$450\text{ km}\cdot\text{s}^{-1}$
Proton temperature	$1.2 \times 10^5\text{ K}$
Electron temperature	$1.4 \times 10^5\text{ K}$
Magnetic field	5 nT

### **1.1.2 Interplanetary Magnetic Field**

The Sun's magnetic field that is pulled away by the outflowing solar plasma forms the IMF, a weak magnetic field embedded in the solar wind plasma. The IMF originates from the Sun and is carried by the outflowing plasma that escapes the Sun's strong gravitational pull and transports a vestige of the solar magnetic field into space [Kivelson and Russell, 1995]. Due to the Sun's rotation a spiral pattern emerges in the magnetic field and at 1 AU, the distance from the Sun to the Earth, the magnetic field is oriented  $45^\circ$  from the Sun-Earth line. Typical values for the IMF at 1 AU are  $\sim 5$  nT. During a storm the strength of the interplanetary magnetic field can increase significantly, up to 25 nT or greater, and the direction of the field can also change over a short time period.

### **1.1.3 Magnetosphere**

The third important component in the solar-terrestrial system is the magnetosphere, which is formed when solar wind plasma interacts and is deflected by a planetary magnetic field, creating a plasma cavity in the solar wind. Since Earth has a strong intrinsic magnetic field, our planet consequently has an extensive magnetosphere. The shape of the magnetosphere is determined by the interaction of Earth's intrinsic magnetic field with the solar wind plasma and the IMF. During nominal conditions the magnetosphere typically extends 10-12 Earth radii ( $R_E = 6378$  km) on the dayside; on the night side the magnetosphere is deformed into a comet-tail shape extending beyond  $200 R_E$  in the anti-solar direction with a diameter of up to  $60 R_E$  in the radial direction. During geomagnetic storms, the dayside magnetopause can move in to a distance of  $6 R_E$ , significantly compressing the magnetosphere.

Figure 1.2 shows a cross-section view of Earth's magnetosphere, which contains several diverse plasma regions. The boundary layer between the IMF and Earth's magnetosphere is called the *magnetopause*. The magnetopause forms at the location where the plasma pressure from the solar wind and the magnetic pressure from Earth's magnetosphere are balanced. In front of the magnetopause, a *bow shock* forms in the supersonic solar wind.

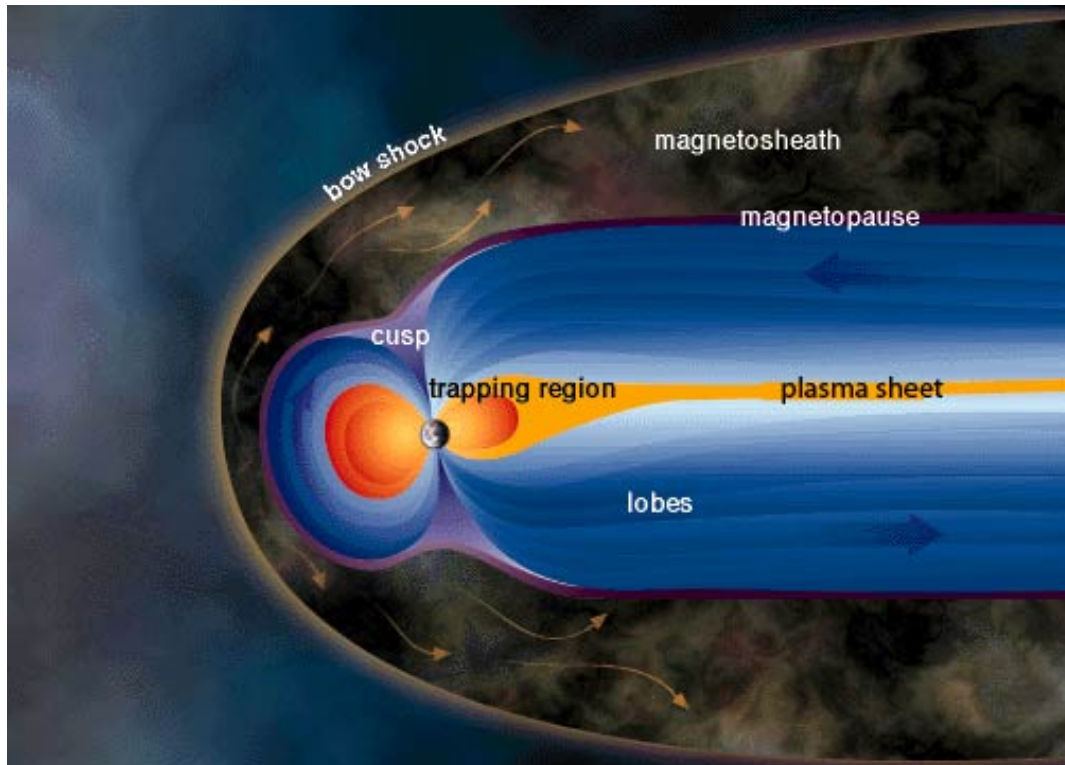


**Figure 1.2** A cross-section view of Earth's magnetosphere with several plasma regions labeled [Image modified from UCAR Windows website].

The bow shock forms upstream in the incident solar wind where the supersonic and super-Alfvénic flow slows down in response to the obstacle presented by the Earth and its magnetic field. This creates a region between the bow shock and the magnetopause known as the *magnetosheath*. The magnetosheath consists of shocked solar wind that has been compressed and heated.

The region inside the magnetopause is divided into several broad regions which include the inner magnetosphere, the plasma sheet, and the tail lobes. The *inner magnetosphere* extends from the edge of the magnetopause on the dayside to a distance of  $\sim 8 R_E$  on the night side. This region is characterized by a nearly dipolar magnetic field and closed drift paths. Included within the inner magnetosphere is the *trapping region* shown in Figure 1.2, which is an area of higher density plasma confined in the orbit around Earth. The radiation

**Table 1-2** Typical near-tail plasma and field parameters from *Kivelson and Russell [1995]*

	<b>Magnetosheath</b>	<b>Tail Lobe</b>	<b>Plasma-Sheet Boundary Layer</b>	<b>Central Plasma Sheet</b>
n (cm <sup>-3</sup> )	8	0.01	0.1	0.3
T <sub>i</sub> (eV)	150	300	1,000	4,200
T <sub>e</sub> (eV)	25	50	150	600
B (nT)	15	20	20	10

belts, plasmasphere, and ring current are all contained within the trapping region in the inner magnetosphere. The region above the poles not included within the inner magnetosphere is known as the *polar cap*. In this region the magnetic field lines are open, meaning that the field lines either connect directly to the IMF or extend along the magnetotail connecting back to the tail lobe. The region of recently merged magnetic field lines Sunward of the polar cap is known as the *polar cusp*, which is a narrow region centered on local noon that extends approximately 2-3 hours in longitude and ~1 degree in latitude. In this region, the shocked solar wind plasma in the magnetosheath has direct access to the ionosphere.

The magnetotail is divided into northern and southern *lobes*, which are regions of lower density (~0.01 cm<sup>-3</sup>) and strong magnetic plasma. Between the lobes is the *plasma sheet*, which is a region of hot, higher density plasma (~1 cm<sup>-3</sup>) centered near the equator of the magnetotail. The plasma sheet has a typical thickness of 3-7  $R_E$  during quiet times, but this thins to ~400 km during active times. The plasma sheet supports the cross-tail current, which flows across the equator of the magnetotail in a dawn to dusk direction, and reconnection events can occur within the plasma sheet during substorms and storms.

Typical plasma parameters within Earth's near-space environment are given in Table 1-2. In this near-Earth region densities vary from 8 cm<sup>-3</sup> in the magnetosheath to 0.01 cm<sup>-3</sup> in the tail lobe area. Within the central plasma sheet, typical densities range from ~0.3-0.5 cm<sup>-3</sup>. The magnetosheath is a dense, cold region with typical temperatures of ~150 eV for ions and ~25 eV for electrons, while the central plasma sheet and plasma-sheet

boundary layer have much higher average temperatures of  $\sim 1,000 - 4,200$  eV for ions and  $\sim 150 - 600$  eV for electrons. Within most of the magnetosphere, typical magnetic field strengths are of order 10 nT; however, closer to the surface of the Earth, the magnetic field increases in strength with a field strength of  $\sim 300$  nT at  $5 R_E$  and  $\sim 1000$  nT at  $3 R_E$ . At Earth's surface the magnetic field strength is  $\sim 30,000$  nT at the equator and  $\sim 50,000$  nT at the poles.

The inner magnetosphere includes the plasmasphere, the ring current, and the Van Allen radiation belts. The plasmasphere consists of low energy plasma, which co-rotates with the Earth. Within the plasmasphere are the ring current and radiation belts, which coexist in the same spatial region, but have increasing larger energies (tens to hundreds of keV) and proportionally smaller densities ( $>10^2$  cm $^{-3}$  in the plasmasphere and  $\sim 1$  cm $^{-3}$  in the ring current).

### **1.1.4 Ionosphere**

The fourth important component in the solar-terrestrial system is the ionosphere, which is a plasma environment formed by solar ultraviolet radiation ionizing the neutral atmosphere above an altitude of  $\sim 80$  km.

Within the ionosphere there are three main regions: the D region, which includes all ionization below 90 km; the E region, which ranges in altitude from 90-150 km; and the F region, which spans the altitude range from 150-500 km and includes the peak ionospheric plasma density (see Figure 1.3). Typical noontime peak plasma densities are around  $10^6$  cm $^{-3}$  with typical temperatures of 0.1 eV. This peak in plasma density occurs at the altitude where the combination of the decreasing solar flux and the increasing neutral density of the atmosphere allow for maximum ionization of neutral atoms. During nighttime, the plasma densities decrease as shown by the dashed line in Figure 1.3. This decrease is particularly severe at lower altitudes in the D and E regions, where molecular ions have a much higher recombination rate with electrons than do atomic ions present higher in the atmosphere.

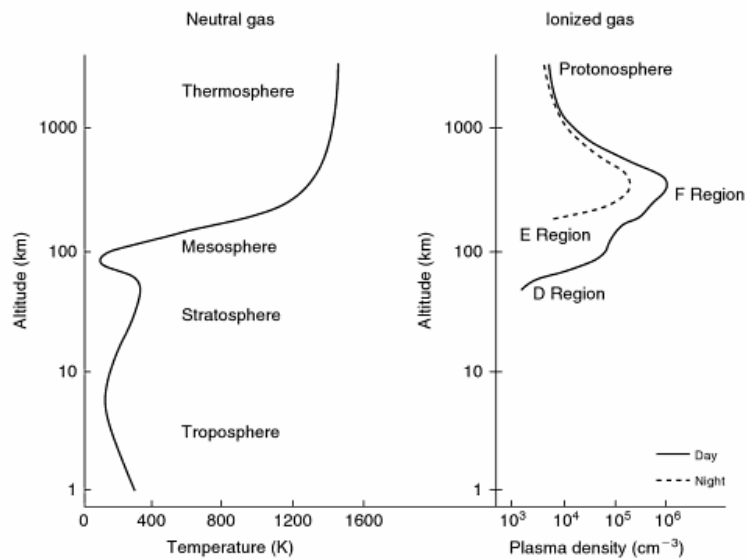


**Figure 1.3** Atmospheric profile for neutral gas (left-hand side) and for ionized gas (right-hand side) [Kelley, 2009].

Photoionization from solar radiation is not the only source of plasma in the ionosphere. Other sources include ionization by energetic particles impacting the neutral gas, a very important source at high latitudes. Energetic particles precipitating into Earth's atmosphere create another effect known as the aurora. The aurorae are electromagnetic emissions given off by atmospheric particles excited by precipitating energetic particles. The formation and detection of auroral emissions on planets in our solar system as well as on other planetary bodies is discussed more fully in Chapter 7.

Figure 1.4 shows empirical data for the ion and neutral composition of Earth's atmosphere with altitude. While molecules such as  $N_2$  and  $O_2$  dominate the atmospheric composition below 100 km, the ion contribution increases with increasing altitude, and above 500 km altitude, electrons, protons, and singly ionized oxygen atoms ( $O^+$ ) are the predominant species in the ionosphere. These particles comprise the major outflowing species from Earth's ionosphere and are an important source of the plasma in the magnetosphere.

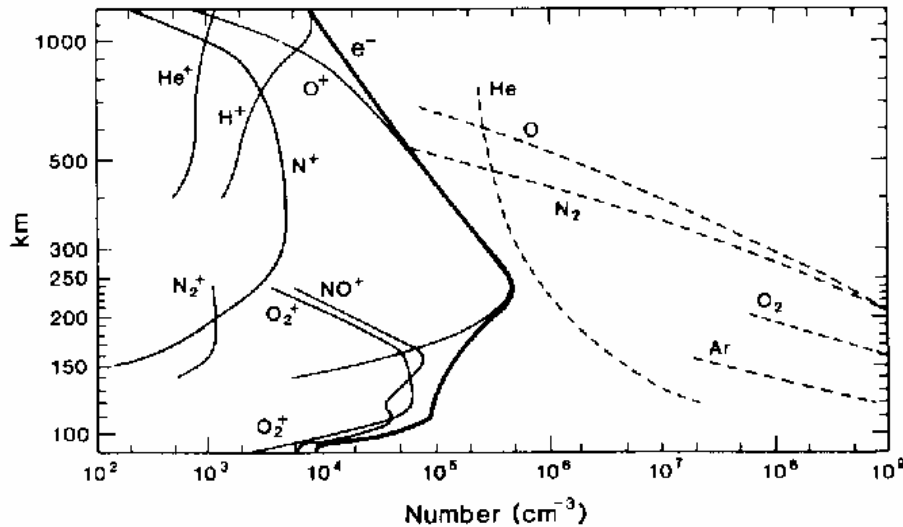


**Figure 1.4** International quiet solar year daytime ionospheric and atmospheric composition based on mass spectrometer measurements [Kivelson and Russell, 1995].

### 1.1.5 Current Systems

Current systems are another key component in a magnetosphere. Within the magnetosphere, the most important electric current systems include the magnetopause current, the plasma sheet current, and the ring current. These current systems can enhance or reduce the strength of the terrestrial magnetic field, which is not produced solely by the Earth's internal magnetic field, but instead is a superposition of intrinsic and induced magnetic fields from a variety of sources. Figure 1.5 gives a schematic of the main currents in Earth's magnetosphere. The *magnetopause current* flows along the magnetopause from dawn to dusk, and induces a magnetic field that increases the magnetic field everywhere within the magnetosphere. The *plasma sheet current* flows across the midnight meridian, again in the dawn to dusk direction, and has the opposite effect, reducing the total B-field. Energetic particles orbiting Earth in the radiation belts and ring current generate a westward flowing current that reduces the horizontal component of Earth's magnetic field at the surface.

When the strength, location, and direction of these currents change, variations are observed in Earth's surface magnetic field. Such fluctuations in Earth's surface magnetic field result

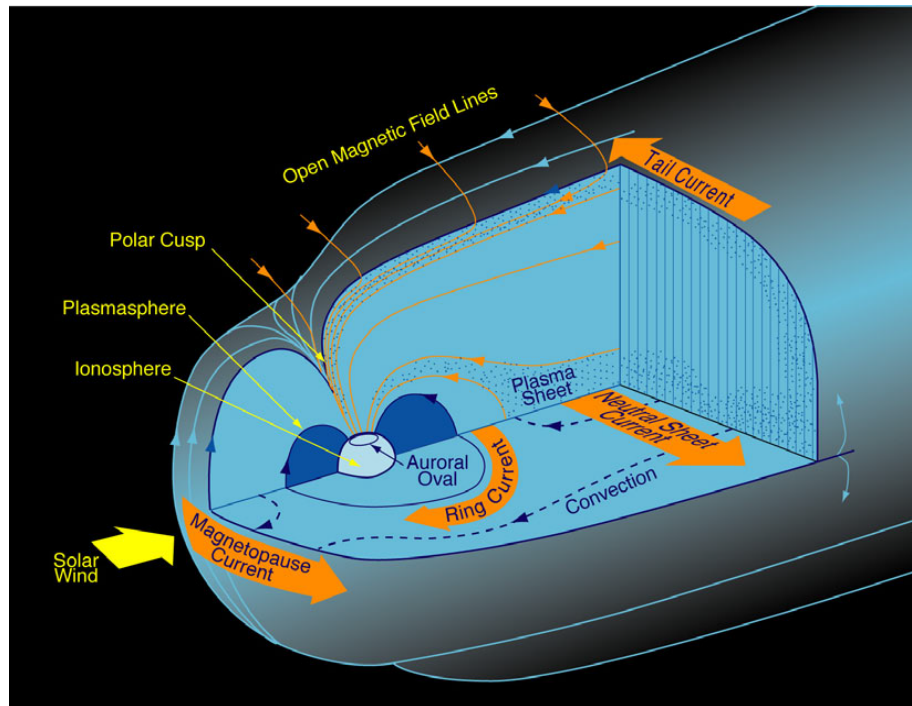


**Figure 1.5** Three-dimensional cutaway view of the magnetosphere showing the most important electric current systems in Earth's magnetosphere, which include: magnetopause current, the neutral sheet current, and the equatorial ring current. The plasmasphere is shown in dark blue and the auroral oval are also shown [NASA/GSFC]. #

in geomagnetic activity. The field of study that examines the relationship between the solar activity and the geomagnetic response is called solar-terrestrial physics. This dissertation deals specifically with just one aspect of these current systems: the ring current. While this current is always present, the strength of the ring current varies in intensity with geomagnetic activity.

## **1.2 Magnetospheric Storms and Substorms**

Geomagnetic activity is a direct manifestation of solar wind-magnetosphere coupling and results in magnetospheric storms, substorms, and aurora. The most frequent type of geomagnetic activity is the magnetospheric substorm. The exact processes which generate substorms are still under debate; however one explanation is that substorms occur due to

prolonged periods of southward IMF (30 minutes or more), during which time there is increased energy flow into the magnetosphere from the solar wind due to dayside reconnection loading mass and energy into the magnetotail. However, substorms also occur during pure northward IMF. Large-scale reconnection events in the near-Earth current sheet can quickly release energy stored in the magnetosphere, accelerating plasma in both earthward and tailward directions. The earthward moving plasma interacts with the inner magnetosphere and the ionosphere, resulting in ionospheric disturbances and creating the most common visual representation of the substorm, the aurora. Substorms occur frequently and typically last a few hours.

Much stronger geomagnetic storms result from enhanced coupling between the solar wind and the magnetosphere and increased energy input into the magnetosphere. Geomagnetic storms are often preceded by extended periods of southward IMF (several hours or longer) followed by a northward turning or by solar activity such as coronal mass ejections (CMEs) or fast solar wind streams. Storms can last anywhere from a few hours to a few days, and the frequency of geomagnetic storms varies over the course of the 11-year solar cycle, with storms more likely to occur during solar cycle maximum.

During periods of geomagnetic activity, the terrestrial ring current fills with energetic particles, intensifying the westward flowing current system. This current produces an induced magnetic field that counteracts the Earth's surface dipole field (Figure 1.6). The corresponding decrease in the surface magnetic field strength is used to assess the severity of the magnetic storm via an index known as the storm-time disturbance index (*Dst*).

The *Dst* index is used to identify and classify geomagnetic storms. It is expressed in nanoteslas (nT) and is a measure of the average deviation of the horizontal component of Earth's magnetic field obtained hourly from four near-equatorial magnetometer stations (all about 30° from the magnetic equator). At such latitudes, the horizontal (northward) component of the magnetic perturbation is dominated by the intensity of the ring current. The *Dst* index is a direct measure of the hourly average of this perturbation.

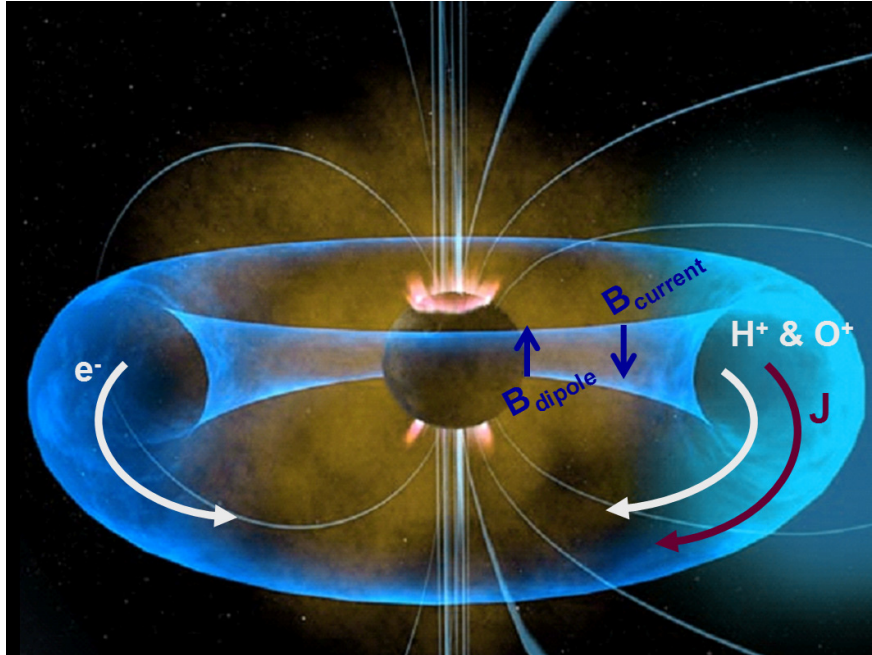


**Figure 1.6** Graphical representation of the ring current showing the flow direction of ions and electrons (white arrows) and the direction of current flow,  $J$  (maroon arrows). At the surface of Earth, the magnetic field from Earth's dipole field points northward and the induced magnetic field from the ring current points southward (blue arrows). The ring current thus results in a decrease in the strength of Earth's surface magnetic field.

A geomagnetic storm often, but not always, begins with an initial increase in  $Dst$ , which is due to a pressure pulse from the solar wind. This is followed by the most prominent feature of a storm, a large decrease in  $Dst$ , known as the storm main phase (Figure 1.7). This sharp decrease in  $Dst$  corresponds to an intensification of the ring current and typically appears on time scales of about an hour. The return to ambient, quiet conditions can take much longer, on the order of several hours, and during this period  $Dst$  begins to slowly rise back to its quiet time level as the ring current recovers. This entire period is called a magnetic storm and is comprised of the sudden storm commencement (sharp rise in  $Dst$ ), the main phase of the storm (sharp decrease in  $Dst$ ), and the recovery phase of the storm (gradual rise in  $Dst$  over several hours). The severity of a storm is classified based on the minimum value of  $Dst$  reached during storm main phase. A  $Dst$  value of  $< -300$  nT, as in Figure 1.7, represents a major geomagnetic storm.

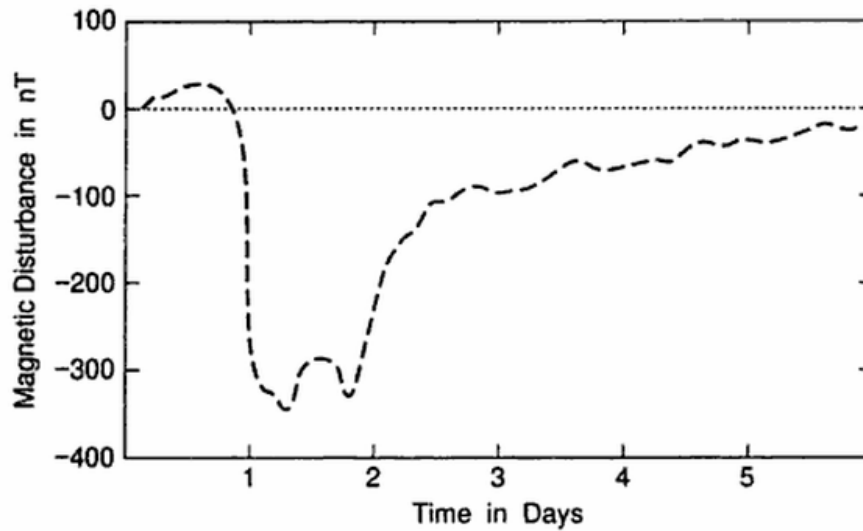


**Figure 1.7** Example of a typical depression in Earth's surface magnetic field strength during a major geomagnetic storm [Baumjohann and Treumann, 1997].

Understanding the source of ring current particles as well as the processes through which the ions are energized, injected, and trapped in the ring current is important for deciphering the underlying forces and characteristics of large geomagnetic storms. The source of ring current particles, the dynamics of particle injection and trapping, particle loss mechanisms, and how these parameters vary with fluctuating solar wind conditions are active areas of research. In order to better explain the plasma physics processes that govern the complex behavior of Earth's magnetosphere, ionosphere, and ring current, physical models capable of capturing these varying and coupled systems are necessary.

### **1.3 Scope of Dissertation**

This work identifies the conditions that drive ring current enhancements and answers the following questions: (1) How do solar wind and outflowing ionospheric ions become accelerated, injected, and trapped in the ring current, and how does this process vary according to ion species and solar wind conditions? (2) How do varying solar wind conditions transition from those generating a moderate storm to those responsible for producing large-scale geomagnetic storms? (3) Which ionospheric outflow regions

contribute most significantly to the ring current during storms and substorms, and what variability is observed between different storms? Specifically, how do solar wind conditions affect the most efficient outflow regions at generating ring current ions? (4) How do particle dynamics affect large and small-scale processes within the global magnetosphere, and what role do small-scale kinetic effects play in the above processes?

Chapter 2 details the ring current, delving deeper into the previous work, open questions, and the specific research questions this thesis addresses. Chapter 3 describes the multifluid and single-particle models used to carry out the numerical calculations, as well as a newly developed combined multifluid / particle code, in which coupling between the two models allows for feedback between the particle dynamics and the global multifluid code. In Chapter 4, the energization of ionospheric ions in the terrestrial magnetotail and the trapping of these particles in the ring current are examined from a particle perspective to address the question of what processes (1) drive the injection of particles in the inner magnetosphere and (2) lead to their energization to form the ring current. Chapter 5 examines the contribution from various ionospheric source regions to the storm time ring current and the effect that IMF  $B_z$  has on producing a symmetric ring current during a large storm event. The ionospheric outflow sectors that contribute most to the ring current in terms of energy and density are identified, illustrating how the dominant source of ring current particles and the ionospheric regions that attain the highest levels of particle energization vary during storm development. Chapter 6 explores the importance of temperature anisotropies and compares single particle tracking results to a version of the multifluid model that includes temperature anisotropies.

Chapter 7 applies our current understanding of space plasmas in our solar system to space plasmas in extrasolar planetary systems in order to determine the feasibility of directly detecting auroral emissions from distant exoplanets. Detecting such extrasolar auroral emissions has implications for astrobiology and for the investigation and characterization of exoplanets orbiting remote stars. In Chapter 7, an analysis of the expected ultraviolet auroral emission strengths from extrasolar giant planets is presented and the possibility of

detecting UV auroral emissions with current and future technology is investigated. Lastly, Chapter 8 provides a summary of the significant results presented in this dissertation and outlines the future direction for this line of research inquiry.

## Chapter 2: The Ring Current

The ring current is a large scale electric current that flows westward around the Earth at distances between  $\sim 4$  and  $9 R_E$  [Daglis *et al.*, 1999]. Westward traveling ions with energies ranging from 10 to 300 keV carry the bulk ( $\sim 90\%$ ) of current produced by the oppositely drifting electrons and ions [Baker and Daglis, 2006 and references therein]; the electrons contribute only  $\sim 1\%$  as much energy as the protons during quiet times, and during active periods the relative electron-to-proton contribution increases to  $\sim 8\%$ - $19\%$  [Liu *et al.*, 2005]. Two ring current sources are the solar wind and ionosphere [Elliott *et al.*, 2001 and references therein], and the relative contribution of each source remains unresolved. Protons originate from both the solar wind and the ionosphere, but the low initial energy of the ionospheric ions ( $\leq 10$  eV) compared to the energy of the arriving solar wind protons ( $\geq 1$  keV) led scientists to believe initially that the ionosphere was not a relevant contributor to the population of energetic  $H^+$  observed in the magnetosphere. Outflowing protons were not thought to experience the heating or acceleration necessary to energize them to the characteristic tens of eV to several keV energies observed in the magnetospheric proton population [Moore & Delcourt, 1995]. However, with the discovery of energetic  $O^+$  (up to 17 keV) in the magnetosphere [Shelley *et al.*, 1972], the Earth's ionosphere could no longer be considered a negligible plasma source [Moore & Delcourt, 1995]. In fact, during intense geomagnetic storms, the primary source of the ring current plasma is terrestrial in origin, [Krimigis *et al.*, 1985; Hamilton, 1988; Sheldon and Hamilton, 1993] as evidenced by the dominance of  $O^+$  in the composition of the storm-time ring current [Lennartsson and Sharp, 1982; Moore *et al.*, 1999; Lotko, 2007]. The discovery of this energetic  $O^+$  population suggested that magnetosphere processes are capable of energizing low-energy ionospheric ions and transporting them from the ionosphere to the magnetotail and back into the inner magnetosphere [Chappell *et al.*, 1987]. Thus, the ionosphere is a significant, if not dominant, source of magnetospheric plasma during active periods. The solar wind may supply the energy, but the ionosphere supplies the vast majority of particles [Chappell *et al.*, 1987].

One of the principal unsolved problems in magnetospheric physics has now become understanding how terrestrial ions are accelerated from their low initial energies of  $\sim 10$  eV, to the 1-500 keV energies observed in the ring current [Roeder *et al.*, 1996]. The observed low energies of the outflowing terrestrial ions suggest that ring current particles must have been accelerated at some point before becoming trapped around the Earth and forming the ring current [Delcourt *et al.*, 1994].

Another open question involves the variation in the source of ring current particles with changing solar conditions. During quiet times,  $H^+$  is the dominant ion and  $O^+$  contributes 1%-10% of the total energy density, with negligible contributions from  $He^+$  and  $He^{++}$  [Williams, 1985; Gloeckler *et al.*, 1985; Krimigis *et al.*, 1985; Sheldon and Hamilton, 1993; Daglis *et al.*, 1994; Roeder *et al.*, 1996]. For moderate to high activity periods, the contribution from ionospheric  $O^+$  increases to  $\sim 27\%$ , making  $O^+$  a more important contributor of particle energy density in the inner plasma sheet and ring current regions during these times [Williams, 1987; Hamilton *et al.*, 1988; Roeder *et al.*, 1996; Baker and Daglis, 2006]. Studies have shown that during large geomagnetic storms, up to 80% of the ring current energy density is carried by ionospheric ions [Hamilton *et al.*, 1988; Sheldon and Hamilton, 1993].

Although it is known that the ionospheric source is important to the contribution of the ring current energy density, especially during storm times, and it is known that  $O^+$  ions contribute more during storms, the specific ionospheric outflow regions from which these particles originate, and how the outflow locations vary with time remains to be addressed.

## **2.1 Previous Modeling and Open Questions**

Much work has already been done investigating all aspects of substorm and storm time particle dynamics attempting to answer many of the open questions associated with the build-up and decay of the ring current. Existing literature addresses key questions about the sources of the magnetospheric plasma, the extent of interplanetary driving conditions,

the relative contribution of various ion species, and the role of substorms in the development of the ring current.

Modeling efforts have significantly contributed to our present understanding of the source of magnetospheric particles. A variety of models have been used to explore mass loading of the magnetosphere by particles of both solar wind and ionospheric origin. *Richard et al.* [1994] examined the entry mechanism of solar wind ions into the magnetosphere using trajectories of non-interacting ions in magnetic and electric fields obtained from a 3D magnetohydrodynamic (MHD) simulation under northward IMF conditions. The dominant entry mechanism of these particles was convection into the magnetosphere on reconnecting field lines. Using Geotail plasma observations and a combination of large-scale kinetic (LSK) technique and time-dependent electric and magnetic fields from MHD simulations to trace ions backwards in time, *Ashour-Abdalla et al.* [1999] investigated the source of ions observed in the near-Earth magnetotail in the midnight sector during a substorm. Two entry mechanisms were identified, entry through a high-latitude reconnection region and entry through open field lines, and results suggest that the magnetosphere contains a mixture of solar wind particles with different histories and residence times. The contribution of solar wind ions to the plasma sheet and non-storm ring current has also been examined by *Moore et al.* [2005] using test particle trajectories in time-dependent magnetic and electric fields obtained from MHD simulations.

The importance of the ionospheric contribution has been addressed by several studies [*Chappell et al.*, 1987; *Moore and Delcourt*, 1995; *Andre and Yau*, 1997]. Particle tracking models have been used in an attempt to quantify the contribution the ionosphere has on the ring current and plasma sheet [*Delcourt et al.*, 1994; *Delcourt and Sauvaud*, 1998; *Elliott et al.*, 2001]. *Delcourt et al.* [1994] and *Delcourt and Sauvaud* [1998] used 3D particle codes to model mass loading of the magnetosphere by outflowing ionospheric ions. *Delcourt et al.* [1994] showed that during quiet times, hydrogen ions from the polar regions were the main source of the plasma sheet ions. *Delcourt and Sauvaud* [1998] examined the transport of plasma sheet particles in the dayside magnetosphere and showed that particles from the cusp can flow back toward the tail along the magnetopause and then

re-circulate, significantly contributing to the population of high-energy particles in the high-latitude boundary layer.

In addition to identifying the source populations of magnetospheric particles, models have been used to investigate the processes that drive the injection of plasma sheet particles (irrespective of their source) into the inner magnetosphere and that lead to their energization. *Moore et al.* [1981] first proposed the “injection front” model in which dispersionless injections are observed in close association with earthward propagating compressional wave fronts. Using a time-varying field model with test-particle trajectories, *Li et al.* [1998] demonstrated that dispersionless injections were caused by an electric field and a self-consistent magnetic field propagating toward the Earth; injected electrons were energized mainly via betatron acceleration. Additional work by *Sarris et al.* [2002] supports the idea that an initial distant magnetotail perturbation propagates inward as high-speed or bursty bulk flows, the perturbation slows down as it approaches the inner magnetosphere causing dipolarization, a compression wave, and dispersionless injections.

Several studies using MHD and test-particle simulations support the identification of near-Earth magnetic reconnection as the ultimate cause of substorm energetic particle injections in the inner magnetosphere [*Birn et al.*, 1997; *Thomsen et al.*, 2001; *Li et al.*, 2003]. The injection of energetic ions has been modeled using the comprehensive ring current model (CRCM), which uses a self-consistently calculated electric field to simulate the evolution of the plasma distribution in the inner magnetosphere [*Fok et al.*, 2001]. CRCM results for  $H^+$  fluxes during the 2 May 1986 magnetic storm agree well with observations. The CRCM predicts stronger electric fields near Earth in the dusk-midnight quadrant, resulting in deeper and faster particle injection into the ring current.

Recent models have also explored the processes through which electromagnetic fields are responsible for the injection of plasma into the inner magnetosphere. Modeling ring current formation using an inductive, localized electric field tied to cycles of stretching and dipolarization of the Tsyganenko magnetic field model, *Fok et al.* [1996] found that the overall increase in the ring current energy during substorms is a result of the enhanced

convection field. Seeking to clarify the relative influences of steady convection and induction electric fields, *Fok et al.* [1999] used single-particle codes to trace particle trajectories backward in time to obtain nightside ion distributions and were able to generate substorm injection features such as the earthward moving “injection front”. *Fok et al.* [1999] found that convection electric field enhancement is critical in order to produce observable changes in the ring current, and without convection enhancement, substorms only produce an enhancement of the cross-tail current.

Dipolarization associated with particle injection can result in both adiabatic and nonadiabatic energization mechanisms. *Birn et al.* [1997] and *Li et al.* [1998] both found that much of the energization associated with particle injection could be attributed to betatron acceleration (an adiabatic process) in the dipolarizing magnetic field earthward of the near-Earth reconnection region. During such dipolarization, significant nonadiabatic particle acceleration has been shown to result from short-lived induced electric fields with no well-defined upper limit to the energization obtained [*Delcourt, 2002*].

Once injected into the ring current region, energized particles will form either an asymmetric or symmetric ring current depending on the orientation and characteristics of the solar wind. Using a global drift-loss model by *Jordanova et al.* [2001], *Kozyra et al.* [2002] examined the decay of the ring current in the early recover phase and addressed the role of preconditioning in multi-step ring current development. Short periods of northward turning of the IMF trap the ring current ions on closed trajectories and seal off the dayside loss region. Likewise, decreasing the strength of a southward IMF also leads to the trapping of ring current particles in the inner magnetosphere on closed drift paths [*Kozyra et al., 2002*].

Seeking to investigate the sources of outflowing ionospheric particles and the ways in which ionospheric outflow varies with external parameters, several studies have looked at the origin of particles outflowing from the ionosphere [*Su et al., 1998; Moore et al., 2005; Winglee et al., 2008*] and the ways in which particle outflow depends on external factors such as the solar wind, IMF, geomagnetic activity, and convection [*Abe et al., 2001; Elliott*

*et al.*, 2001; *Peterson et al.*, 2002; *Howarth and Yau*, 2008]. Using data from the FAST, Akebono, and Polar satellites, *Peterson et al.* [2002] examined correlations between the net global ion outflow rate and geomagnetic and solar activity for intervals of both quiet and disturbed magnetic activity. They concluded that short time and spatial scale variation of ion outflow must be included in any large scale model of the magnetosphere that attempts to include effects of small-scale variations in magnetospheric mass density. The response of ionospheric outflow to changing solar conditions as a function of latitude and magnetic local time (MLT) has been modeled by *Winglee et al.*, [2008] who found that the composition of the magnetosphere can change with variations in the IMF of as small as  $\pm 1$  nT. *Elliott et al.* [2001] compared the properties of  $H^+$  and  $O^+$  outflow with solar wind and IMF properties using Thermal Ion Dynamics Experiment data. It was found that during northward IMF, sunward convection has been observed to occur, while during southward IMF, anti-sunward convection in the polar caps is observed.

Using multi-fluid simulations, *Winglee* [1998] showed that during southward IMF, field lines convect faster over the polar caps, resulting in enhanced convection of ionospheric plasma out of the polar regions, increased density in the lobes, and substantial enhancement of the ionospheric contribution to the plasma sheet. Particles originating from the ionosphere are energized when they reach the near-Earth neutral line (NENL). The resulting energized particles provide much of the hot plasma in the current sheet [*Winglee*, 1998]. The stronger centrifugal acceleration of ionospheric plasma during southward IMF results in enhanced ionospheric outflow. Ionospheric plasma dominates the plasma sheet in the midnight sector [*Winglee*, 2003] and  $O^+$  dominates over  $H^+$  during storm periods [*Roeder et al.*, 1996]. *Winglee* [1998] also showed that during northward IMF the field lines have slower convection over the polar caps and ionospheric outflows are suppressed. The solar wind plasma enters through high-latitude reconnection regions and the mass-loaded field lines convect to the nightside where solar wind plasma is deposited at the low-latitude boundary layer (LLBL) and plasma sheet [*Winglee*, 1998]. *Song and Russell* [1992] showed that the LLBL became more prominent during northward IMF, suggesting that it is formed by high latitude reconnection.

The ultimate destination of outflowing ionospheric ions has been explored using numerical tracing of particle trajectories, which has proven to be a powerful tool for understanding plasma transport and distribution within the magnetosphere. Employing a full-particle tracking scheme, *Ehibara et al.* [2006] looked at the transport and final destination of outflowing  $O^+$  ions to determine whether particles went into the magnetopause, the distant tail, the ring current, or the atmosphere. They found that the number of ions reaching each of the four final destinations depended largely on the magnetic field configuration and ionospheric conditions. During an active-time magnetic field, the number of ions reaching the ring current increased by a factor  $\sim 3$  compared with the quiet time magnetic field and greater outflow rates from the ionosphere were observed. Also employing single-particle trajectory simulations, *Howarth and Yau* [2008] explored the influence of the IMF and convection electric field on the rate and destination of low-energy ion outflows. During periods of negative  $B_z$ , low-energy outflowing ions were confined to lower L-shells and low-temperature oxygen ions were found to have a higher probability of escape when originating from the noon and dusk sectors. The IMF  $B_y$  component was found to affect the way in which ionospheric ions were distributed, with ions preferentially feeding the dusk sector for positive  $B_y$ , and with the ions distributed more uniformly throughout the plasma sheet during periods of negative  $B_y$ .

In addition to identifying the ultimate destination of outflowing ions, models have been used to explore the effects of plasma sheet density and temperature on ring current parameters. Using kinetic ring current simulations for an idealized storm, *Lavraud and Jordanova* [2007] found that for a colder and denser plasma sheet, the resulting proton ring current energy was significantly increased given a constant initial energy density. Investigation into the effects of density and temperature showed that the ring current strength was primarily controlled by density, while particle temperature controlled the ring current peak location, with colder plasma resulting in a ring current peak closer to Earth and midnight. This work suggests that the presence of cold and dense plasma in the magnetotail may lead to an increased ring current during an ensuing storm.

Recently *Vogiatis et al.* [2011] investigated four substorm events captured by the Time History of Events and Macroscale Interactions during Substorms (THEMIS) spacecraft in February 2008. Analyzing wave, particle, electric and magnetic field data, the observed initial earthward propagating disturbances were interpreted as flux ropes embedded inside fast earthward convective plasma flows in the central plasma sheet. These results are in agreement with previous studies by *Imber et al.* [2011], in which an earthward traveling flux rope was observed with same magnetic field and plasma flow signatures. In the recent THEMIS observations reported by *Vogiatis et al.* [2011], the flux ropes were accompanied by energetic ions with the ion population “being carried” earthward by the flux ropes. Particle energization was observed to be a continuous process occurring in front of the flux ropes for all four of the substorm events captured by the THEMIS spacecraft in February 2008.

Differences in the relative contributions of  $H^+$  and  $O^+$  to the ring current energy density have been explored for both substorms [*Daglis et al.*, 1994; *Daglis and Axford*, 1996] and storms [*Daglis*, 1997; *Daglis et al.*, 1999]. Using the storm time observations from the Combined Release and Radiation Effects Satellite (CRRES), *Daglis* [1997] compared the relative contribution from the two major ion species,  $H^+$  and  $O^+$ , to the total ring current energy density during five magnetic storms occurring in 1991 and showed that  $O^+$  is the dominant ion species present in the ring current during the main phase of large storms.

## **2.2 Questions to be Addressed**

To further our knowledge of how particle acceleration and transport mechanisms differ with varying levels of geomagnetic activity (storms versus substorms), this dissertation resolves the small-scale particle dynamics within the current sheet, boundary layers, and reconnection regions that accelerate ring current particles within the larger global context of the magnetosphere. A combined multifluid and particle approach capable of resolving small-scale dynamics key to particle energization within the context of the global magnetosphere is used to investigate the transport of the energetic particle. Such an

approach allows investigation into many of the open questions mentioned above; in particular, this dissertation focuses on addressing the following questions:

- 1) *How do outflowing ionospheric ions become accelerated, injected and trapped in the ring current and how does this process vary according to ion species and solar wind conditions? (Chapter 4)*
- 2) *What part do small-scale kinetic effects play in particle energization, and what variations are observed between hydrogen and oxygen ions? (Chapter 4)*
- 3) *What differences are observed between storms and substorms in terms of particle energization and transport? Specifically, how do the conditions transition from those generating a moderate storm to those responsible for producing large geomagnetic storms? (Chapter 5)*
- 4) *Which ionospheric outflow regions contribute most significantly to the ring current during storms and substorms, and what variability is observed between different storms? Specifically, how do solar wind conditions affect the most efficient outflow regions at generating ring current ions? (Chapter 5)*

To address these questions, this work uses a single particle tracking model and a multifluid model, both of which are described in detail in Chapter 3.

## Chapter 3: Numerical Methods

The work presented in this dissertation is based upon two individual models: a multifluid / multi-scale model and a single-particle tracking model. This chapter introduces both of these models and the equations on which they rely. As part of this thesis I have included high resolution capabilities within the single-particle tracking model, and I have worked to combine these two separate models into a combined multifluid / particle model. In addition to describing the two models individually, this chapter discusses the implementation and benefits of embedding the particle tracking code within the global multifluid model.

### 3.1 Multifluid Model

The multifluid model used throughout this dissertation is described in detail in Winglee [2004]. Below a brief overview of the multifluid code is presented. The multifluid model simultaneously tracks multiple, separate ion fluids and an electron fluid; the dynamics of each ion species, denoted by the subscript  $\alpha$ , are described by the continuity equation for mass conservation, the momentum equation, and the pressure equation:

$$\frac{\partial \rho_\alpha}{\partial t} + \nabla \cdot (\rho_\alpha \mathbf{V}_\alpha) = 0 \quad (3.1)$$

$$\rho_\alpha \frac{d\mathbf{V}_\alpha}{dt} = q_\alpha n_\alpha (\mathbf{E} + \mathbf{V}_\alpha \times \mathbf{B}) - \nabla P_\alpha - \left( \frac{GM_E}{R^2} \right) \rho_\alpha \hat{\mathbf{r}} \quad (3.2)$$

$$\frac{\partial P_\alpha}{\partial t} = -\gamma \nabla \cdot (P_\alpha \mathbf{V}_\alpha) + (\gamma - 1) \mathbf{V}_\alpha \cdot \nabla P_\alpha \quad (3.3)$$

In the above equations,  $\rho_\alpha$  represents the mass density,  $\mathbf{V}_\alpha$  is the bulk velocity,  $n_\alpha$  is the number density, and  $q_\alpha$  is the particle charge.  $G$  is Newton's gravitational constant,  $M_E$  denotes the mass of Earth,  $P_\alpha$  is the pressure for each separate ion species and  $\gamma$ , the ratio of specific heats, is set to 5/3 for the 3D simulation.

For speeds slow compared to the speed of light, the displacement current can be neglected, and the plasma current can then be described by

$$\mathbf{J} = \frac{1}{\mu_0} \nabla \times \mathbf{B} \quad (3.4)$$

We can then compute the total ion velocity,  $V_i$ , and electron velocity,  $V_e$

$$V_i = \sum_i \frac{n_\alpha}{n_e} V_\alpha \quad (3.5)$$

$$V_e = \sum_i \frac{n_\alpha}{n_e} V_\alpha - \frac{\mathbf{J}}{en_e} \quad (3.6)$$

where  $n_e$  is the electron density,  $n_\alpha$  is the density for each of the ion species,  $e$  the electron charge, and  $J$  is the current density. Assuming the electrons have sufficiently high mobility along the field lines and that  $dV_e/dt$  is small on the simulation timescale, then  $dV_e/dt$  can be approximated as being zero. Using this assumption and neglecting the gravitational term enables us to reduce the momentum equation (3.2) for the electron population to

$$\mathbf{E} + \mathbf{V}_e \times \mathbf{B} + \frac{\nabla P_e}{en_e} = 0 \quad (3.7)$$

By substituting the equation for the electron velocity (3.6) into above momentum equation for the electron population (3.7), one obtains

$$\mathbf{E} = -\sum_i \frac{n_\alpha}{n_e} V_\alpha \times \mathbf{B} + \frac{\mathbf{J} \times \mathbf{B}}{en_e} - \frac{1}{en_e} \nabla P_e \quad (3.8)$$

which is the modified Ohm's law. The first term in (3.8) is the ideal Ohm's law and all ion components contribute. The second and third terms are the Hall and pressure gradient

corrections, which have been shown to be important in generating magnetotail flux ropes during reconnection [Shay *et al.*, 1998; Winglee *et al.*, 1998; Zhu and Winglee, 1996]. A resistivity term  $\eta(x)\mathbf{J}$  is added to equation (3.8) to account for the effects of finite conductivity in the ionosphere. The resistivity term is only applied in the ionosphere where there is a finite conductivity produced by atmospheric collisions. No anomalous resistivity is included in the code and at all other locations in the simulation space the resistivity is set to zero.

To advance the fluid parameters, a second-order Runge-Kutta method is used. In this method, the parameters  $\rho_\alpha$ ,  $\mathbf{V}_\alpha$ ,  $P_\alpha$ , and  $\mathbf{B}$ , are advanced using the continuity equation (3.1), the pressure equation (3.3), and the individual fluid momentum equation (3.9), which is obtained by substituting the modified Ohm's law (3.8) into equation (3.2).

$$\rho_\alpha \frac{d\mathbf{V}_\alpha}{dt} = q_\alpha n_\alpha (\mathbf{V}_\alpha \times \mathbf{B} - \sum_i \frac{n_\alpha}{n_e} \mathbf{V}_\alpha \times \mathbf{B}) + q_\alpha n_\alpha \left( \frac{\mathbf{J} \times \mathbf{B}}{en_e} - \frac{1}{en_e} \nabla P_e \right) - \nabla P_\alpha - \left( \frac{GM_E}{R^2} \right) \rho_\alpha \hat{\mathbf{r}} \quad (3.9)$$

If one assumes a single ion species, then equation (3.9) reduces to the ideal MHD momentum equation. The first term in the right hand side of equation (3.9), which is zero in MHD, is actually non-zero in the presence of different ion species and is responsible for producing ion cyclotron effects that are significant at boundary layers and thin current sheets. In order to observe the ion cyclotron effects, it is necessary to have at least two ion species with significantly different masses. At Earth, oxygen is used as the heavy ion species and hydrogen is used as the light ion species. Around other planets and satellites the heavy and light ion species can vary, but as long as there is a significant difference in masses and hence a large difference in the gyro-radii, ion cyclotron effects can be observed.

Finally to close the set of equations, we invoke Faraday's Law (3.10), which is used to advance the magnetic field,

$$\frac{\partial \mathbf{B}}{\partial t} = -\nabla \times \mathbf{E} \quad (3.10)$$

The above equations are solved using a 2<sup>nd</sup> order Runge-Kutta, in which the parameters are first advanced from  $n$  to  $n+1/2$  to obtain  $\rho_\alpha^{n+1/2}$ ,  $V_\alpha^{n+1/2}$ ,  $P_\alpha^{n+1/2}$ , and  $\mathbf{B}^{n+1/2}$ , the values at the half time step. These values are then used to calculate the remaining fluid parameters,  $\mathbf{J}^{n+1/2}$ ,  $V_i^{n+1/2}$ ,  $V_e^{n+1/2}$ , and  $\mathbf{E}^{n+1/2}$ , also at the half time step using equations (3.4) through (3.8). This process is then repeated using the values at the half time step for the derivatives and advancing the fluid parameters from time  $n$  to time  $n+1$ . The equations below show the final advance of the fluid parameters in the second-order Runge-Kutta using the derivative at the half step to calculate the full time step.

$$\rho_\alpha^{n+1} = \rho_\alpha^n + \Delta t \frac{\partial \rho_\alpha^{n+1/2}}{\partial t} \quad (3.11)$$

$$(\rho_\alpha V_\alpha)^{n+1} = (\rho_\alpha V_\alpha)^n + \Delta t \frac{\partial (\rho_\alpha V_\alpha)^{n+1/2}}{\partial t} \quad (3.12)$$

$$P^{n+1} = P^n + \Delta t \frac{\partial P^{n+1/2}}{\partial t} \quad (3.13)$$

$$\mathbf{B}^{n+1} = \mathbf{B}^n + \Delta t \frac{\partial \mathbf{B}^{n+1/2}}{\partial t} \quad (3.14)$$

### 3.2 Particle Tracking

The particle tracking model follows the flow and energization of particles from their initial sources as they convect through the magnetosphere. The particle dynamics are described using the following two equations

$$\frac{dx_\xi}{dt} = \mathbf{v}_\xi \quad (3.15)$$

$$m_\xi \frac{d\mathbf{v}_\xi}{dt} = q_\xi (\mathbf{E} + \mathbf{v}_\xi \times \mathbf{B}) \quad (3.16)$$

where the subscript  $\zeta$  represents an individual particle. The Lorentz force equation (3.16) relies on the three-dimensional, time-dependent magnetic and electric fields obtained from the multifluid simulations as inputs. The electric and magnetic field at a particular position and time are determined using a linear interpolation scheme between both grid points and time steps. This interpolation method is chosen because it allows repeated use of the given electric and magnetic fields for various particle simulations. In this way, the same electric and magnetic fields can be used to investigate the response of different ion species, namely  $H^+$  and  $O^+$ , from several injection locations (sources) over a similar timescale. The effects of gravity can be ignored because of the strong convective conditions. A fourth-order Runge-Kutta scheme is used to advance the position and velocity of each particle within the simulation.

## Chapter 4: Ring Current Formation during Substorm Conditions

In this chapter, the energization of ionospheric ions in the terrestrial magnetotail and the trapping of these particles in the ring current during an internally driven substorm are examined from a particle perspective using time-dependent electric and magnetic fields from multifluid simulations in order to address the question of what processes (1) drive the injection of particles in the inner magnetosphere and (2) lead to their energization to form the ring current. The specific goal of this chapter is to investigate conditions that lead to the injection front of energetic particles that potentially feed the ring current as proposed by *Li et al.* [2003], and how these conditions lead to the formation of the asymmetric and symmetric components of the ring current for an idealized substorm. Electrons are neglected due to their small energy contribution [*Liu et al.*, 2005] and the ionospheric source is chosen as the primary source of particles since the ionosphere is supplying the bulk of the tail plasma for the conditions considered here [*Winglee et al.*, 2009]. Boundary and initial conditions for the multi-fluid simulation code and the particle tracking algorithms are given in section 4.2. Sections 4.3-4.6 explore particle energization and trapping during an internally driven substorm with changes in solar wind  $B_z$ . Small-scale structures within a thin post-plasmoid current sheet and earthward-moving flux ropes are found to accelerate and energize particles during a constantly southward IMF. The importance of high resolution capabilities is illustrated by the need to resolve these small-scale current sheet structures in order to observe physical acceleration mechanisms.

Once energized, the generation of a symmetric ring current is shown to be dependent for changing solar wind  $B_z$  conditions. The role of northerly turnings in the IMF as well as the timing and degree of the northward turning are examined and it is found that a northerly turning is important in producing a symmetric current ring, but the degree of northward turning is not as critical. A northerly turning to zero IMF appears to still allow for the formation of a symmetric ring current. A summary of the results and conclusions regarding

particle injection, acceleration, and trapping during an internally driven substorm and the influence of small-scale structures in the tail on ions from ionospheric origin are presented in section 4.6. Material in this chapter was originally published in the *Journal of Geophysical Research – Space Physics* and is reproduced with permission of the American Geophysical Union [Cash *et al.*, 2010a].

## 4.1 Overview

Single-particle tracking with time-dependent global magnetic and electric fields is used to investigate the generation of the ring current from ionospheric outflows during an internally driven substorm. We show that the energization of the ions is not correlated with the time that the ions leave the ionosphere, instead energization is correlated with the formation of an injection front driven by an earthward moving flux rope at onset. Because of the large gyro-radius of the  $O^+$  ions, they experience strong dawn/dusk acceleration in the vicinity of the injection front. The acceleration is strongly influenced by small-scale structures including the Hall electric field and the development of kinks across the tail.  $H^+$  is mainly energized by betatron acceleration as it is injected into the inner magnetosphere, and the average energy of the  $H^+$  ions is less than the  $O^+$  ions. In this paper we investigate the conditions that lead to the formation of the injection front and small-scale structures ( $\sim 1 R_E$ ) in the current sheet, such as tail kinking and flux ropes, that are correlated with particle convection and energization at substorm onset. High-resolution capabilities allow us to resolve these small-scale processes within a thin ( $< 1000$  km) current sheet, and we show that simulations with coarse grid resolution underestimate the energization of ring current particles. The role of IMF  $B_z$  on dayside particle loss is also examined. It is found that northerly turning IMF at or shortly after onset is important in producing a symmetric ring current, but the degree of turning is not as critical.

## 4.2 Boundary and Initial Conditions

Equations (3.1) – (3.8) are solved on a ‘nested’ Cartesian grid system with grid spacing increasing outwards from  $\sim 0.3 R_E$  near the Earth to  $2.4 R_E$  in the distant tail. The entire

simulation area extends from  $+47 R_E$  Sunward to  $-377 R_E$  downtail,  $\pm 94 R_E$  in the dawn-dusk direction, and  $\pm 70 R_E$  over the poles in order to allow for a global perspective. A region containing the Earth with  $0.3 R_E$  grid resolution extends from  $+17.7 R_E$  Sunward to  $-35.4 R_E$  downtail,  $\pm 11.8 R_E$  in the dawn-dusk direction, and  $\pm 8.9 R_E$  over the poles. Two additional high resolution grids are included in the tail, with resolution varying from 940 km between  $-1$  to  $-28 R_E$  downtail,  $\pm 8.85 R_E$  in the  $y$  direction, and  $\pm 4 R_E$  in the  $z$  direction, to a resolution of 470 km in a region extending  $-8.85$  to  $-22 R_E$  downtail,  $\pm 4.4 R_E$  in the  $y$  direction, and  $\pm 2 R_E$  in the  $z$  direction. In these high resolution regions, we are able to resolve small-scale structures in the tail, which are shown to be important for particle energization.

The inner boundary of the simulations is set at  $2.7 R_E$ . Within the simulation, the “ionosphere” (the region of non-zero resistivity) extends earthward from  $0.17 R_E$  above the inner boundary with the resistivity increasing with decreasing radius. In the multifluid simulations the proton density is assumed to be  $800 \text{ cm}^{-3}$  at the equator, and the density then decreases with increasing latitude reaching a minimum density of  $400 \text{ cm}^{-3}$  over the poles. A variable  $\text{O}^+$  concentration is included at the inner boundary in the vicinity of the auroral oval with a 5% concentration at auroral latitudes which then decreases with latitude to zero at both the poles and at the equator. In order to attain an initial equilibrium configuration for the magnetosphere, the simulations are run for 2 hours under quiescent conditions during which time equilibrium is established with zero IMF in all directions, a solar wind density of  $6 \text{ cm}^{-3}$ , and a solar wind velocity of 450 km/s. Once an approximate equilibrium configuration is established, the  $B_z$  component of the IMF is turned southward to  $-5 \text{ nT}$  at 0200 UT and all other solar wind parameters remain unchanged. After the initial southward IMF propagates through the magnetosphere, six different cases are examined by turning the IMF northward at various times and to varying degrees, while holding all other parameters constant.

The six cases examined for the changing solar wind IMF  $B_z$  are as follows: (1) the IMF is kept southward at  $-5 \text{ nT}$  for the entire run; (2–5) the IMF is southward initially and is then flipped northward to  $0 \text{ nT}$  at 0232 UT, 0244 UT, 0257 UT, and 0313 UT, respectively; (6)

the IMF is southward initially and turns northward to 5 nT at 0310 UT. The electric and magnetic fields from the multifluid simulations were saved at 1.5 minute (simulated time) intervals as they were run and these fields were then read into the particle tracking model described in detail in section 3.2.

#### **4.2.1 Particle Initialization**

All particles are injected into the simulation at an altitude of  $3.5 R_E$ , slightly higher than the inner boundary of the fluid simulations, in order to avoid boundary condition effects. Particles were initialized from a variety of magnetic local times (MLTs) and latitudes ranging from  $35^\circ$  to  $85^\circ$  in order to find the outflow location that allowed for the greatest observed particle energization, the geo-optimal location from which to initialize the particles. For the results presented in section 4.3, hydrogen and oxygen ions were initialized on the nightside in a region extending from  $55^\circ$  to  $75^\circ$  latitude and from 22 to 02 MLT. In section 4.4 the same initial location for hydrogen ions is used, while the initial location for the oxygen ions is moved slightly dawn of midnight to a region extending from 02 to 06 MLT and from  $55^\circ$  to  $75^\circ$  latitude. For both species, particles are initialized with a beam velocity of 0.4 km/s and a randomly distributed thermal velocity of 4 km/s in an isotropic Maxwellian. This gives average outflow energies of 0.08 eV and 1.3 eV for  $H^+$  and  $O^+$ , respectively.

In these simulations, both continuous and one-time injection schemes are used. For continuous injections, the injection rate varied from 2000 particles injected at 6 minute time intervals, to 100,000 particles injected at 2 minute time intervals. The total number of particles injected was limited to 1,000,000 over the period of interest (typically 2 hours). For the one-time particle injection scheme, 100,000 ions were launched from the midnight sector at a single time in order to allow for detailed examination of convection patterns and energization regions. The continuous injection scheme, while lacking the ability to provide detailed information about the convection pattern of a particular source at a given time, allows for full temporal coverage, which is necessary in determining the

conditions capable of producing a stable ring current. This scheme also allows for improved particle statistics and is used in the quantitative flux calculations.

### **4.3 Particle Energization**

To explore potential energization mechanisms for  $H^+$  and  $O^+$ , particles are initialized in a single, one-time injection of 100,000 ions launched from the midnight sector for several different times during the course of the idealized substorm. Using several one-time injections enables us to investigate the relationship between particle injection and substorm timing and to correlate regions of particle energization with structures in the electric and magnetic fields. Particles were injected at times ranging from 0220 to 0238 UT in order to determine if particle energization occurs a fixed amount of time after the initial injection or if particle energization is more dependent on structures within the electromagnetic fields and occurs at approximately the same time regardless of the initiation time. Analysis of eight different starting times for each ion species suggested that the structures within the plasma sheet were associated with particle energization and injection into the inner magnetosphere. All particles launched between 0220 and 0234 UT are injected in a group in relation to the development of an injection front that forms in the tail between 0257 and 0302 UT. The injection front appears to be related to the formation of a large earthward moving flux rope at 0257 UT, which impacts the inner edge of the plasma sheet at 0259 UT [see *Winglee et al.*, 2009 Figure 11], suggesting that substorm initiation has more to do with particle energization than the time at which particles are injected into the simulation.

Particle tracking results for  $O^+$  launched at 0220 UT in a continuously southward IMF are shown in Figure 4.1. Panels a-d show particle energy plotted on top of white magnetic field lines and panels e-h shows an equatorial view of the particles plotted with white arrows showing the bulk  $O^+$  velocity. Panels (a), (b), (e), and (f) show the magnetosphere in a stretched configuration with the tail field lines basically parallel to the equatorial plane. This magnetospheric configuration developed after the formation of an X line and the ejection of a plasmoid at 0235 UT. The retreating plasmoid leaves a thin current sheet behind (0241 UT) and fast flows in the  $x$  direction result in the formation of a Y line

(0246 UT) with the magnetic field lines parallel to the equatorial plane. Within the Y line, magnetic reconnection is observed around  $14 R_E$  and oxygen ions are observed to gain energy as they move duskward due to cross-tail convection (Figure 4.1a, b, e, and f). The gyroradius of  $O^+$  is larger than the current sheet thickness allowing oxygen ions to break the frozen-in condition and move independently of the field lines. Oxygen ions then experience strong acceleration by the convection electric field as they travel across the tail. The inductive electric field also transports the particles toward earth via  $E \times B$  drift, energizing the ions further due to betatron acceleration. When energized particles reach the inner edge of the plasma sheet on the dusk side, they drift westward due to  $\nabla B$  and curvature drifts. Particles observed to drift eastward are lower energy ions ( $< 5$  keV) from the post-midnight region that convect eastward around the Earth due to convective flows moving earthward from the tail (Figure 4.1g and Figure 4.1h). These results agree with *De Michelis et al.* [1997] who observed local time asymmetries between two populations of oppositely drifting ions and calculated the energy threshold separating energetic westward drifting ions from less energetic eastward drifting ions to be  $\sim 5$  keV at 00 MLT and  $6 R_E$ . A separate group of low energy particles can be seen to flow up above the current sheet in the isometric projection of the magnetosphere on the left side of Figure 4.1 (a-d). These are particles from the initial injection convecting downtail on open field lines.

The formation of a large earthward moving flux rope around  $-16 R_E$  at 0257 UT signifies the end of the stretched configuration of the magnetosphere and in the subsequent images (Figure 4.1g and Figure 4.1h), the energy dispersion of  $O^+$  is no longer spread uniformly in the  $y$  direction with the most energetic particles being on the dusk side of the current sheet and the least energetic particles closer to midnight. In addition, other particles are energized in a group (injection front). These later times represent substorm conditions. In the wake of a tailward moving flux rope, which is observed at  $-35 R_E$  in Figure 4.1c exiting the region, a large earthward moving flux rope develops at 0257 UT around  $-16 R_E$ . This earthward moving flux rope develops near the location of the X line and reaches the inner edge of the plasma sheet 2 minutes later. In order to more clearly see the

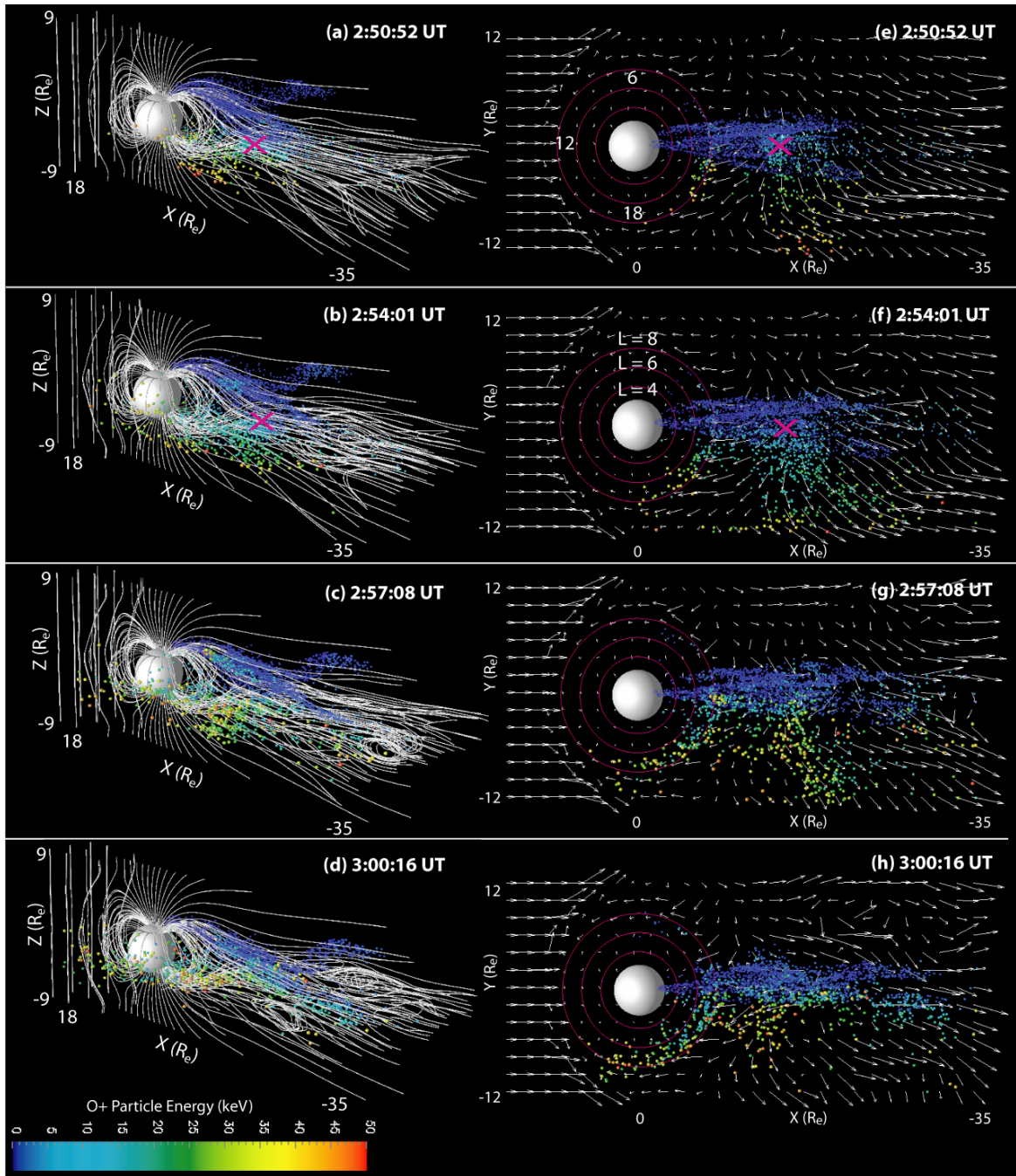


**Figure 4.1** Time evolution of a single injection at 0220 UT of 100,000  $O^+$  ions injected at an altitude of  $3.5 R_E$  from  $55^\circ$  to  $75^\circ$  latitude and from 22 to 02 MLT. The particles are color coded to energy and plotted alongside white magnetic field lines and white  $O^+$  flow vectors (equatorial plane). Magenta circles represent  $L$ -shell values of 4, 6 and 8 and a magenta cross denotes clearly recognizable  $X$  line. (e, f) Energization due to cross-tail convection is clearly visible. (c) An earthward moving flux rope is observed in the tail at  $-16 R_E$  (see Figure 4.2b) and (g) particle energization occurs in a group around  $-16 R_E$ . (d) the injection front observed in Figure 4.1c has moved earthward and particles are being deposited in the inner magnetosphere.

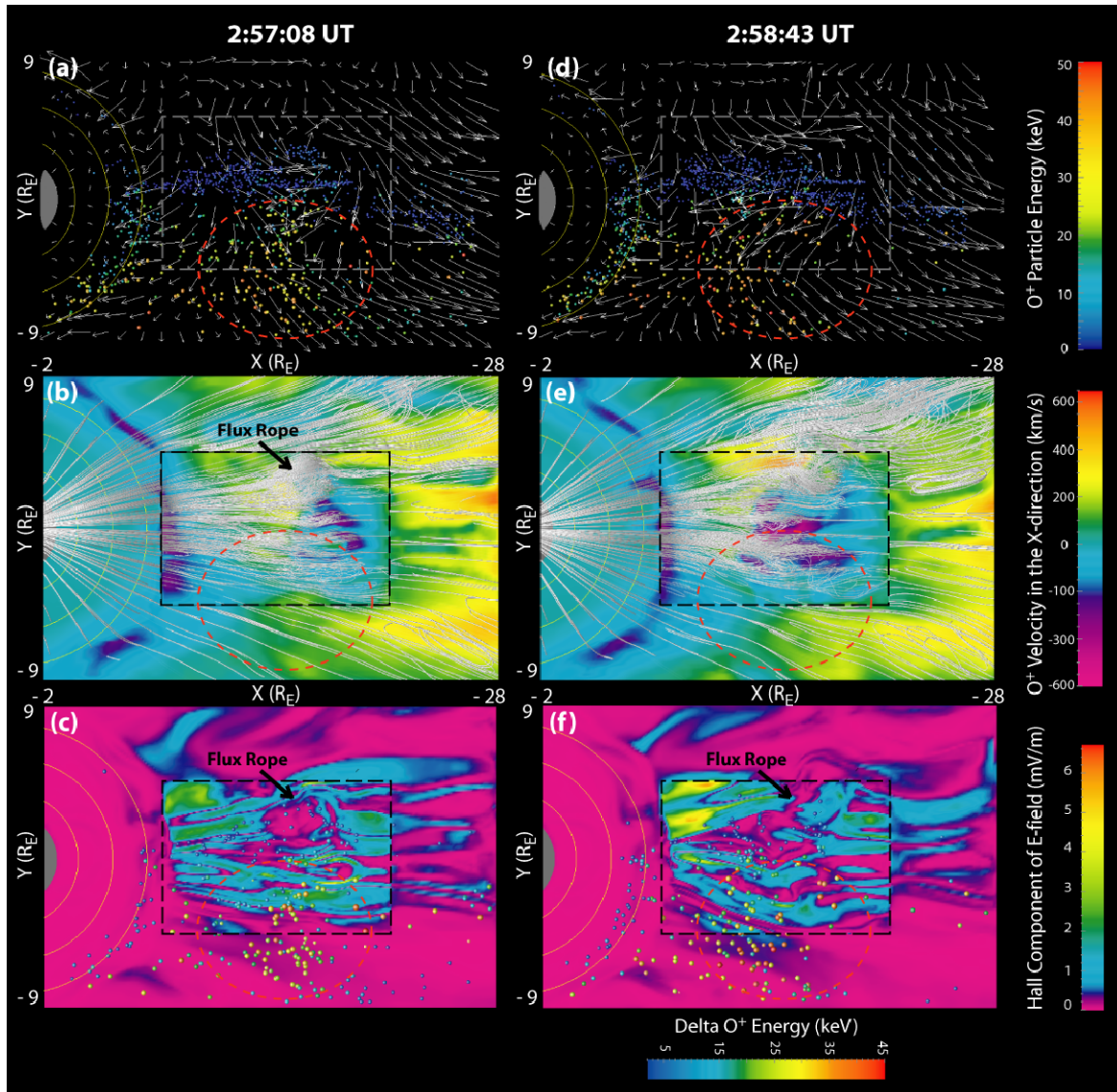


**Figure 4.2** (a) High-resolution image of Figure 4.1c showing particles within  $2 R_E$  of the equatorial plane. The shaded dashed box corresponds to an even higher resolution region. (b) White magnetic field lines are plotted over a contour plot of the  $O^+$  velocity in the  $x$  direction. A large earthward moving flux rope can be seen to extend from the top of the black dashed high-resolution box to the lower edge in a horseshoe shape. The red dashed circle shows the location of particle energization. (c) Particles with  $> 2$  keV change in energy are plotted on a contour plot of the Hall component of the electric field, which shows kinking in the tail current sheet. The region of particle energization is duskward of the noon-midnight meridian and the earthward moving flux rope. (d-f) The flux rope and particle positions at time 1.5 minutes later. The flux rope has moved earthward and the particles in the energization region have moved earthward in a corresponding fashion.

earthward moving flux rope and the relationship between this energization region and the electric and magnetic fields, a higher resolution image of the region of interest is plotted for 0257 UT in Figure 4.2.

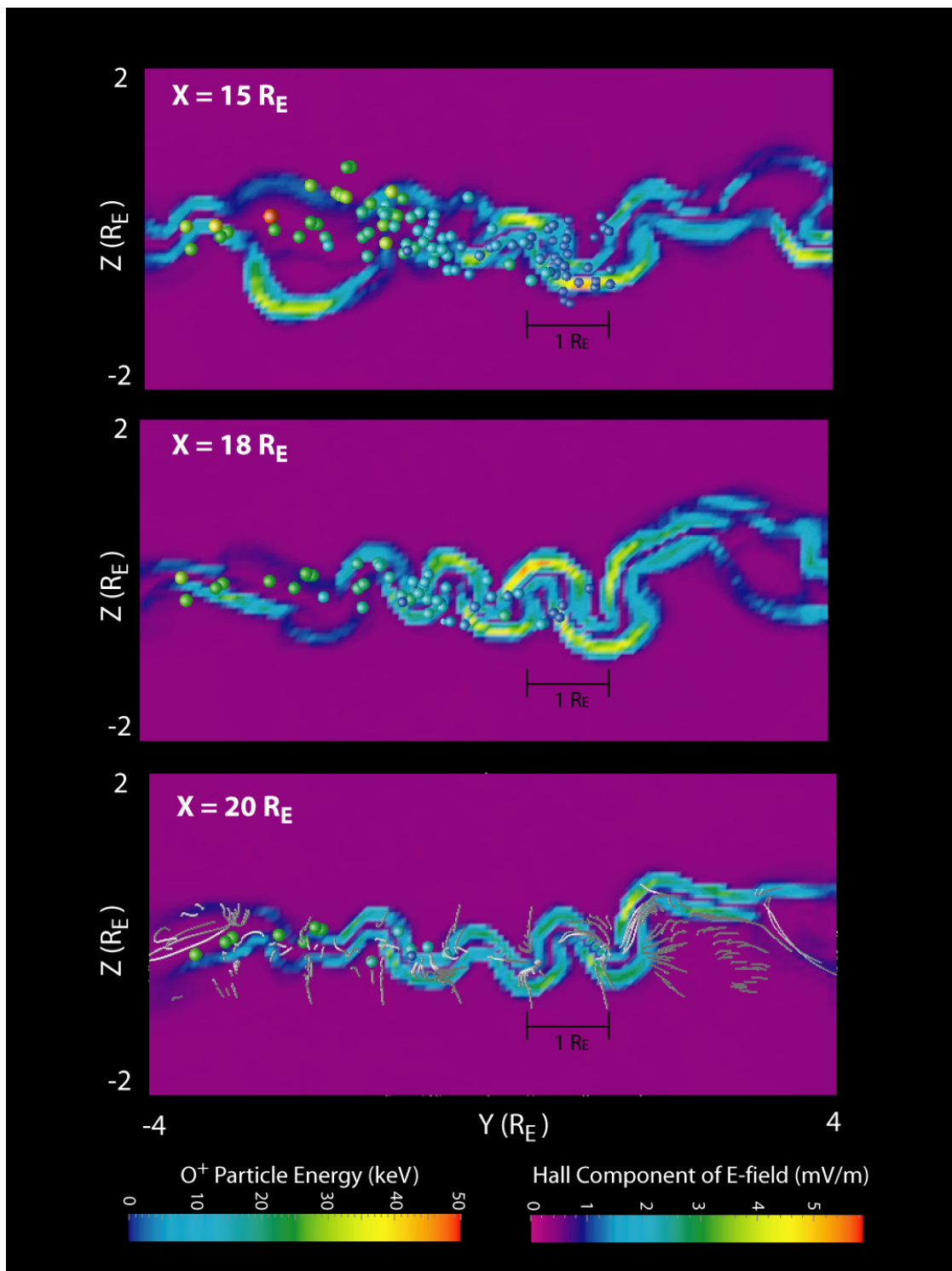
Figure 4.2a shows the same energization region from Figure 4.1g, but the view is limited to the tail for the higher resolution. The particles are color coded for energy and plotted on top of white arrows showing the  $O^+$  velocity flow direction. The shaded dashed box represents a region of highest resolution, 470 km, and the area circled in red is a region where particle acceleration is observed. The bottom two panels explore possible mechanisms for the observed energization. In Figure 4.2b, within the highest resolution region, a large earthward moving flux rope can be seen. There is some overlap between the dusk edge of the flux rope around  $y = -2 R_E$  and the region of energization; however, most particle acceleration is observed duskward of this large flux rope. In Figure 4.2c the same  $O^+$  ions shown in the first panel are plotted, but this time the particles are color coded according to the change in particle energy. Within the high-resolution region, channel-like structures can be observed in the Hall component of the electric field. Here only the Hall component of the total electric field is considered. While particles feel the effects of the total electric field, in this region near the current sheet the Hall term is the largest component of the total electric field. These channel-like structures, which represent kinks in the current sheet, are more clearly illustrated in Figure 4.3 where three downtail cross sections from the high-resolution region have been plotted at 0300 UT, a time 3 minutes after the generation of the large earthward moving flux rope, when the tail kinks have fully developed. Some boundary effects can be observed in Figure 4.2f at the interface between the two grids of differing resolution, but these effects do not affect the interior results of the high-resolution grid.

Figure 4.2 (d-f) shows the location of the flux rope and front of energetic particles  $\sim 1.5$  minutes later. The flux rope has moved  $\sim 2 R_E$  earthward and expanded in the dawn-dusk direction (Figure 4.2e), and the energetic particles are also observed to have moved  $\sim 2 R_E$  earthward during this same time interval. This seems to suggest that the particles are moving with the flux rope and are approaching the earth as a single injection front. As the

earthward-moving flux rope approaches the inner edge of the plasma sheet, the speed of the flux rope increases to 600 km/s [Winglee *et al.*, 2009, Figure 13]. A similar injection feature is not present in the absence of flux ropes.

During periods of southward IMF, a thin current sheet often develops in association with reconnection in the tail region and the formation of flux ropes. Harnett *et al.* [2006] reported that as a flux rope moves downtail, it leaves behind a thin, 1200 km wide current sheet, which is subject to small-scale kinking and twisting. In Figure 4.3 such sinusoidal kinks in the tail are clearly visible in the Hall component of the electric field. The current sheet is bounded above and below by the Hall electric field, which is directed downward above the current sheet and upward below the current sheet, helping to channel positive oxygen ions into the current sheet region by accelerating them toward the current sheet. In this region the  $O^+$  gyroradius is  $\sim 2 R_E$ , much larger than the thickness of the thin current sheet, allowing the oxygen ions to break the frozen-in condition and move independently of the field lines. The  $O^+$  ions follow the sinusoidal path bounded by the Hall electric field as the particles convect duskward due to the cross-tail current. The kinks in the Hall component of the electric field are observed to have a wavelength of  $\sim 1 R_E$  and amplitude of  $\sim 0.6 R_E$ , and as the oxygen ions move through these kinks, they gain energy. Intensifications in the Hall component of the electric field appear to occur on the outer edge of the kinks. Flux ropes forming within the current sheet are also observed to be bounded above and below by the Hall current. These small scale structures within the thin current sheet appear to be important for particle acceleration (see section 4.5 for a discussion of high-resolution results vs. low-resolution results).

A different mechanism is in place for the energization of  $H^+$ . Figure 4.4 shows particle tracking results for  $H^+$  under the same simulation conditions used for the  $O^+$  case: a single injection of 100,000 particles launched at 0220 UT from the nightside in a continuously southward IMF. The majority of the protons are observed to travel downtail where they experience only slight acceleration. Ionospheric protons, which were previously accelerated from their low initial outflow energies to energies of  $\sim 10$  keV, are pushed



**Figure 4.3** Hall component of the electric field as seen from the down tail region ( $X$ - $Z$  plane) showing the kinking of the current sheet at 0300 UT. Once inside the current sheet,  $O^+$  convects duskward following the sinusoidal kinks. Particles are color coded according to their change in energy ( $\Delta E$ ) and as they move duskward (to the left), they gain energy.

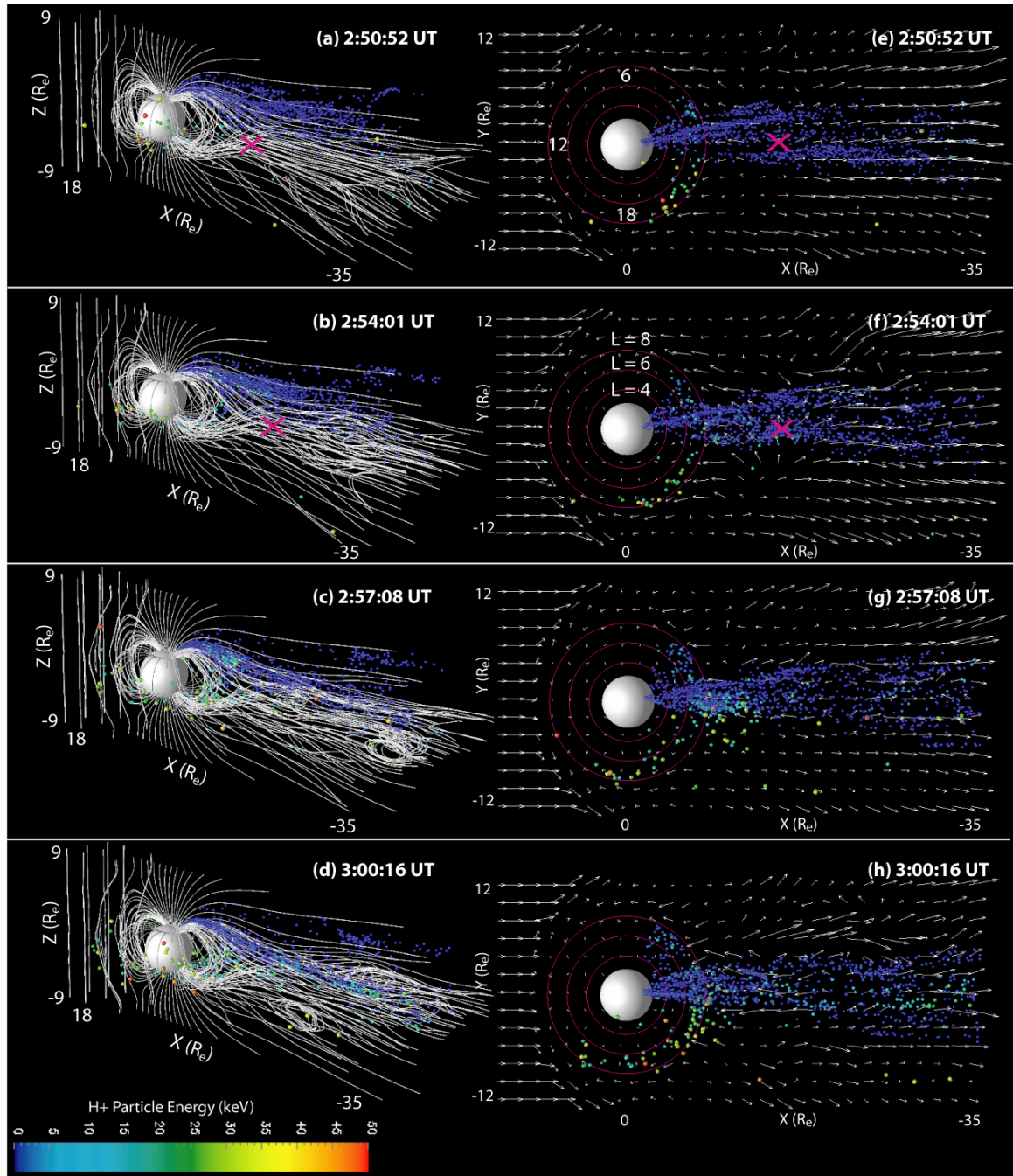


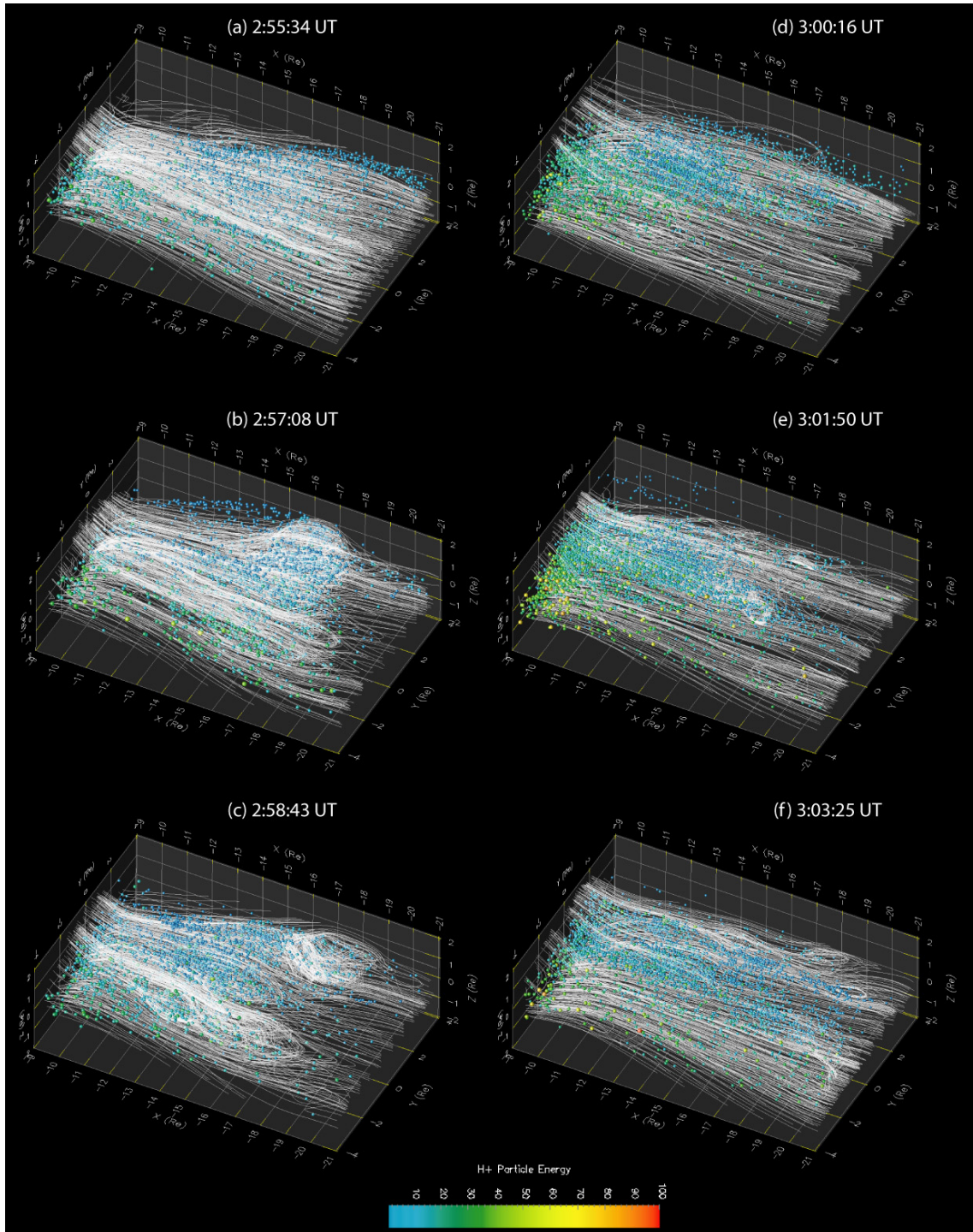
**Figure 4.4** As in Figure 4.1 but this time for proton. Note the asymmetries between the energization of  $H^+$  versus  $O^+$ .

earthward by fast flows from reconnection and become energized to  $>50$  keV by betatron acceleration as they move earthward on closed field lines. Once inside the inner magnetosphere, these energetic protons convect duskward due to  $\nabla B$  and curvature drift.

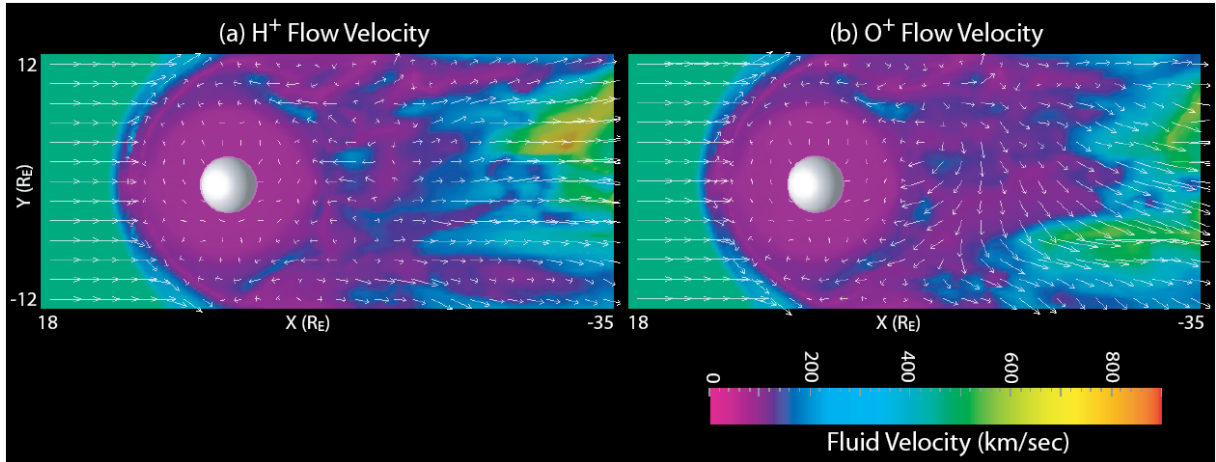
The less energetic protons in the postmidnight sector convect eastward around the earth (Figure 4.4g and Figure 4.4h), as was observed previously for  $O^+$ . During substorm conditions such as those observed at 0257 UT, bursty bulk flows can result in increased particle energization (Figure 4.4g). As the large flux rope at 0257 UT moves earthward, a group of particles moves with the flux rope and is energized by adiabatic compression (betatron acceleration). The correlation between the flux rope and the energization of  $H^+$  can be seen more clearly in Figure 4.5 where 100,000 particles with an average initial energy of 0.08 eV are injected every 2 minutes in a continuous injection.

Figure 4.5a shows protons within the thin current sheet before the formation of the large earthward moving flux rope at  $\sim 16 R_E$  (Figure 4.5b). As the flux rope develops, a large number of particles get trapped within the flux rope and the region tailward of the flux rope becomes depleted of particles. As the flux rope moves earthward, the protons move with the flux rope and are energized as they enter the inner magnetosphere due to betatron acceleration (Figure 4.5d and Figure 4.5e). The arrival of the flux rope at the inner edge of the plasma sheet represents an injection front of particles deposited into the inner magnetosphere at one time. Behind the injection front the region from  $-15$  to  $-20 R_E$  is mainly devoid of particles (Figure 4.5e) until 0303 UT when protons are again seen to populate this region of the tail (Figure 4.5f).

Several noteworthy asymmetries are observed between  $H^+$  and  $O^+$ . Overall, less particle acceleration is observed for  $H^+$  compared to  $O^+$  and the two species appear to be accelerated by different mechanisms:  $H^+$  is energized through betatron acceleration and flows in a field-aligned direction, while  $O^+$  is accelerated by the cross-tail electric field and flows perpendicular to the field. In the multifluid model, the field-aligned flow of  $H^+$  and the cross-tail flow of  $O^+$  are clearly visible (Figure 4.6). The fluid velocity flow vectors depicted in Figure 4.6 illustrate the flow of the  $H^+$  fluid in the positive and negative  $x$  direction and the flow of the  $O^+$  fluid in the negative  $y$  direction.



**Figure 4.5** Time evolution of down tail region where (b) earthward moving flux rope is first observed. Note the large group of particles contained within the flux rope. (c) Particles are seen to move earthward with the flux rope, and (d) the particles have reached the inner edge of the plasma sheet where they are deposited into the inner magnetosphere. Particles plotted have energies  $> 1$  keV. By plotting only the more energetic protons, a group of particles becomes easily identifiable. This group of particles is seen propagate earthward, getting energized and injected into the inner magnetosphere between 0300 UT and 0301 UT. This appears to be an injection front.



**Figure 4.6** Velocity flow vectors for  $H^+$  and  $O^+$  fluids obtained from the multifluid model at 0250 UT. (a) Protons flow mainly in the  $x$  direction, while (b) the bulk oxygen motion in the midtail is in the dawn-to-dusk direction.

The asymmetries observed between  $H^+$  and  $O^+$  energization are consistent with recent THEMIS substorm observations, which detected two discrete components in the ion distribution [Angelopoulos *et al.*, 2008]. One component was aligned with the magnetic field and the other was propagating perpendicular to the field. Using single-particle tracking, we observe protons to move in the field-aligned direction and  $O^+$  to move perpendicular to the magnetic field in the magnetotail (see Figure 4.1 and Figure 4.3), these results are consistent with results observed using only the multifluid model (Figure 4.6). The asymmetry between the two ion species results from the presence of a thin current sheet which enables  $O^+$  to become demagnetized and move in a perpendicular direction (Figure 4.6b), while the motion of  $H^+$  remains in a field-aligned direction (Figure 4.6a). The high-resolution capabilities of the model allow us to resolve this thin current sheet, and observe the asymmetries between the heavy and light ion species.

#### 4.4 Northward Turning of IMF

Having demonstrated the ability of our model to energize ionospheric particles and produce an injection front in association with an earthward moving flux rope, we now investigate the conditions that lead to particle trapping and the formation of the asymmetric

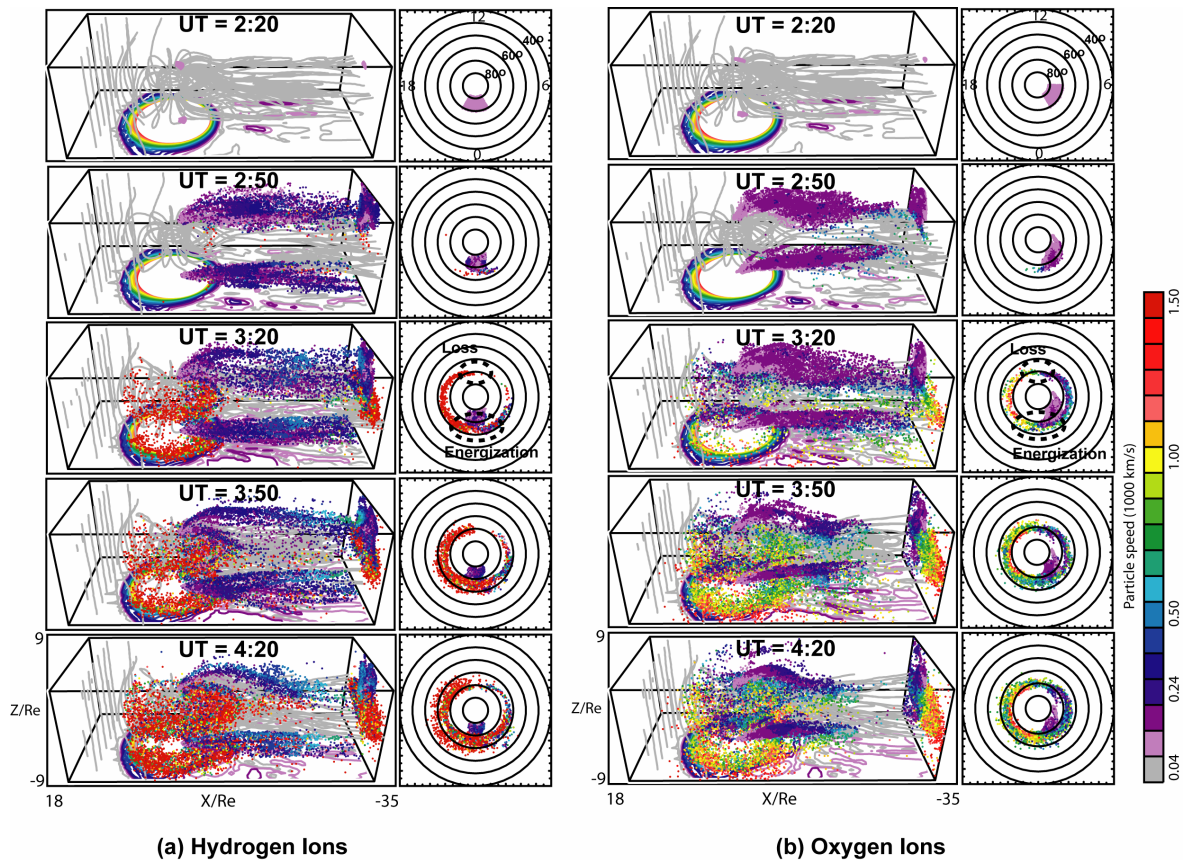


**Figure 4.7** Time evolution of ionospheric (a)  $\text{H}^+$  and (b)  $\text{O}^+$  for the case when the interplanetary magnetic field (IMF) is southward for the entire run. Shaded lines represent the Earth's magnetic field lines. Color contours projected on the bottom of the box represent the pressure, and the speed of the particles is given by the color of the particle. To the right of each 3D box is a projection of the particles mapped back to Earth with the inner circle at  $80^\circ$  and the outermost circle at  $30^\circ$ .

and symmetric components of the ring current. In order to determine if test particles accelerated in a continuously southward IMF would eventually form a symmetric ring current, we continuously injected ions in a constant southward solar wind for 2 hours. Protons were injected from auroral latitudes between 22 to 02 MLT and from an altitude of  $3.5 R_E$ , while  $\text{O}^+$  ions were injected slightly dawnward of midnight from 02 to 06 MLT. The difference in  $\text{H}^+$  and  $\text{O}^+$  injection locations were chosen in order to optimize observed particle energization for the given solar wind conditions during quiet periods when  $\text{O}^+$  is observed to gain energy through cross-tail convection and  $\text{H}^+$  is accelerated through adiabatic heating. As discussed in section 4.3, during substorm conditions, particle acceleration for both species takes place between 0257 to 0302 UT in the midnight and post-dusk sectors for the present idealized case.

For both  $H^+$  and  $O^+$ , energetic particles are observed to drift westward to the dayside where the particles encounter the dayside magnetopause reconnection region near the subsolar point and are lost over the polar cap as the ions move onto field lines convecting over the polar cap (Figure 4.7). The less energetic ions are observed to move eastward around the Earth, but once they encounter the dayside magnetopause, they are also lost over the polar cap. In Figure 4.7b, these two populations of ions are clearly visible: a less energetic population convecting through dawn to noon and a more energetic population convecting through dusk to noon. While it may look like a symmetric ring current is formed, what is actually observed is the two oppositely directed populations of energetic and less energetic oxygen ions drifting in opposite directions and converging at the dayside magnetopause. Neither population is observed to convect past noon as evident by the continued segregation of these two populations even 1 hour after they initially both reach 12 MLT. Once on the dayside, both populations of  $O^+$  are lost over the polar caps for the continuously southward IMF case. During periods of southward IMF the dayside reconnection region moves into  $\sim 10 R_E$ , field line merging occurs, and the particles convect over the polar caps and downtail. Even 2 hours after the initial particle injection, only an asymmetric ring current is present and a symmetric ring current has not formed as particles continue to be lost upon encountering the dayside reconnection region. Thus, a continuously southward IMF appears to allow for particle acceleration but does not allow for particle trapping, suggesting that an investigation into the effects of rotations in  $B_z$  on particle trajectories is necessary.

To determine what conditions lead to trapping of energetic particles in the ring current, the effect of IMF orientation on test particles trajectories was explored by varying the direction and strength of the  $B_z$  component of the solar wind. Several cases were examined with  $B_z$  initially  $-5$  nT in all cases (0200 UT). The solar wind was turned northerly to 0 nT at 0232 UT (case A), 0244 UT (case B), 0257 UT (case C), and 0313 UT (case D). For the two earliest northerly turnings, 0232 and 0244 UT, not enough time has passed since the launch of particles at 0220 UT to allow for particle energization. The field orientation is changed

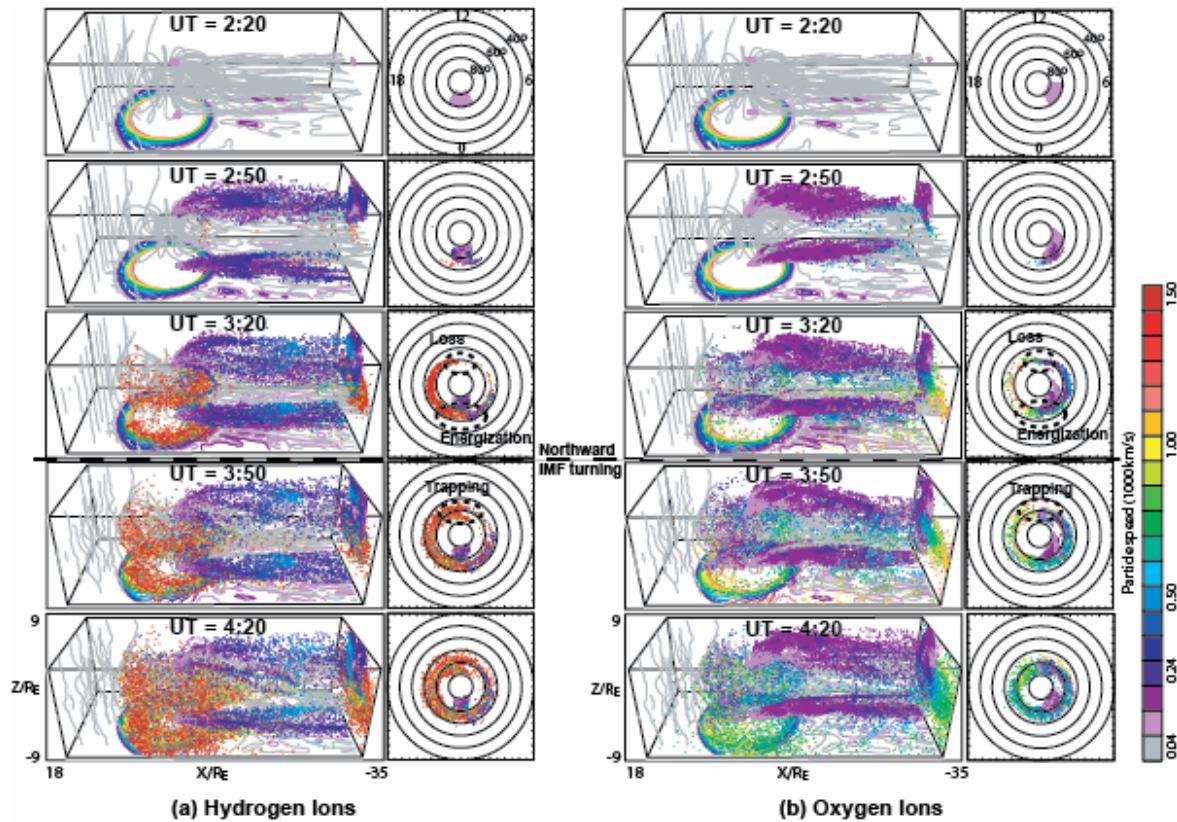


**Figure 4.8** Time evolution of ionospheric (a)  $H^+$  and (b)  $O^+$  for case when IMF turns northward to 0 nT at 0310 UT. Notice that after the northerly turning of the IMF, energetic ions are observed to convect past noon forming a symmetric ring current by 0420 UT.

before the large earthward-moving flux rope, which forms at 0257 UT (for a substantial southward IMF), is able to move through the magnetosphere and interact with the particles to energize them. Thus, for these two cases, little particle energization is observed. For the cases when the field orientation turns to 0 nT at 0257 and 0313 UT, the large earthward moving flux rope and small-scale structures in the thin current sheet are able to energize the particles before the new IMF conditions reach the Earth. This allows time for the particle energization before the arrival of the  $B_z = 0$  nT field. About 15–20 minutes after the northward turning of the IMF in each of these cases, energetic particles are observed to convect past noon. This effect is illustrated in Figure 4.8 where after an initial period of southward IMF, the IMF is switched northerly to 0 nT at 0313 UT, ~50 minutes after the initial particle injection. At 0320 UT particles continue to be lost in the dayside reconnection region because the  $B_z = 0$  nT front takes ~9 minutes to arrive at the

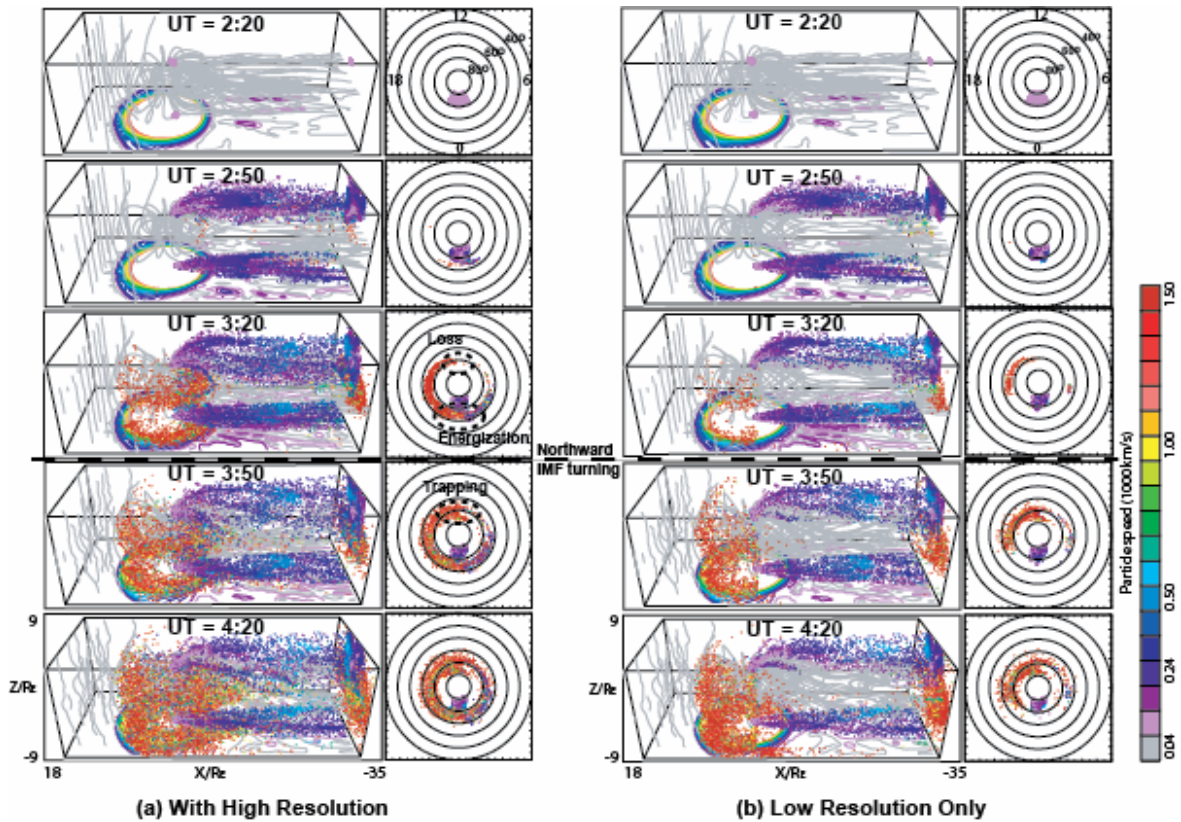


**Figure 4.9** Time evolution of ionospheric  $H^+$  for the same case as Figure 4.8, IMF northward turning at 0310 UT. (a) High-resolution capabilities are included. (b) Only low-resolution grids are used, and the formation of a symmetric ring current is not observed at 0420 UT as it is when high-resolution gridding is included.

magnetopause. By 0350 UT, energetic particles have begun to convect past noon, where they were previously lost over the polar cap in the continuously southward case (Figure 4.7), and by 0420 UT energetic particles have begun to form a symmetric ring current. The energetic ions are able to convect past noon because during periods of northward IMF, the dayside magnetopause moves out to  $\sim 13 R_E$ , the reconnection rate on the dayside is reduced, and the polar cap shrinks. Thus, in order to trap the particles, a northerly turning of the IMF is necessary to move the dayside reconnection region outward, allowing the ring current particles to remain on closed trajectories in confirmation with findings by *Kozya et al.* [2002].

While asymmetries are observed between  $H^+$  and  $O^+$  energization mechanisms, both species respond in a similar manner to rotations in solar wind  $B_z$ . Both ions experience

trapping when the IMF is turned in a northerly direction as observed when  $B_z$  is increased from  $-5$  to  $0$  nT (Figure 4.8).

In all four cases we find that as long as sufficient time has elapsed to allow structures in the electric and magnetic fields to accelerate the particles (such as flux ropes and a thin, kinked current sheet), then the timing of the northward turning is not as important as the turning itself and  $\sim 18$  minutes after the turning, the dayside loss region is sealed off and energetic particles are effectively trapped.

While the northward turning of the solar wind  $B_z$  appears to play a critical role in the trapping of energetic ions, the degree of northward turning does not seem to be as important. The same conditions used for Figure 4.8 were used again, but this time a stronger degree of northward turning ( $5$  nT compared to the  $0$  nT from above) was used. The results for these two cases are nearly identical with only subtle differences, indicating that a reduction in the cross-polar cap potential of as small as  $50\%$  is needed to reduce dayside convection and allow the formation of a symmetric ring current.

#### **4.5 Resolving the Thin Current Sheet**

To determine whether the high resolution in the downtail region of the model affects particle acceleration and energization, two of the above cases were tested again using only low resolution in the tail, equivalent to that around the Earth ( $0.3 R_E$ ) instead of the higher  $470$  km resolution used previously (see section 4.2). Figure 4.9 shows the importance of being able to resolve small-scale structures with high-resolution capabilities, showing identical times to Figure 4.8. If resolving small-scale features did not significantly contribute to the acceleration of the particles, the results for both cases would be similar. However, as can be seen in Figure 4.9b, protons are not energized in the tail during the periods of southward IMF as in the previous cases (Figure 4.9a). Instead, the hydrogen ions convect across the tail and are energized when they encounter hot plasma in the low-latitude boundary layer (LLBL). Even after the northerly turning of the IMF, a symmetric ring current is not formed in the low-resolution case (Figure 4.9b).

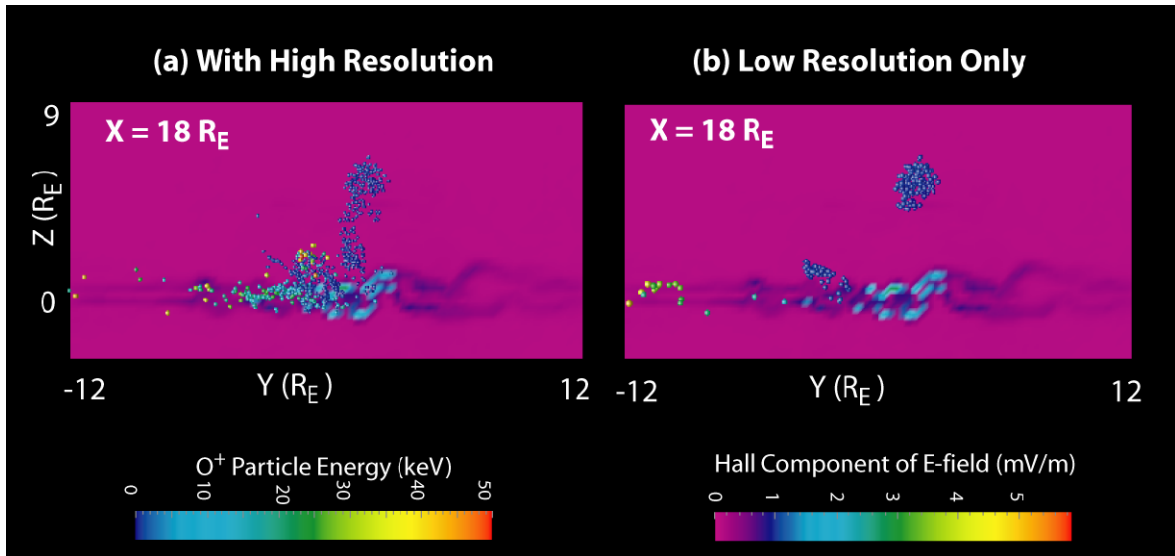


**Figure 4.10** Hall component of the electric field as seen from the down tail region ( $X$ - $Z$  plane) showing the kinking of the current sheet, but this time as observed with a resolution of  $\sim 0.3 R_E$ . (a) shows oxygen ion with high resolution and (b) shows the same run using only low resolution. The particles do not enter the current sheet or follow the kinks as observed in Figure 4.3. Instead three groups of ions are observed: a group of low-energy particles convecting downtail which can be seen above the current sheet; a group of low-energy particles just duskward of midnight slightly above the current sheet; and a group of particles on the duskward side of the image which have encountered the low-latitude boundary layer (LLBL) and gained energy. In contrast, in Figure 4.10a, the same box is shown, this time with particles that have been allowed to interact with the high-resolution region in the tail. These particles make it into the current sheet and can be seen to convect duskward within the current sheet. There is also a low-energy population of particles above the current sheet, but these particles are observed to convect southward and into the current sheet. Particles are color coded according to their change in energy ( $\Delta E$ ).

Similarly  $O^+$  experiences less downtail and cross-tail acceleration. Figure 4.10a and Figure 4.10b show the Hall component of the electric field in a cross-tail plane at  $18 R_E$  for the high-resolution and low-resolution cases, respectively. With only low resolution, the  $O^+$  crossing of the thin current sheet is not well resolved and oxygen ions are not observed to gain energy as they convect duskward. Instead, it is not until the oxygen ions reach the LLBL that they are accelerated (Figure 4.10b). No oxygen ions enter the ring current between 18 and 24 MLT in the low-resolution case, and thus a symmetric ring current cannot form. These results suggest that particles forming the ring current are accelerated by small-scale processes within a thin current sheet ( $< 1000$  km) and that simulations with only coarse-grid resolution observe a different acceleration mechanism for ring current particles.

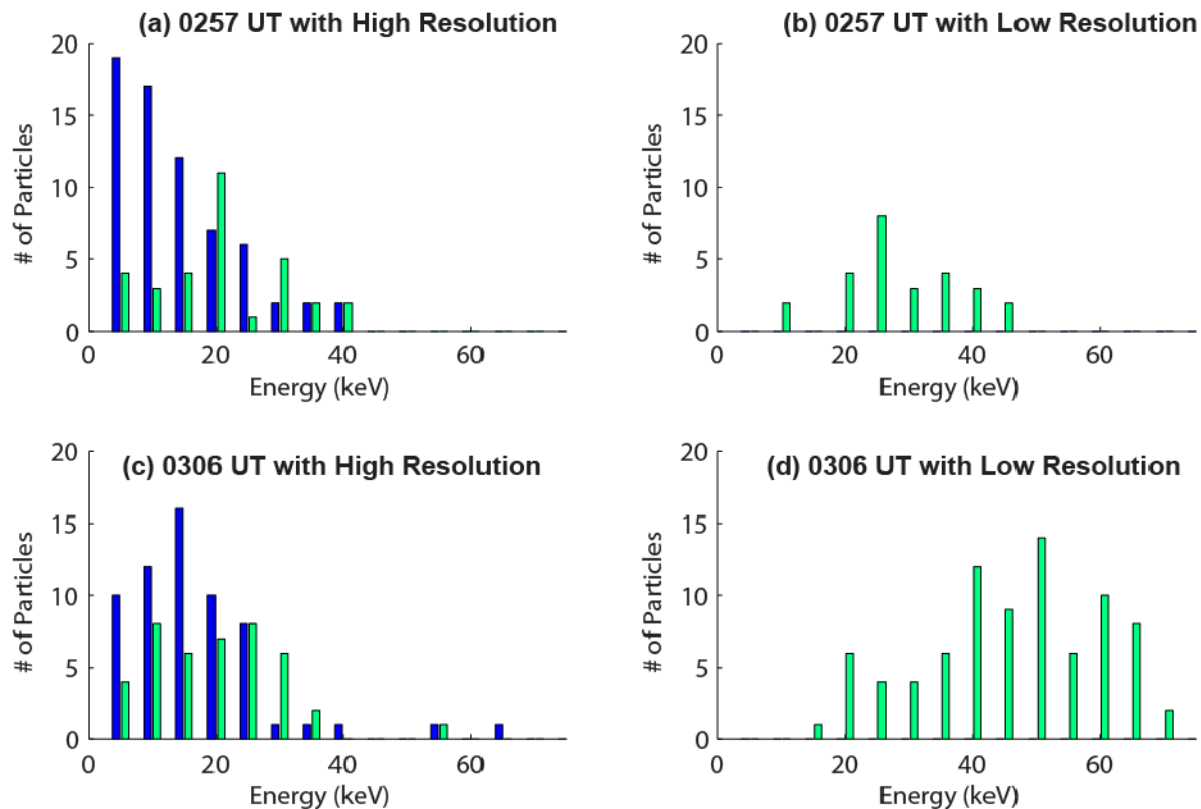


**Figure 4.11** Number of oxygen ions in the tail (blue) and in the ring current (green) for two different times potted as a function of energy. The tail region considered extends from 15 to 25  $R_E$  in the  $x$  direction, from  $\pm 2.5 R_E$  in the  $y$  direction, and from  $\pm 0.3 R_E$  in the  $z$  direction. The ring current region in these images is defined as extending in L-shell from 4 to 8  $R_E$ , and from  $\pm 0.3 R_E$  in the  $z$  direction. Results are approximately 30 minutes after particles are launched (a) in the high-resolution simulation and (b) in the simulation with low resolution only. Approximately 10 minutes later (c) ions in the tail of the high resolution case are observed to have gained energy, while (d) in the low-resolution simulation no particles are observed in the tail. With only low resolution, the oxygen ions are not observed to gain energy until later in the simulation when they reach the LLBL and then they achieve a high level of energization.

This difference between energization regions is depicted graphically in Figure 4.11 where oxygen ions in the tail and the ring current are plotted as a function of energy for two different times. The first time is at 0257 UT, approximately 30 minutes after the particles are launched from the ionosphere. In the high-resolution simulation (Figure 4.11a) particles are observed both in the tail (blue lines) and in the ring current (green lines). The majority of the particles in the tail have lower energies than the ring current particles. The tail region considered in this analysis extends from 15 to 25  $R_E$  in the  $x$  direction, from  $\pm 2.5 R_E$  in the  $y$  direction, and from  $\pm 0.3 R_E$  in the  $z$  direction, while the ring current region

considered here is limited to L-shells from 4 to 8  $R_E$  in the radial direction and from  $\pm 0.3 R_E$  in the  $z$  direction. At 0257 UT in the simulation with low-resolution only (Figure 4.11b), no particles are observed in the tail, instead particles are only observed in the ring current region. These ring current particles are slightly more energetic than those observed in the high-resolution simulation. Approximately 10 minutes later at 0306 UT, the oxygen ions in the tail of the high-resolution case are observed to have gained energy with the peak energy increasing to  $\sim 15$  keV (Figure 4.11c). The particles in the ring current have also been observed to gain slightly more energy. In the low-resolution simulation at 0306 UT (Figure 4.11d), the tail remains devoid of particles; however the particles in the ring current region have increased in number and have achieved substantially higher energies of  $\sim 50$  keV. This suggests a different acceleration mechanism is responsible for acceleration ring current particles in the low-resolution case, which as suggested previously, likely occurs when the oxygen ions reach the LLBL instead of some of the particle energization occurring in the tail region.

In order to obtain an accurate picture of the mechanisms involved particle energization, the detailed structure of thin current sheets must be fully resolved by simulations, as in our multifluid-multiscale model [Harnett *et al.*, 2006]. A multiscale model that can fully resolve the thinning of the current sheet and the disturbances by tail current sheet kinking predicts a different sequence of particle energization. The oxygen ions need to experience multiple encounters with the small-scale kinks in order to gain energy in the thin current sheet. When underresolved (Figure 4.10b), the peak magnitude of the electric field and current structures is smaller because the peak intensities are averaged over several grid points of the higher-resolution simulations. In the low-resolution case, the peak intensities are spread out over a larger area so that neither the small-scale structures nor the large intensities can be identified. Cluster spacecraft data recently demonstrated the thinning of the current sheet from about 1  $R_E$  down to about 400 km [Nakamura *et al.*, 2002], further supporting the need for high-resolution capabilities in order to see the effects of these small-scale structures in a global model.

Using 470 km as the finest resolution in this study has produced significant differences, thus the question can be asked whether this resolution is in fact adequate in order to capture all of the relevant small-scale processes that play a role in particle energization and injection in the ring current region. Perhaps employing even higher resolution grids would yield even better results. While it would be ideal to include even higher resolution or to expand the size of the highest resolution grid, the increased resolution would significantly slow down the multifluid code. Weighing the potential benefits of including even higher resolution to the limitations imposed by significantly slowing down in the multifluid code is critical when deciding upon grid size and resolution. Given our ability to resolve the thin current sheet and the sinusoidal kinks within the current sheet, a resolution of 470 km seems adequate for the purposes of this study. Before increasing the resolution further, the author suggests expanding the size of the high-resolution grids to include more of the inner magnetosphere and not having high-resolution capabilities only in the tail. Including high resolution in the inner magnetosphere may result in enhanced field strength in this area, which is a region in which the multifluid model consistently underpredicts the strength of Earth's magnetic field.

#### **4.6 Calculated Particle Flux**

In order to quantify the model results, the energy flux for ring current particles in our model is compared with expected values from observations and theory. To obtain a realistic, quantitative value for the energy flux of particles injected into the ring current region, we first correlate the rate at which ions are injected into the simulation with observed rates for ion outflow. Several studies have addressed bulk ion outflow rates for the auroral zones [*Collin et al.*, 1984; *Shelley*, 1985; *Yau et al.*, 1985; *Chappell et al.*, 1987; *Yau and Andre*, 1997]. *Collin et al.* [1984] used S3-3 satellite data to determine the total outflow rate for  $H^+$  and  $O^+$ , but were limited to energies between 0.5 and 16 keV due to the low-energy threshold of the spectrometer. *Yau et al.* [1985] used data from the Dynamic Explorer 1 (DE 1) spacecraft to repeat the work done by *Collin et al.* [1984] but for lower energies, down to 10 eV. With this expanded energy range, *Yau et al.* [1985] obtained outflow rates that were 2.5 to 5 times larger than those obtained by *Collin et al.*

[1984]. These results indicated the dominance of 10–500 eV ions in the upward ion flows. Ions with energies <1 keV were found to be the most prevalent with 1–17 keV ions contributing less than 10% of the total ion outflow. Outflow from the auroral regions was determined to be greater than polar cap ion outflow.

These previous works are summarized by *Chappell et al.* [1987] who, after subtracting out the cleft ion fountain contribution, determined the bulk ion outflow to be between  $2.6 \times 10^{25}$  and  $3.3 \times 10^{25}$  ions/s for active conditions, during solar minimum and during solar maximum respectively, for the auroral zone. This work was expanded upon by *Yau and Andre* [1997], who also examined the sources of ion outflow and determined that the bulk flow occurs at auroral latitudes from 400 to 1500 km altitudes or higher, at velocities up to  $\sim 1$  km/s and outflowing fluxes up to  $10^{13} \text{ m}^{-2}\text{s}^{-1}$ . Their results give ion outflow rates for  $\text{H}^+$  and  $\text{O}^+$  at 0.01–17 keV integrated over all MLT and invariant latitude above  $56^\circ$  in both hemispheres as a function of magnetic  $Kp$  index. For active times ( $3 \leq Kp \leq 5$ ), total ion outflow ( $\text{H}^+$  and  $\text{O}^+$ ) was determined to be around  $1.5 \times 10^{26}$  ions/s, while for quiet times ( $Kp \leq 2$ ), total outflow was  $5 \times 10^{25}$  ions/s [*Yau et al.*, 1985].

In these simulation, ions are injected at latitudes between  $55^\circ$  and  $75^\circ$  in the auroral zone, which has been shown to be a significant contributor to the plasma sheet and ring current [*Collin et al.*, 1984; *Shelley*, 1985; *Yau et al.*, 1985; *Chappell et al.*, 1987]. The auroral zone source is also relatively energetic compared to other ionospheric sources such as the cleft ion fountain, polar cap, and polar wind, with outflowing ions having energies in the 10 eV to 10 keV range. The particles are initialized with an initial injection energy of <0.1 eV, which is at the lower end of typical energy range of outflowing auroral zone ions, and are injected over a period of 6 hours MLT centered at midnight at an altitude of  $3.5 R_E$ . In order to compare with observed values, the particle results are scaled with each particle multiplied by  $2 \times 10^{21}$  ions. Within the simulation, 100,000 particles are continuously injected into an area  $1.165 \times 10^8 \text{ km}^2$  in the nightside auroral region every 6 minutes, giving an injection rate of  $\sim 5.2 \times 10^{24}$  ions/s, which is in line with typical outflow values during quiet times [*Collin et al.*, 1984].

**Table 4-1** Simulation results obtained at 0310 UT for a minor isolated substorm during a time of relatively low magnetic activity compared to values obtained from satellite observations during magnetically quiet times with *Dst* values ranging from between  $\sim 1$  nT to  $-25$  nT.

Parameter	H <sup>+</sup> Particles	O <sup>+</sup> Particles	H <sup>+</sup> Observation	Reference
Average energy (keV)	27.4	37.1	10-30	<i>Lui and Hamilton [1992]</i>
Energy density (erg/cm <sup>3</sup> )	$5.15 \times 10^{-10}$	$7.88 \times 10^{-10}$	$9.00 \times 10^{-8}$	<i>Frank [1967]</i>
Current density (nA/m <sup>2</sup> )	$6.71 \times 10^{-2}$	$1.027 \times 10^{-1}$	1-4	<i>Lui and Hamilton [1992]</i>

The composition of the ring current during storm and substorm conditions has been explored in several papers [*Frank, 1967; Lui et al., 1987; Lui and Hamilton, 1992; De Michelis et al., 1997*]. The ring current consists of energetic ions between 1–200 keV at distances from 2.5 to 8  $R_E$  [*Lui et al., 1987*]. During solar minimum, H<sup>+</sup> ions with energies of 20 to 200 keV make up the majority of the ring current system [*De Michelis et al., 1997*]. During moderate storms, the ring current energy density is contributed mainly by protons in the 20 to 300 keV energy range with 70%–85% of the ring current energy density carried by 25 keV to 1 MeV ions [*Lui et al., 1987*]. During intense storms, ionospheric O<sup>+</sup> ions have been shown to become the dominant species in the ring current, contributing more than 70% of the total energy density [*Daglis et al., 1999a*], with typical oxygen contribution during storm time of  $< 50\%$ . According to *Frank [1967]*, protons with energies  $> 100$  keV do not significantly contribute to the ring current energy density and have been shown to be insufficient by at least an order of magnitude for explaining the observed decrease in Earth's surface magnetic field during geomagnetic storms.

Table 4-1 gives the model results for ring current values for H<sup>+</sup> and O<sup>+</sup> compared to observations for protons. The simulation values were obtained using the same injection rate for H<sup>+</sup> and O<sup>+</sup>. All the flux values are calculated in one quadrant of a toroidal region between 18 and 24 MLT at a radial distance of 6 to 8  $R_E$ . This distance range was selected in order capture the majority of the particles in the simulation, which at this time during the simulation are at higher L-shells. Varying solar wind conditions are necessary for the particles to move inward, but the results presented in this section are for a continuously

southward IMF. Peak flux values for protons were observed in the simulation at 0310 UT, 11 minutes after the large earthward moving flux rope reaches the inner edge of the plasma sheet depositing energized particles into the inner magnetosphere. Peak flux values for oxygen ions were observed 2 minutes later at 0312 UT. These peaks correspond with the injection of energetic particles from the injection front. For both  $H^+$  and  $O^+$ , the injection front reaches 18 MLT at 0315 UT. After the passage of the injection front, a decrease in particle density is observed, followed by a second increase ~20 minutes (0320 UT) after the earthward moving flux rope reaches the inner edge of the plasma sheet. The region behind the flux rope has been depleted of particles (see Figure 4.5) and it takes a few minutes before the continuously injected particles fill this region again and a corresponding increase in the flux density is observed.

For both ion species the average energy is within the observed range; however, the model energy density and current density are each about two orders of magnitude lower than the observed values. In these results, the processes described above produce the expected energization levels of individual ions typically accompanying magnetospheric activity, while the values for the fluxes are smaller than expected. A number of reasons could account for the lower densities, including assumptions behind the ion outflow rate normalization. The observed outflow rates were measured over all MLT and invariant latitude above  $56^\circ$  in both hemispheres. Here we consider the ionospheric outflow to originate from a wedge-shaped region in the midnight sector, and assume that the observed outflow rate is uniform over all MLTs and take only a subset of the observed outflow area. Thus, a larger ion injection area may need to be considered.

The fact that these results for an isolated substorm produce the energization of individual ions suggest the accuracy of the model in predicting physical quantities such as magnitude and location of enhancements in the electric field and current density in the tail. The result that the fluxes are low is consistent with the fact the predicted ionospheric outflow rates from fluid models for substorms are typically lower by an order of magnitude for  $H^+$  and nearly two orders of magnitude for  $O^+$  for storms. Our results are consistent with those noted in the introduction that  $O^+$  is the primary current carrier of the ring current.

## 4.7 Summary

The generation of the terrestrial ring current has been investigated using single-particle tracking and time-dependent global magnetic and electric fields from multifluid simulations. Observing the energization and trapping of different ionospheric ions, we determined the following.

(1) For particle energization, as expected, the structures within the electromagnetic fields are more important in determining when particles get accelerated than the time elapsed since particles were launched from the ionosphere. For a continuously southward IMF, test particle acceleration is observed corresponding to substorm development noted by the presence of a large earthward moving flux rope and a thin, kinked current sheet. Flux ropes and the thin current sheet formed during substorms appear to be associated with particle acceleration.

(2) Small-scale structures such as the kinks in the thin current sheet also appear to play a role in particle energization. The thin current sheet is bound above and below by the Hall component of the electric field, which acts as a boundary for  $O^+$  convecting across the tail. As the particles convect duskward through the kinking current sheet they gain energy. The largest intensification of the Hall term appears on the outer edge of the kinks. When the kinks are underresolved, the peak magnitude of the Hall current is smaller. In order to resolve the kinks, the resolution must be able to capture a wavelength of  $\sim 1 R_E$  and amplitude of  $0.6 R_E$ . High-resolution capabilities in the model are important, as evidenced by substantial differences between low-resolution and high-resolution results. In the low-resolution simulations, particles are not energized in the tail by small-scale plasma structures as observed in the high-resolution case, but rather the particles are only energized when they are near the low-latitude boundary layer. Using solely low-resolution grids, ring current formation was not observed.

(3) During substorms asymmetries are observed between ionospheric  $H^+$  and  $O^+$  acceleration mechanisms. Once in the current sheet, oxygen ions, due to their large gyroradius, move in the dawn-to-dusk direction according to the electric field, while

protons move earthward on reconnecting field lines. This results in  $H^+$  flowing in a field-aligned direction, while  $O^+$  flows perpendicular to the field. These two perpendicular ion streams could explain the two separate ion components observed by THEMIS, one flowing in a field-aligned direction and the other perpendicular to the field.

(4) After the particles have been accelerated during an initial period of southward IMF, a northward turning of the IMF is required in order to trap energetic particles and allow them to convect past noon. During periods of southward IMF, the magnetopause is compressed to about  $10 R_E$  and energetic particles convecting around Earth encounter the dayside reconnection region, where they are lost over the polar cap. Once the IMF turns northward, the magnetopause moves out to about  $13 R_E$ , the reconnection points move to higher latitudes, and less total reconnection occurs. Such conditions allow particles, energized during southward IMF, to become trapped and convect beyond the dayside reconnection region. While a northward turning appears to be essential for particle trapping, the magnitude of the northward turning does not significantly affect ring current formation. Only subtle differences are observed between the northerly turning case ( $-5$  to  $0$  nT) and the strongly northward turning case ( $-5$  to  $5$  nT), suggesting that as long as the degree of northward turning is sufficient to allow enough expansion of the magnetopause for particles to convect past noon, stronger northward  $B_z$  does not appreciably affect the degree of particle trapping.

(5) Particle energization in this model produces the observed energies, but the energy and current densities are two orders of magnitude smaller than those associated with average periods of low activity. Since we consider only a substorm, we expect these values to be slightly lower than storm-time values, and these results are consistent with the smaller outflows that are typically associated with isolated storms. These results show that even for an isolated substorm,  $O^+$  can be the dominant current carrier for the ring current. The next chapter addresses differences observed during the storm time production of ring current ions.

## Chapter 5: Storm Time Production of Ring Current Ions

This chapter examines the contribution from various ionospheric source regions to the storm time ring current (RC) and the effect of IMF  $B_z$  on producing a symmetric ring current. The 10 March 1998 storm is modeled using single-particle tracking in combination with time-dependent global magnetic and electric fields obtained from multifluid simulations. The energization, injection, and trapping of both  $H^+$  and  $O^+$  from various ionospheric source regions are explained for this storm. Two sets of analysis are performed: (1) identifying the effects of  $B_z$  on injection, energization, and trapping of ring current particles during the two different times of ring current enhancement comparing ionospheric  $H^+$  and  $O^+$  and (2) taking into account the relative outflow rates for the various sectors of the ionosphere in order to understand the dominant ionospheric species contributing to the ring current energy density, the primary ionospheric source regions that contribute particles and energy to the storm-time ring current, and how these vary over the course of the storm.

In the first part of this chapter, the relevant solar wind conditions for generating storm-time ring current particles are examined, focusing on the  $B_z$  component of the IMF and looking at the effects from several different ionospheric source regions including the midnight, predawn, midmorning, and noon sectors at both high and low latitudes. The efficiency of  $H^+$  and  $O^+$  ion contributions to the storm time ring current are compared by launching equivalent numbers of ions from the ionosphere in order to determine the most geo-optimal locations from which outflowing ionospheric particles enter the ring current during the development of the storm.

In the second part, relative ionospheric outflow rates are used to investigate how the contribution to the total ring current energy density from various sectors of the ionosphere changes over the course of the storm. Model values for the relative contribution of  $H^+$  and

$O^+$  to the total ring current energy density are compared with spacecraft data for several storms reported by *Daglis et al.* [1996]. Plots indicating the ionospheric sectors that contribute most to the ring current in terms of energy and density are shown, illustrating how the dominant source of ring current particles and the ionospheric regions that attain the highest levels of particle energization vary during storm development. These results increase the overall understanding of how ionospheric outflow relates to the development of the storm time ring current. Material in this chapter was originally published in the *Journal of Geophysical Research – Space Physics* and is reproduced with permission of the American Geophysical Union [Cash et al., 2010b].

## 5.1 Overview

Using single-particle tracking with time-dependent global magnetic and electric fields from multifluid simulations, the 10 March 1998 storm is modeled to investigate storm time acceleration, injection, and trapping mechanisms associated with the formation of the ring current. The contribution from various ionospheric source regions to the storm time ring current and the effect IMF  $B_z$  has on producing an asymmetric and symmetric ring current is examined. This work leads to producing the first maps for the relative importance of ionospheric outflow ( $H^+$  and  $O^+$ ) regions as a function of all magnetic local times (MLTs) and latitudes between  $60^\circ$  and  $80^\circ$ . During the early part of the storm, high latitude outflow regions between 00 and 06 MLT are the most efficient sectors at contributing particle density to the ring current, while during the main phase of the storm, there is more even contribution from all MLTs. The sectors that contribute the majority of the energy are primarily the high-latitude regions between 03 and 09 MLT. An increase in the contribution of  $O^+$  to the current density is observed from the predawn high-latitude region during each of two decreases in  $Dst$  examined for the 10 March 1998 storm, supporting the central role oxygen plays in storm development. Asymmetries are observed between  $H^+$  and  $O^+$  contributions to the ring current energy density and the dominant ionospheric species contributing to the ring current energy density is shown to vary during the course of the storm with a significant increase in ionospheric  $O^+$  contribution to the ring current associated with large decreases in  $Dst$ .

## 5.2 Boundary and Initial Conditions

The simulations presented here use single-particle tracking to follow the transport and energization of ionospheric  $H^+$  and  $O^+$ . The particles convect through the magnetosphere according to the Lorentz force equation,

$$m_n \frac{d\mathbf{v}_n}{dt} = q_n (\mathbf{E}(\mathbf{r}, t) + \mathbf{v}_n \times \mathbf{B}(\mathbf{r}, t)) \quad (5.1)$$

with the electric and magnetic fields obtained from 3D multifluid simulations as described in Chapter 3. Time-dependent field information from the multifluid model is saved at 15 minute intervals and a linear interpolation scheme is used to interpolate the electric and magnetic field information between grid points and time steps (see section 3.2). Using this recorded field information with the particle tracking code is not a self-consistent treatment, as the particles do not influence the evolution of the electric and magnetic fields; however, it allows for studies of the response of different ionospheric outflow regions to identical field conditions. In this way, we are able to compare the response of different ion species from several injection locations (sources) over the storm event in question and determine the efficiency of various outflow regions for the same set of input field conditions. The use of the multifluid simulations in concert with the single particle tracking scheme and the benefits of such a system are described at length in Chapter 4. Similar to results shown in Chapter 4, Figure 5.1 depicts the temporal evolution of the magnetic field as well as the evolution of outflowing ionospheric ions within the 3D simulation. In the results presented in subsequent figures, particles are either shown in a polar plot, with particles mapped back to the ionosphere, or from an equatorial perspective.

The 3D simulations are solved on a Cartesian grid using GSM coordinates, with varying grid resolution. The highest resolution of  $\sim 0.3 R_E$  extends from  $17.7 R_E$  to  $-35.4 R_E$  in  $x$ ,  $\pm 11.8 R_E$  in  $y$ , and  $\pm 8.9 R_E$  in  $z$ . The resolution then increases with distance from the Earth to  $2.4 R_E$ . The full simulation region extends from  $47 R_E$  to  $-377 R_E$  in  $x$ ,  $\pm 94 R_E$  in  $y$ , and  $\pm 70 R_E$  in  $z$ . The inner boundary of the simulations is set at  $2.7 R_E$ . In the multifluid

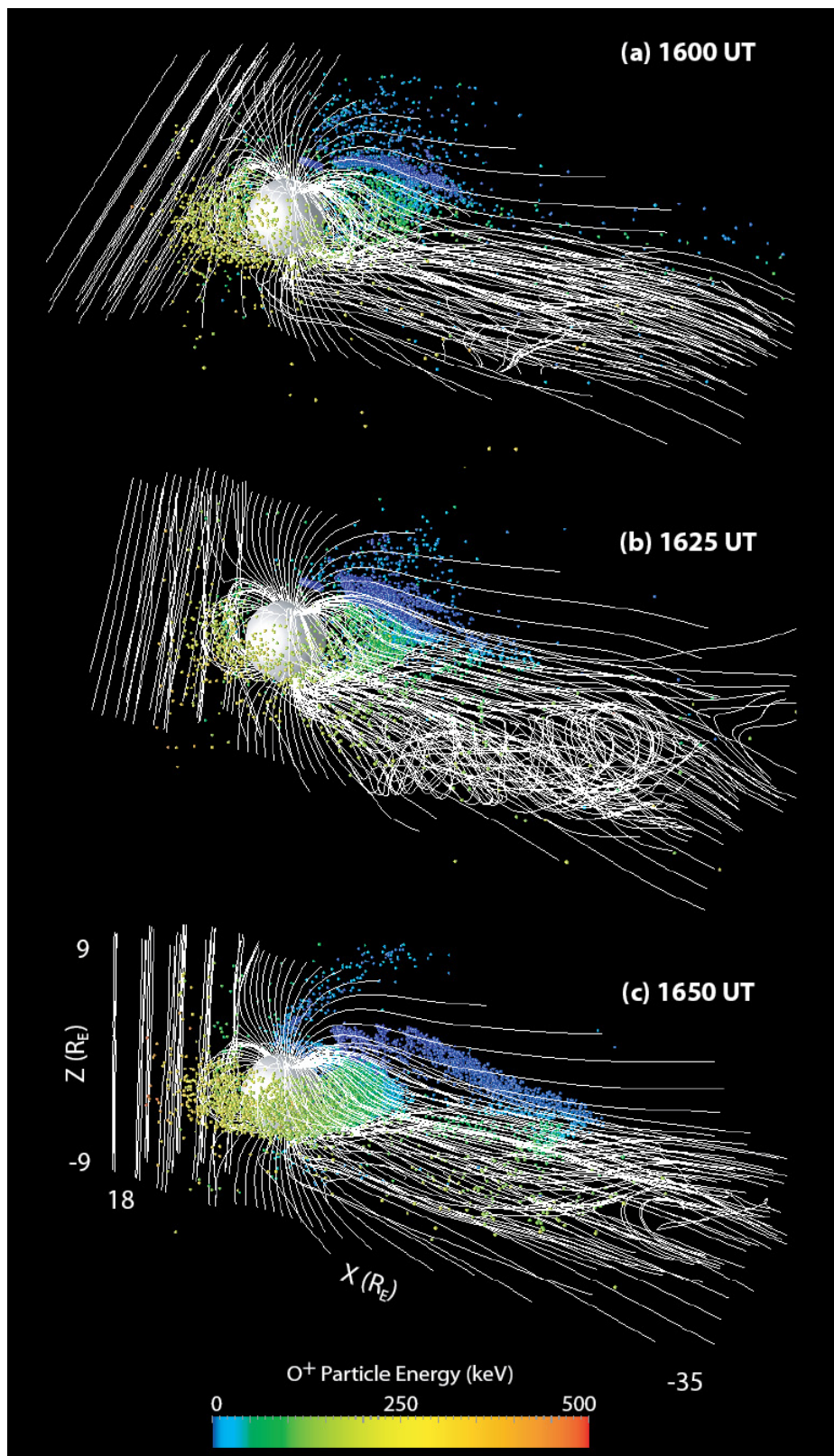


**Figure 5.1** Evolution of the magnetic field and outflowing oxygen ions within the 3D simulation domain for the main phase of the 10 March 1998 storm.

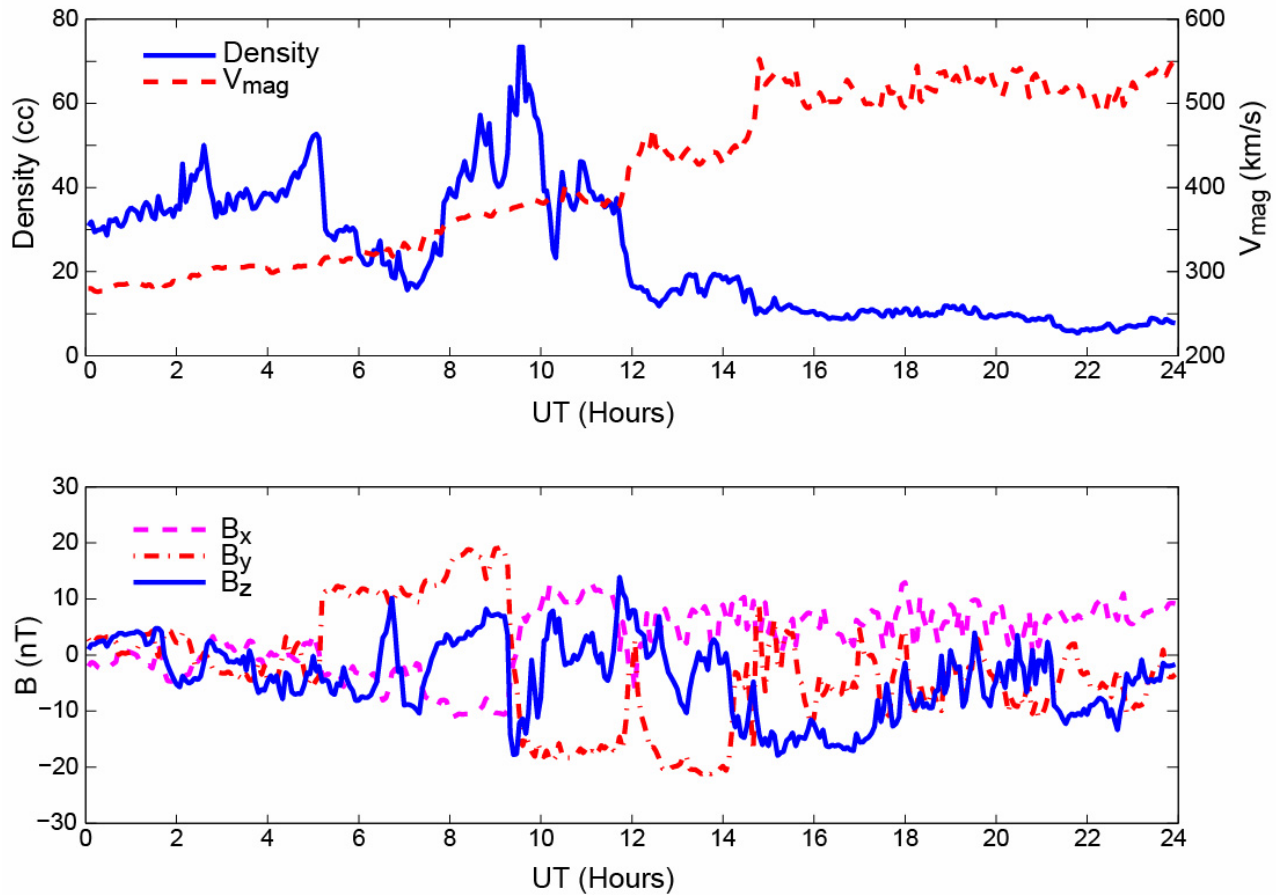


**Figure 5.2** Solar wind conditions on 10 March 1998 as measured by the ACE spacecraft at L1. (top) Solar wind density (solid blue line) and speed (dashed red line). (bottom) Components of the IMF.

simulations the  $\text{H}^+$  ionospheric density at the inner boundary is held fixed at  $400 \text{ cm}^{-3}$ , while the concentration of  $\text{O}^+$  at the inner boundary varies according to the magnitude of the aurora currents with a minimum concentration of 5% during low activity periods and a concentration equal to  $\text{H}^+$  during active periods. These boundary conditions lead to outflow rates which are consistent with those reported by *Yau and André* [1997] of  $10^{25}$ – $10^{26}$  ions/s.

We model the 10 March 1998 storm event using the input parameters shown in Figure 5.2. For this event there were two strong rotations of IMF  $B_z$  with an extended period of intensely southward ( $< -10 \text{ nT}$ ) IMF  $B_z$  between 1400 and 1800 UT; there were also large IMF  $B_x$  and  $B_y$  components. During periods of large  $|B_x|$  (between 0724 and 1148 UT), a value of  $B_x = 0 \text{ nT}$  was used in order to keep the multifluid model from going unstable.

These periods are before the main phase of the storm and this approximation is not expected to affect the results. For a more detailed discussion of the 10 March 1998 storm event, see *Jordanova et al.* [2001].

In these simulations particles are continuously injected from high-latitude regions with initial energies of 50 eV for  $H^+$  and 1 keV for  $O^+$ . The injection rate was 10,000 particles to 100,000 particles injected at varying time intervals ranging from 10 to 15 minutes. The total number of particles tracked at any given time was limited to 2,000,000. Such a continuous injection scheme allows for full temporal coverage of the magnetosphere, which is necessary when comparing the efficiency and relative contribution for each of the ionospheric outflow regions studied.

Sixteen separate ionospheric outflow regions were considered. Outflow regions were grouped in 6 hour overlapping wedges (for determining the most efficient sectors at generating RC particles) and in 3 hour non-overlapping wedges (for the relative contribution plots and calculations). Both high- and low-latitude source regions were considered with high-latitude particles initialized between  $70^\circ$  and  $80^\circ$  invariant latitude and with low-latitude particles initialized between  $60^\circ$  and  $70^\circ$  invariant latitude. All particles were initialized in a wedge shaped region in local time from the specified outflow region at an altitude of  $3.5 R_E$ . Such complete ionospheric coverage, including high- and low-latitude source regions from all MLTs, allows for the determination of (1) the most efficient outflow location for getting ionospheric particles to the ring current as well as (2) the regions that experience the greatest levels of particle energization.

### **5.3 Energization and Trapping of Ring Current Ions**

Values for the  $B_z$  component of the IMF are plotted above the  $Dst$  index for the corresponding time interval in Figure 5.3. The values for the IMF  $B_z$  were obtained from Advanced Composition Explorer (ACE) data and have been propagated to the bow shock; in this way, the  $Dst$  index can be compared to the corresponding IMF  $B_z$  values. For the

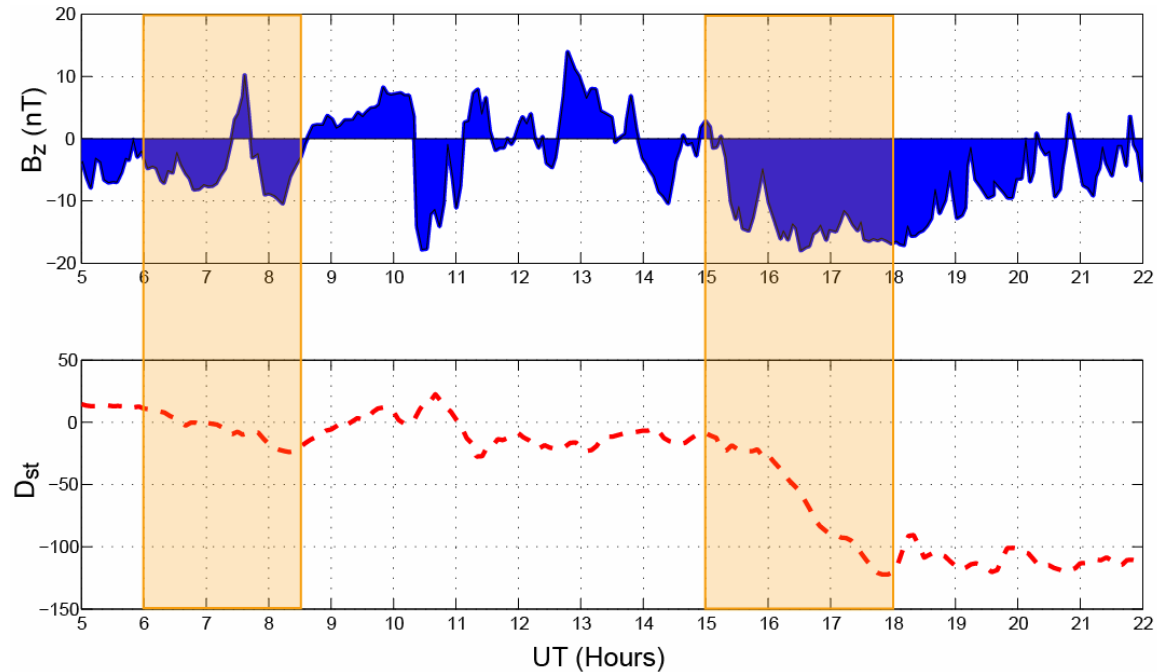


**Figure 5.3** Parameters used to monitor conditions for the 10 March 1998 storm. (top) Solar wind  $B_z$  component obtained from ACE data and propagated to the bow shock. (bottom)  $Dst$  index for the corresponding time interval. The two decreases in  $Dst$  examined in this chapter have been highlighted in orange.

10 March 1998 storm, three decreases in  $Dst$  were observed, with the storm reaching a minimum value of -130 nT around 1800 UT (Figure 5.3). This chapter focuses on two of these decreases: the first is the small decrease in  $Dst$  that occurs between 0600 and 0830 UT, and the second is the much larger drop in  $Dst$ , which represents the main phase of the storm and occurs between 1500 and 1800 UT.

The results for the first, smaller dip in  $Dst$  are shown in Figure 5.4 with ring current ions mapped along terrestrial field lines to the polar region. The left-hand side of the image shows hydrogen ions initialized in the midnight sector between 21 and 03 MLT from  $70^\circ$  to  $80^\circ$  latitude (high latitudes), and the right-hand side shows results for oxygen ions initialized from a slightly dawnward location, 00 – 06 MLT, and from  $70^\circ$  to  $80^\circ$  latitude. Simulations were also run for ions from other ionospheric sectors in order to determine the most geo-optimal outflow location. In this determination of the geo-optimal launch location, we are not taking into account the relative outflow rates for the different

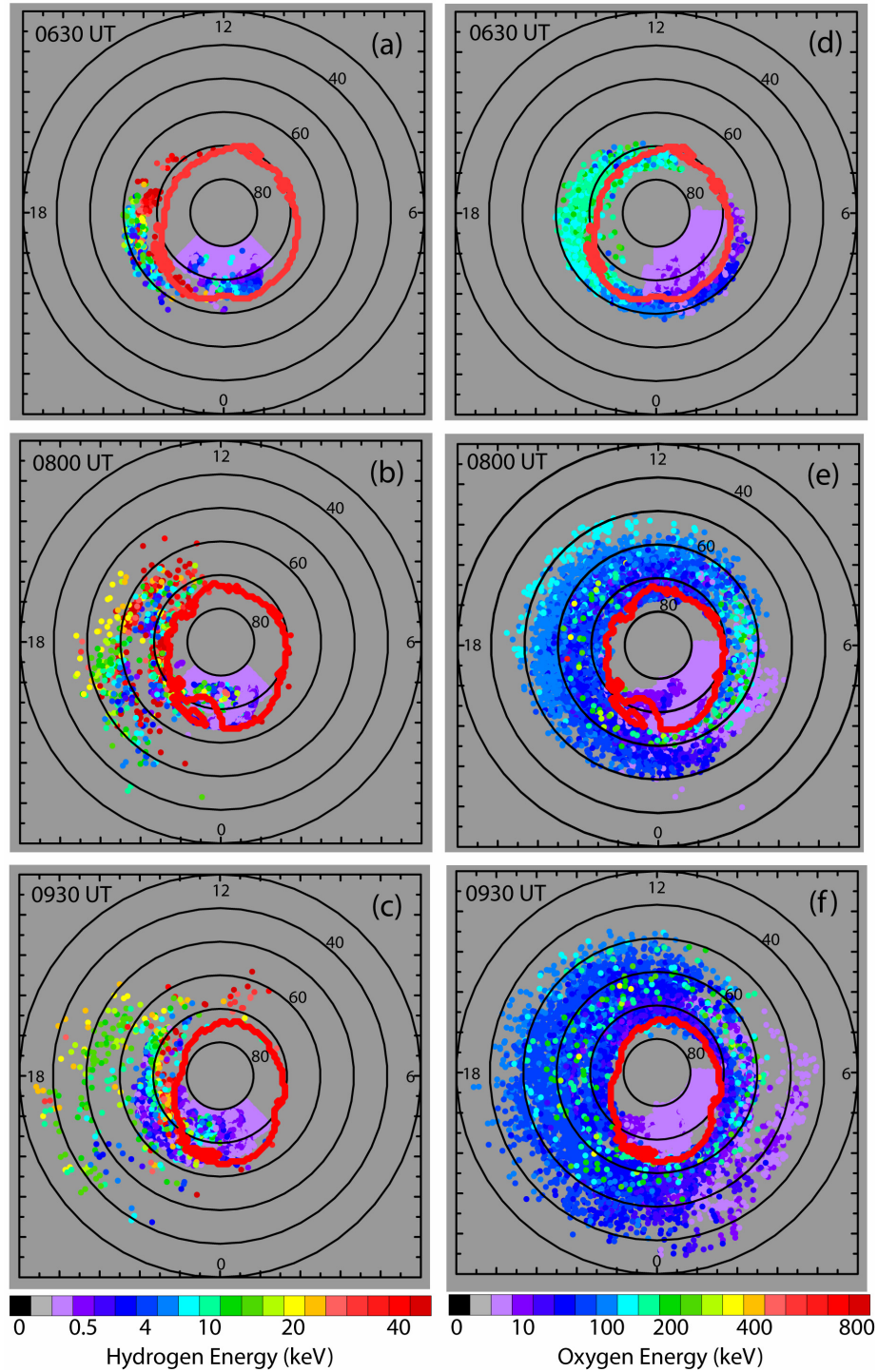


**Figure 5.4** Foot point mapping of ring current ions mapped back to the polar cap. These results are for the smaller decrease in  $Dst$  observed between 0600 and 0830 UT. The left-hand column shows results for  $H^+$  and the right-hand column shows results for  $O^+$ . The lavender wedge shows the locations from which the ions were initialized, and the solid red line depicts the location of the separatrix as determined by the multifluid simulations. The particles are color coded according to energy. The energy scale for  $H^+$  and  $O^+$  is different, whereas the velocity scale is the same for both ions.

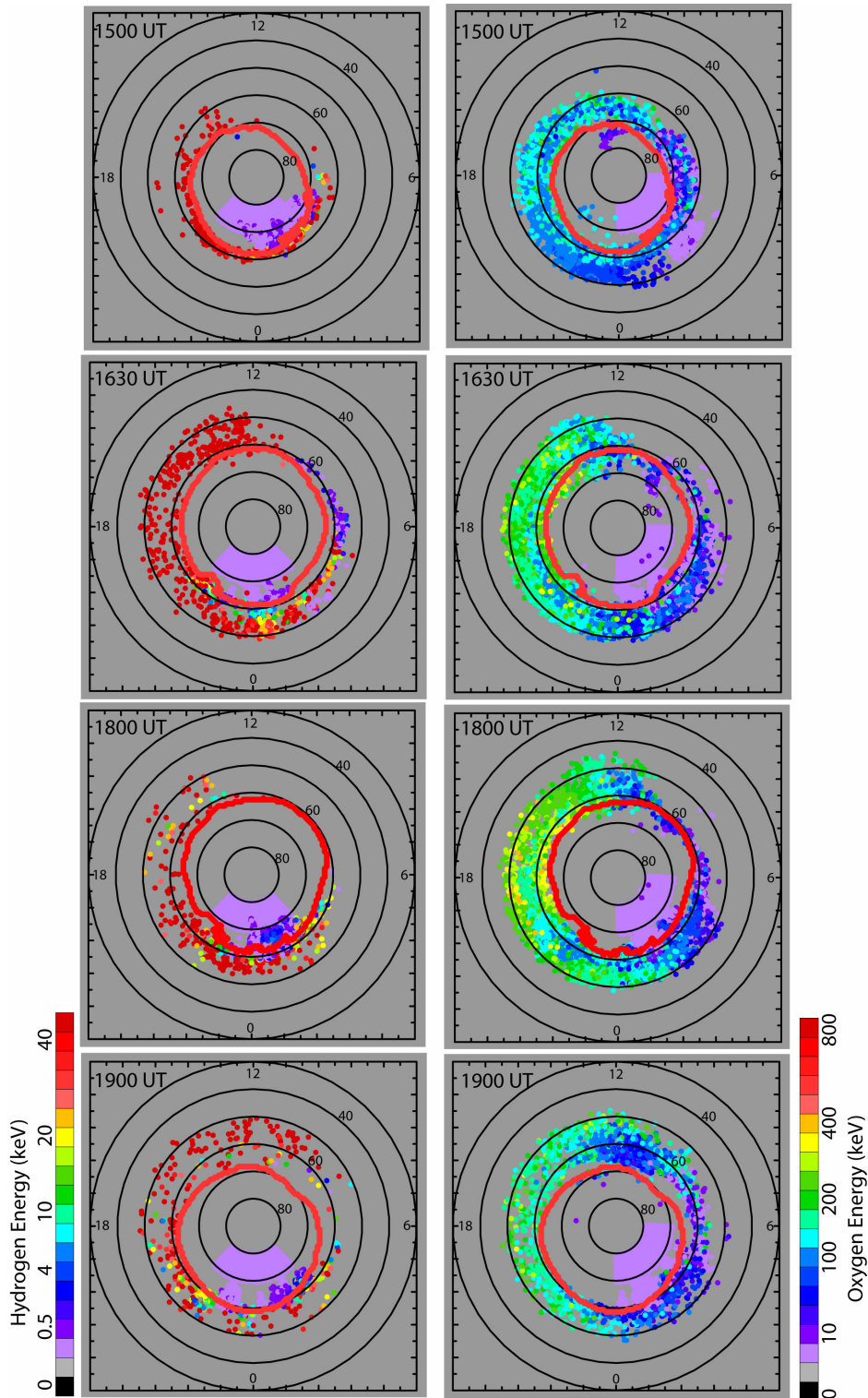


**Figure 5.5** Results for hydrogen and oxygen ions for the main phase of the storm, which occurs between 1500 and 1800 UT when the solar wind is strongly southward with  $B_z \approx -15$  nT. Injections of energetic particles are observed for  $O^+$  at 1630 and 1800 UT. Ions begin to form a symmetric ring current at 1900 UT.

ionospheric outflow regions, instead we inject equivalent numbers of  $H^+$  and  $O^+$  ions from the ionosphere in order to determine the most effective locations for getting energetic particles into the ring current, and here efficiency is determined by the factor of particles that make it into the ring current region. In the next section (5.4), the outflow rates will be taken into account in order to determine the relative density and energy contribution from 16 different ionospheric outflow regions to the total ring current.

For periods of low activity, the most geo-optimal outflow location for generating ring current ions is the predawn high-latitude sector (see section 5.4). For  $O^+$ , this outflow region was significantly more efficient at getting ionospheric particles into the ring current, producing  $\sim 100\%$  more ring current ions than the midnight and dawn sectors, the next two most efficient outflow regions. For  $H^+$ , the geo-optimal outflow location is not as clearly defined and varies over the duration of the simulation with outflow sectors from 21 to 06 MLT and from both high and low latitudes all efficient at generating ring current particles at some point during the simulation. The  $H^+$  outflow region shown in Figure 5.4 was chosen to show an additional initialization location for outflowing ions contributing to the ring current.

During the initial period of southward IMF (0500 to 0725 UT), injections into the inner magnetosphere of energetic particles on the dusk side are observed for both  $H^+$  and  $O^+$  (Figure 5.4a and Figure 5.4d). These injections are similar to those observed in the previous chapter which addressed the energization and inward transport of ionospheric ions during substorm conditions (sections 4.3-4.5), where discrete injections of energetic particles were observed in association with small-scale structures ( $\sim 1 R_E$ ) in the current sheet, such as tail kinking and earthward moving flux ropes. The energetic particles in Figure 5.4 are observed to convect westward around the earth to noon where the particles encounter the dayside reconnection regions and are lost over the polar cap on open trajectories. An injection of  $O^+$  ions takes  $\sim 10$  minutes to travel from the location of particle initialization at an altitude of  $3.5 R_E$  to its destination in the ring current.

After a brief northward turning at 0724 UT and again during an extended period of northward IMF beginning at 0839 UT, the energetic particles are observed to move closer to Earth (lower latitudes in the foot point mapping plots) and to convect past noon. Northward turnings of the IMF seal off the dayside loss region, trapping radiation belt ions on closed trajectories. This is easily seen for  $O^+$  where a symmetric ring current forms by 0800 UT (Figure 5.4e and Figure 5.4f). During periods of northward IMF, new injections of energetic particles into the ring current are not observed.

Both  $H^+$  and  $O^+$  demonstrate the same response to changes in the  $B_z$  component of the IMF; however, the energies and densities of the hydrogen ions are much lower than those of the oxygen ions launched during the same times and from the same locations. While the oxygen ions at 0630 UT reached energies of  $\sim 200$  keV, the  $H^+$  ions are only energized to around 50 keV. The observed energies for this first initial decrease in  $Dst$  agree with results for an idealized substorm presented in Chapter 4. Particle injections are observed with a southward IMF and then northerly turnings of the IMF trap the particles.

The solid red line in Figure 5.4 and Figure 5.5 shows the location of the separatrix, the boundary between the region of open field lines and closed field lines. During the first decrease in  $Dst$  the separatrix is at high latitudes, around  $70^\circ$  on the dayside and  $65^\circ$  on the night side (Figure 5.4). During this time the most geo-optimal regions for getting ionospheric particles into the ring current are the midnight and predawn sectors at high latitudes. The midmorning and noon sectors, while known to contribute significantly to outflow, are not very efficient at producing particles that ultimately enter the ring current. Likewise, between 0600 and 0930 UT lower auroral latitudes are not geo-optimal locations for producing ring current particles even though these regions are known to have significant outflow rates [Yau and André, 1997].

Figure 5.5 shows results plotted in the same style as Figure 5.4, but for the main phase of the storm between 1500 and 1800 UT when the largest decrease in  $Dst$  is observed. During this part of the storm, the outflowing ions experience higher levels of energization, with  $H^+$  particles energized to  $\sim 50$  keV and  $O^+$  particles energized to  $\sim 350$  keV. After the IMF

turns southward at 1515 UT, energetic oxygen ions are observed on the dusk side (Figure 5.5f and Figure 5.5g) with energies up to 400 keV, much larger than those observed associated with the earlier small decrease in  $Dst$ . As with the previous time period, during this period of southward IMF, the energetic particles convect westward to the dayside reconnection region where they are lost over the polar cap, forming only a partial ring current. However, by 1900 UT, the energetic oxygen ions have begun to convect past noon and a symmetric ring current is beginning to form (Figure 5.5h). At this time the IMF is still strongly southward ( $B_z \approx -10$  nT), but not as intensely southward as between 1600 and 1800 UT, and a symmetric ring current is forming even in this southward field. Thus, during the main phase of the storm, particle trapping occurs even in a strongly southward  $B_z$  field due to the reduction in the southward component.

During the main phase of the storm, the polar cap expands to lower latitudes and extends further into the noon and midmorning sectors (Figure 5.5). At this time, ring current particles are seen to originate from all MLT source regions as well as from auroral latitudes. With the expanded polar cap, outflowing ions from lower latitudes are able to convect downtail, become energized, and be injected into the ring current. While more ionospheric outflow sectors now contribute particles to the ring current, the average energies achieved by the ions depend on the outflow regions from which the particles originate.

On the left-hand side of Figure 5.5, hydrogen ions are shown initialized in the midnight sector at high latitudes. The high-latitude source region does not significantly contribute to the ring current during this time; however, during this large decrease in  $Dst$  the lower-latitude source regions contribute more to the ring current than the higher latitudes. This is especially true between 1650 and 1800 UT when the polar cap has expanded and moved to lower latitudes. For  $O^+$ , the high latitudes are a more efficient source of energetic particles, while for  $H^+$ , lower latitudes contribute more to the ring current population. The most energetic particles originate from the predawn, dawn and midmorning sectors for  $O^+$ , while for  $H^+$  the most energetic particles are the midnight and predawn sectors.

#### **5.4 Relative Contribution of Ionospheric Source Regions**

In addition to considering the geo-optimal location from which to launch ionospheric particles, the relative contribution from various ionospheric outflow regions to the total ring current energy density was also compared. By taking into account the ionospheric outflow rates, the ionospheric regions that are the most significant contributors to the ring current energy and particle density can be determined. Comparing these results over the simulation interval, a graphical representation of the way in which the contribution from each sector varies over the storm development can be generated.

Outflow rates for each sector were determined using results from the multifluid model as described by *Winglee et al.* [2002, 2008]. The multifluid model includes dynamic boundary conditions that allow for more ionospheric outflow as Region 1 and 2 currents increase. The density of the heavy ions at the inner boundary scales with the derived current through the ionosphere, and represents an increase in the scale height of the heavy ions that occurs within increased magnetospheric activity. The bulk velocity and thermal velocity of the ions at the inner boundary are held constant. Up-flowing ionospheric flux values were computed for each of the 16 ionospheric outflow sectors at 1.8 minute time intervals; outflow rates varied with sector location and with time during the storm development. The outflow rates used in the single-particle tracking were scaled by the outflow rates obtained from the multifluid simulations in computing the relative contribution of ionospheric source regions to the ring current.

Results are shown in Figure 5.6 through Figure 5.9. In all four of these images, the right-hand column shows a north pole view of the location of ring current particles within  $1.5 R_E$  of the equatorial plane during the time listed in the center column. Particles not within  $1.5 R_E$  of the equatorial plane are not shown. Noon is at the top of the images and the red circles represent  $L$  shells of 4, 6, and 8, respectively. The locations from which the ring current particles originated within the ionosphere are shown adjacent to the north pole view (on the left-hand side of these images) with the magenta circles denoting invariant latitudes of  $60^\circ$ ,  $70^\circ$ , and  $80^\circ$ . The white lines separate the eight different MLT sectors

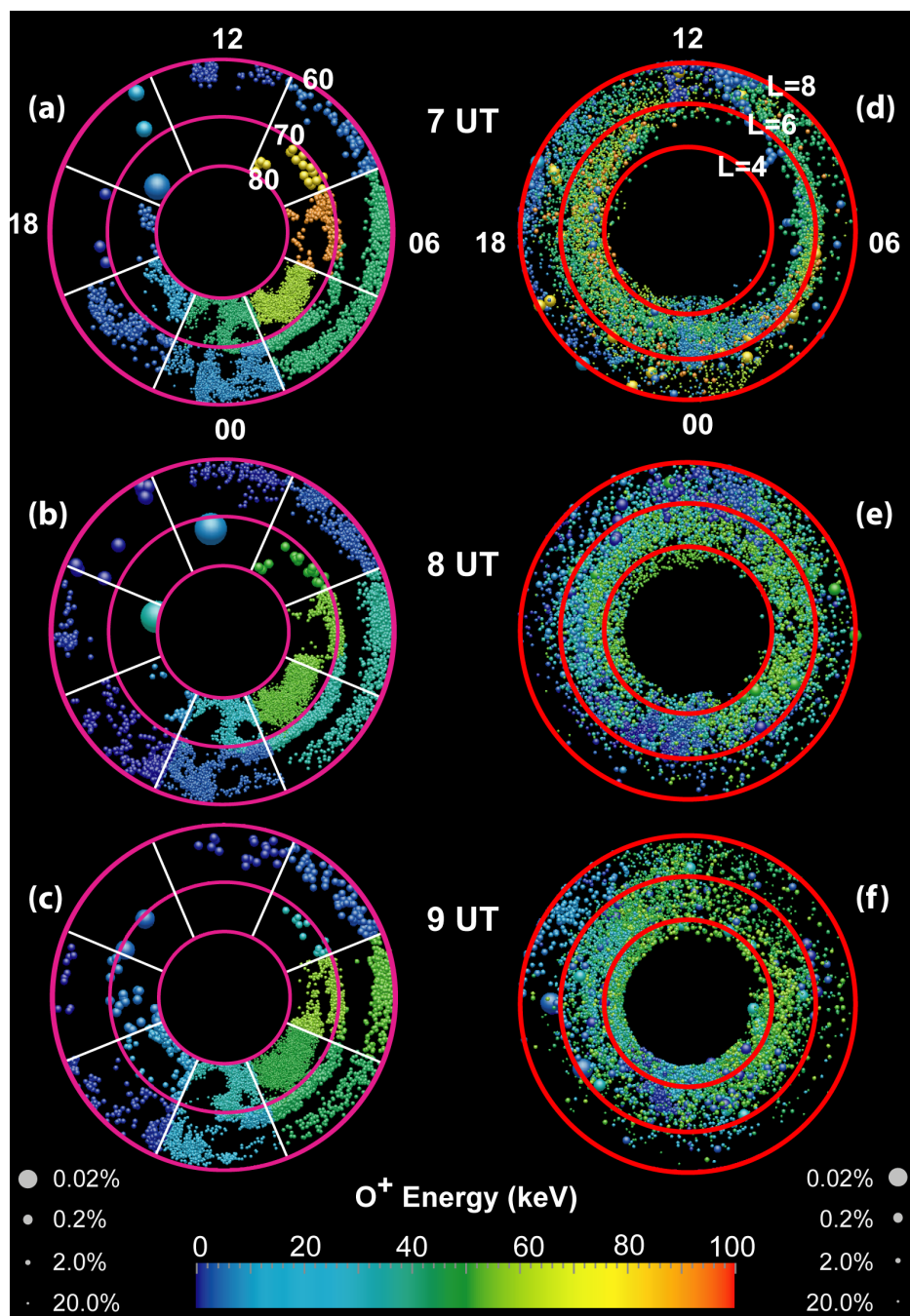


**Figure 5.6** Initial outflow region (column 1) and current location within the ring current (column 2) for oxygen ions during the smaller decrease in  $Dst$ . The relative contribution from each outflow location to the total ring current density is inversely related to the size of the particles, and particles are color coded according to the average energy of the ions outflowing from that sector. Magenta circles denote invariant latitudes of  $60^\circ$ ,  $70^\circ$ , and  $80^\circ$ , and the white lines separate outflow regions into eight sectors each spanning 3 h of MLT. Equivalent numbers of particles were launched from each sector. (a-c) Initial outflow location of particles that end up in the ring current. (d-f) North pole view of the location of ring current particles within  $1.5 R_E$  of the equatorial plane during the time listed in the center column. Noon is at the top of all the images and the red circles represent  $L$  shells of 4, 6, and 8, respectively.

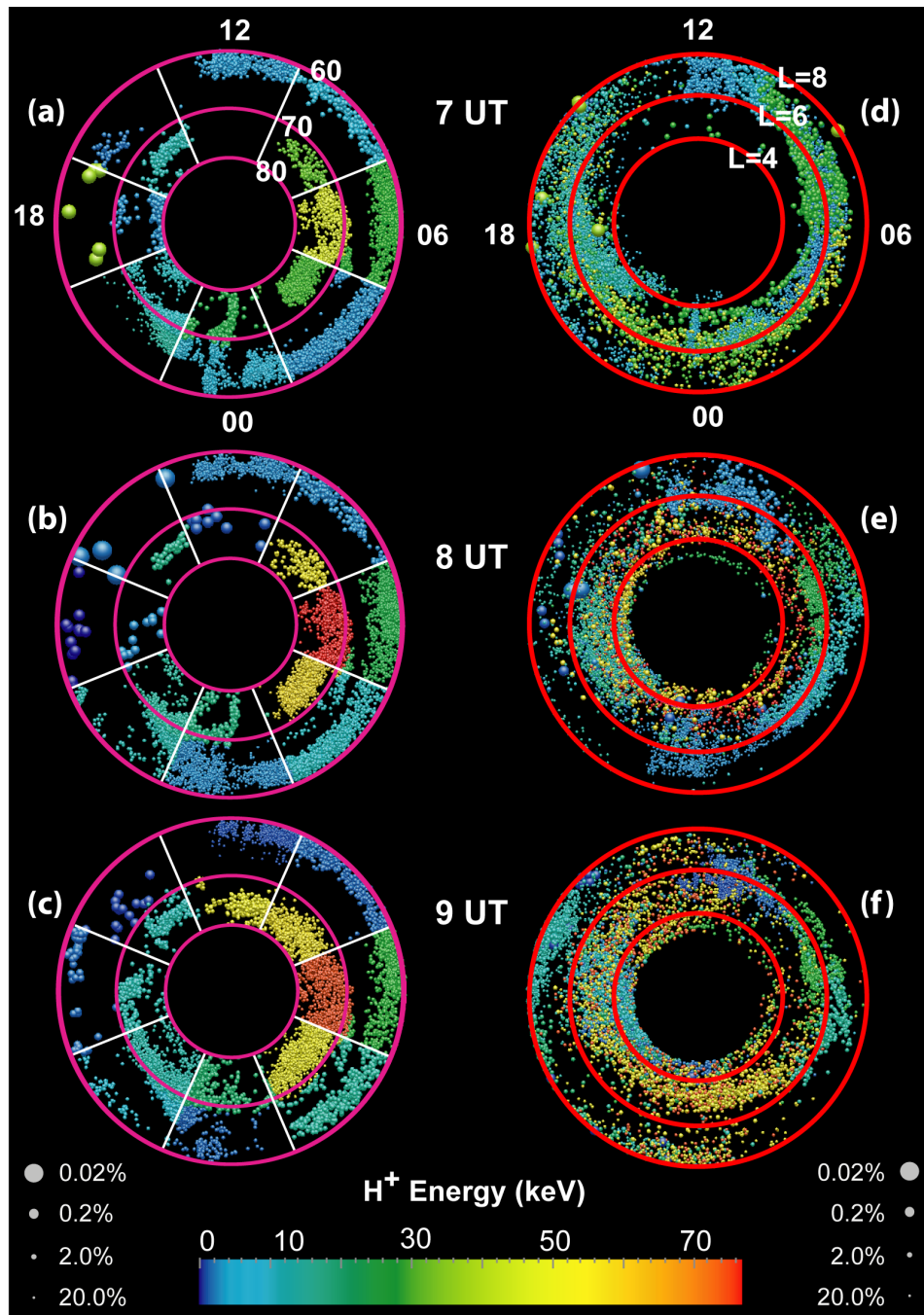


**Figure 5.7** Same format as Figure 5.6, this time showing the relative contribution plots (column 1) and particle locations within the ring current (column 2) for hydrogen ions.

considered (moving in a clockwise fashion): midnight, predawn, dawn, midmorning, noon, afternoon, dusk, and premidnight. Particles were launched either from high latitudes, between 70° and 80° invariant latitude, or low latitudes, between 60° and 70°. The relative contribution plots on the left-hand side of Figure 5.6 through Figure 5.9 show which

sectors are contributing the majority of the particles to the ring current at the given times. The particles are color coded according to the average energy attained by ions outflowing from that region at the given time. In each plot 10,000 particles are shown and the size of the particles is inversely related to the percent that each sector contributes to the total ring current density. Regions with numerous small particles are the most significant contributors to the total ring current density, and regions with only a few large particles do not contribute much to the total density of the ring current at the depicted time. Outflow regions which contain no particles are regions from which few, if any, ions made it into (or remained within) the ring current during the simulation for that time. The energy scale is listed at the bottom of the image and varies according to the highest average energy attained during the time interval shown.

For the decrease in  $Dst$  between 0600 and 0830 UT, most of the  $O^+$  ions come from the predawn sector (Figure 5.6a – Figure 5.6c). Between 0700 and 0900 UT, the predawn high-latitude sector contributes  $> 30\%$  of the  $O^+$  to the ring current (increasing from 31% at 0700 UT to 41% at 0900 UT). No other sector contributes as significantly to the total ring current  $O^+$  density. The noon high latitude sector and afternoon sectors are insignificant contributors of  $O^+$  to the ring current during this phase of the storm development.

The most energetic  $O^+$  in the ring current during this time originates from the high-latitude regions near dawn. Average energies of between 5 and 50 keV are observed for most outflow regions with the most energetic ions originating from the dawn high-latitude sector. These particles have an average energy of 90 keV at 0700 UT. This is slightly lower than the peak average energy of 102 keV attained by ions outflowing from the dawn high latitude sector between 0643 and 0650 UT. At later times, the predawn, dawn, and midmorning high sectors all contribute particles with average energies of  $\sim 60$  keV. The energies in Figure 5.6 through Figure 5.9 represent the average energies from each outflow region and as such, these values are smaller than those shown in Figure 5.4 and Figure 5.5 where each particle is plotted individually. Maximum energies observed during this first decrease in  $Dst$  can be as large as 690 keV for  $O^+$  (0744UT) but are typically  $\sim 400$  keV

during this time period. The large maximum energy at 0744 UT is from the predawn low-latitude sector and is associated with a large earthward moving flux rope observed to form in the tail at 0735 UT and to reach the inner magnetosphere at 0745 UT. Before 0820 UT, the midnight low-latitude region shows the greatest contribution to the ring current, but between 0820 and 0950 UT the midmorning high-latitude sector becomes the region of greatest contribution; however, despite having a large outflow rate, this region is not efficient at generating ring current particles.

Similar to  $O^+$ , the most energetic hydrogen ions originate from the dawn high sector during this initial decrease in  $Dst$  (Figure 5.7). Average energies are between 5 and 30 keV and the most energetic outflowing ions attained an average energy of  $\sim 75$  keV during the time interval from 0700 to 0900 UT. However, a peak in the average energy for  $H^+$  is observed earlier in the simulation at 0631 UT; at this time, the average energy from the dawn high-latitude sector reaches 126 keV and the average energy from the predawn high-latitude sector reaches an average energy of 117 keV. The difference in the time of the peak level of energization could be due to differences between  $H^+$  and  $O^+$  energization mechanisms or to previous mass loading of the magnetotail by hydrogen ions. The peak in the average energy of outflowing  $H^+$  from the dawn and predawn high-latitude regions occurs  $\sim 15$  minutes before a corresponding peak is seen in average energy of outflowing  $O^+$ . This delay between  $H^+$  and  $O^+$  energization has previously been reported by *Harnett et al.* [2008], who demonstrated that for the 29 October 2003 Halloween storm, a 20 minute delay occurred between the  $H^+$  and  $O^+$  energization at the beginning of the event. Later during the storm development, between 0700 and 0900 UT, the average energies achieved by each of the outflow regions remained fairly constant, with maximum energies of  $\sim 300$  keV. The midmorning, dawn, and predawn sectors at high latitudes all reached  $\sim 50$  keV for the average energy of the ring current ions between 0800 and 0900 UT. At these times, the ring current ions begin to form a symmetric ring current as shown by the red-colored particles in Figure 5.7e and Figure 5.7f.

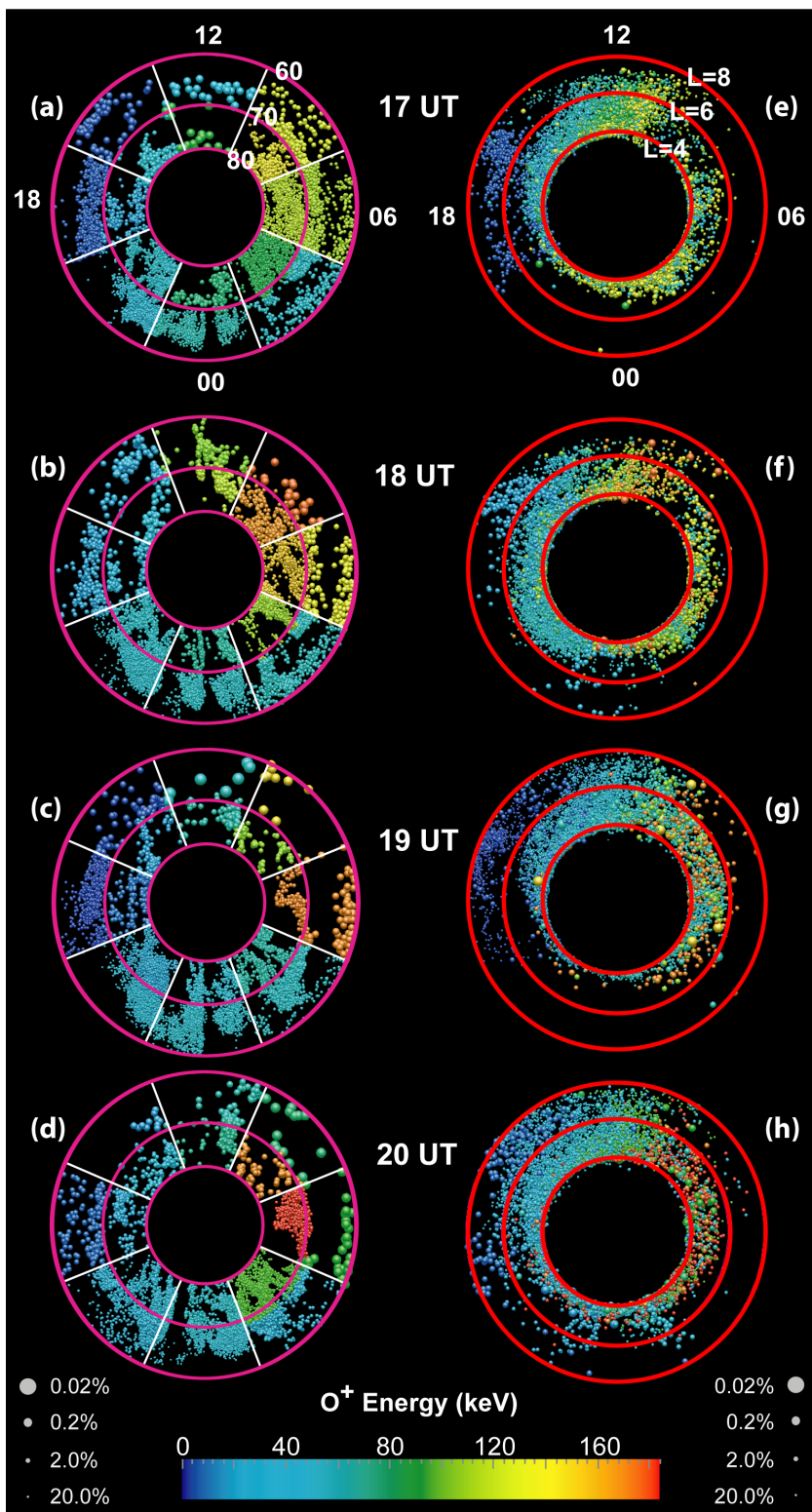


**Figure 5.8** Same format as Figure 5.6, but this time for the main phase of the storm. The average energies attained by the oxygen ions are larger than those in Figure 5.6. (a-d) More uniform contribution from all 16 ionospheric outflow regions to the total ring current density.

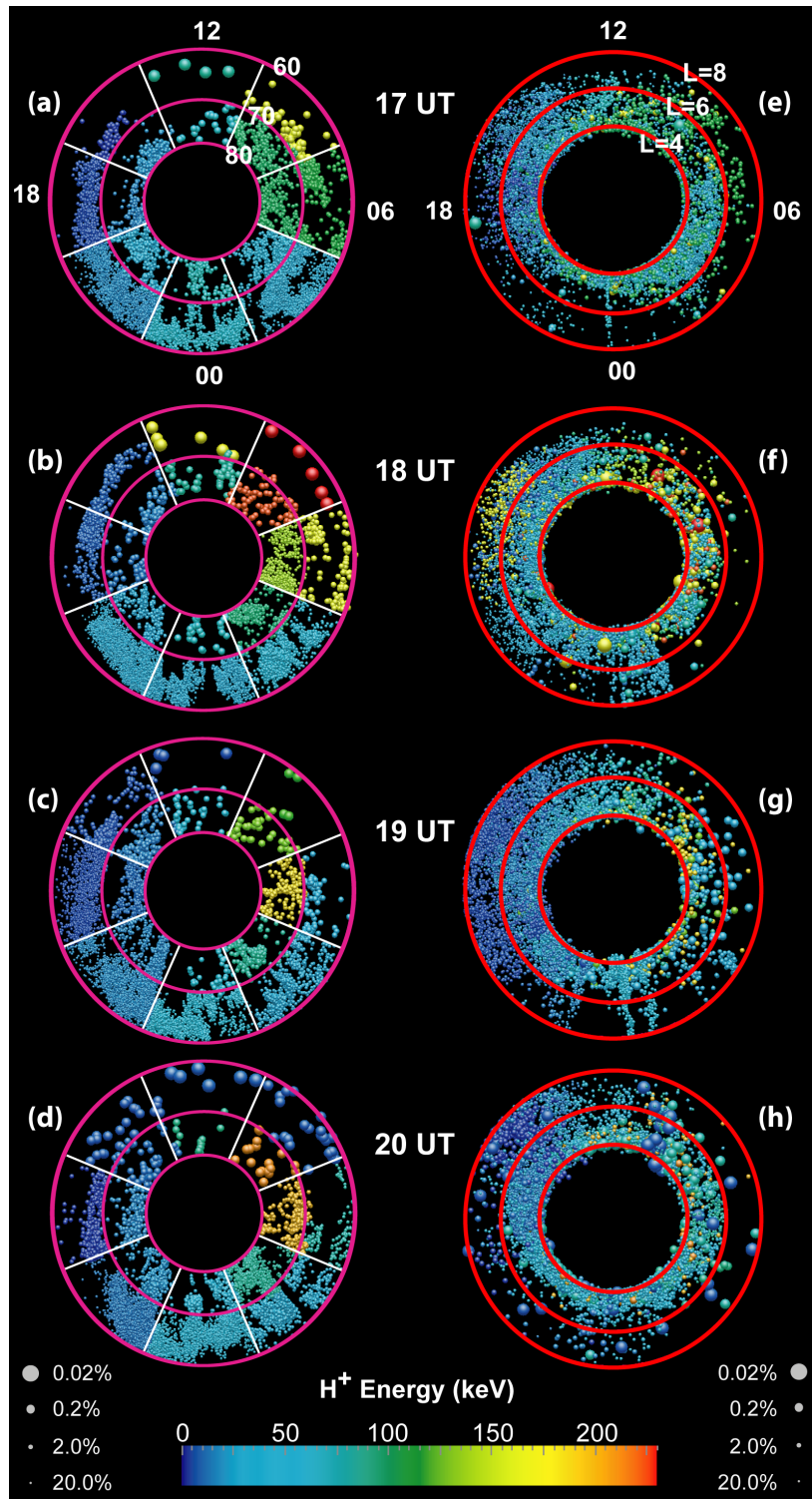


**Figure 5.9** Same format as Figure 5.7, now showing results for hydrogen ions during the main phase of the storm. Compared with Figure 5.7, higher average energies are observed and an increased contribution to the total ring current density is seen from the dusk sided at both high and low latitudes.

Unlike for  $O^+$  where the predawn high sector was by far the greatest contributor to the ring current density, for  $H^+$ , eight of the sectors each contribute  $<5\%$  of the RC particle density and the other 8 sectors each contribute between 5% and 20%. The region that dominates the density contribution to the RC extends from roughly 21 to 08 MLT and includes outflow from both high and low latitudes. The ionospheric outflow rates during this time show significant outflow from the region extending from 06 to 12 MLT at high latitudes and from 00 to 06 MLT at low latitudes. Thus, there can be significant ionospheric outflow to feed plasma into these regions and contribute to the RC. The  $H^+$  outflow rates are  $\sim 10 \times$  larger than the  $O^+$  outflow rates during this pre-main phase decrease in  $Dst$ , and thus,  $H^+$  is contributing more overall particles to the ring current during this time.

Figure 5.8 shows relative contribution plots for oxygen ions during the main phase of the 10 March 1998 storm. Several differences are observed between these plots and those in Figure 5.6 for the smaller decrease in  $Dst$ . First, all MLTs and all latitudes are contributing to the RC. Each of the 16 outflow locations contributes at least 0.1% of the particles in the simulation. No sector contributes  $>30\%$  of the total ring current particle density, and more than half the sectors contribute between 1% and 10% of the particles to the ring current, providing a fairly uniformly distributed source for ring current particles. This corresponds to a time when the polar cap region has expanded, moving down to lower latitudes (see Figure 5.5), and thus, particles outflowing from regions between  $\sim 12$  and 18 MLT contribute more significantly to the total ring current density.

Comparing Figure 5.6 and Figure 5.8, one of the most pronounced features is the higher degree of energization attained by the oxygen ions between 1700 and 2000 UT (note the different energy scales). The most energetic particles still originate from the dawn side, but their outflow location shifts. At 1700 UT, particles with average energies of 130 keV are seen originating between 07 and 09 MLT, whereas at 2000 UT, particles with average energies of 170 keV are seen originating in a more concentrated region around 06 MLT at latitudes between  $70^\circ$  and  $80^\circ$ . The increased density of particles originating from the dawn and midmorning sectors at 1700 UT corresponds to a time when the extent of the separatrix has expanded and a stronger cross polar cap potential is observed, associated

with more flux into the magnetosphere, resulting in stronger electric and magnetic fields. By 2000 UT, the separatrix has contracted and the midmorning and dawn low latitude sectors are no longer experiencing increased outflow: this is illustrated in Figure 5.8c and Figure 5.8d by a decrease in the particle number density from the midmorning and dawn low latitude outflow regions. During the main phase of the storm, all particles achieve a higher degree of energization, which is expected in a strongly southward IMF field in which an active magnetosphere results in increased particle accelerations and injections. The plots at 1700 and 1800 UT are during the most intense southward IMF of the storm with  $B_z$  continuously  $<-10$  nT. By 2000 UT, the IMF is still southward, but not as strongly southward as before. The ring current particles are more evenly distributed around the earth (Figure 5.8h). The most energetic particles at this time originate from the dawn high-latitude sector and these red particles are seen at all MLTs in Figure 5.8h.

Significant differences are observed for  $H^+$  ions between the first decrease in  $Dst$  (0600 to 0830 UT) and during the main phase of the 10 March 1998 storm. Results for the main phase of the storm (Figure 5.9) show that sectors between  $\sim 12$  and 21 MLT now contribute more significantly to the ring current, similar to what was observed for  $O^+$ . The midmorning and noon sectors at low latitudes are contributing less overall to the ring current density. During this time period (1700 – 2000 UT), the low latitude noon ionospheric outflow region consistently contributes  $<0.1\%$  to the total RC density. The dominant source of  $H^+$  to the ring current throughout this interval is from the premidnight low latitude outflow region between  $\sim 20$  and 23 MLT. This sector consistently contributes  $>25\%$  of the  $H^+$  particle density of the ring current and at 1800 UT this sector alone contributes 40% of the density. The particles originating from the low-latitude premidnight sector achieve average energies between 20 and 35 keV during the main phase of the storm. Regions experiencing the highest levels of energization have shifted slightly noonward, and the greatest levels of energization are seen for particles originating from the dawn, midmorning, and noon sectors.

The outflow rate from each sector as calculated by the multifluid model (see *Winglee et al.* [2002, 2008]) varied greatly over the duration of the storm. The majority of the  $H^+$  outflow

is from the midnight low and midmorning high-latitude sectors. This agrees with results by *Andersson et al.* [2004] who found the highest outflow rates in the morning side cusp and the midnight sectors. Comparing the two decreases in  $Dst$ , 0600 to 0830 UT and 1500 to 1900 UT, the midmorning sector at low latitudes experienced a significant increase in  $H^+$  outflow compared to other outflow sectors, more than doubling its  $H^+$  outflow rate, whereas other outflow rates remained fairly constant. This is particularly interesting since the midmorning sector at low latitudes was the only region from which the  $H^+$  contribution to the total RC density decreased. Even with an increased outflow rate, not many particles from the midmorning low-latitude sector are injected into the ring current region. However, the particles that do get injected into the ring current have some of the largest energies of all particles contributing to the ring current, with an average energy at 1800 UT of  $>200$  keV.

The most energetic  $H^+$  ions are observed in the ring current at 1800 UT, which corresponds to the minimum in  $Dst$  observed during the storm. This was not the case for  $O^+$  for which the largest particle energies were observed in the ring current at 2000 UT for particles originating from the dawn high sector with an average energy of  $\sim 170$  keV. Thus, during the main phase of the storm, higher energies are observed for hydrogen ions than for oxygen ions, and the time at which the greatest energies are observed and the ionospheric region from which these particles originate differs for the two species.

### **5.5 Energy Density Contribution from $H^+$ and $O^+$**

Results for the relative contribution from selected ionospheric sectors to total RC energy density are plotted over the duration of the simulation time interval for  $O^+$  and  $H^+$  in Figure 5.10 and Figure 5.11, respectively. This is the same information from Figure 5.6 through Figure 5.9 but plotted graphically as a function of time from 0600 to 2000 UT. To aid in readability, only five of the eight MLTs are shown, with low latitudes on the left-hand side and high latitudes on the right-hand side. For  $O^+$ , outflow from the predawn high-latitude sector is the dominant source of ring current particle density during the early

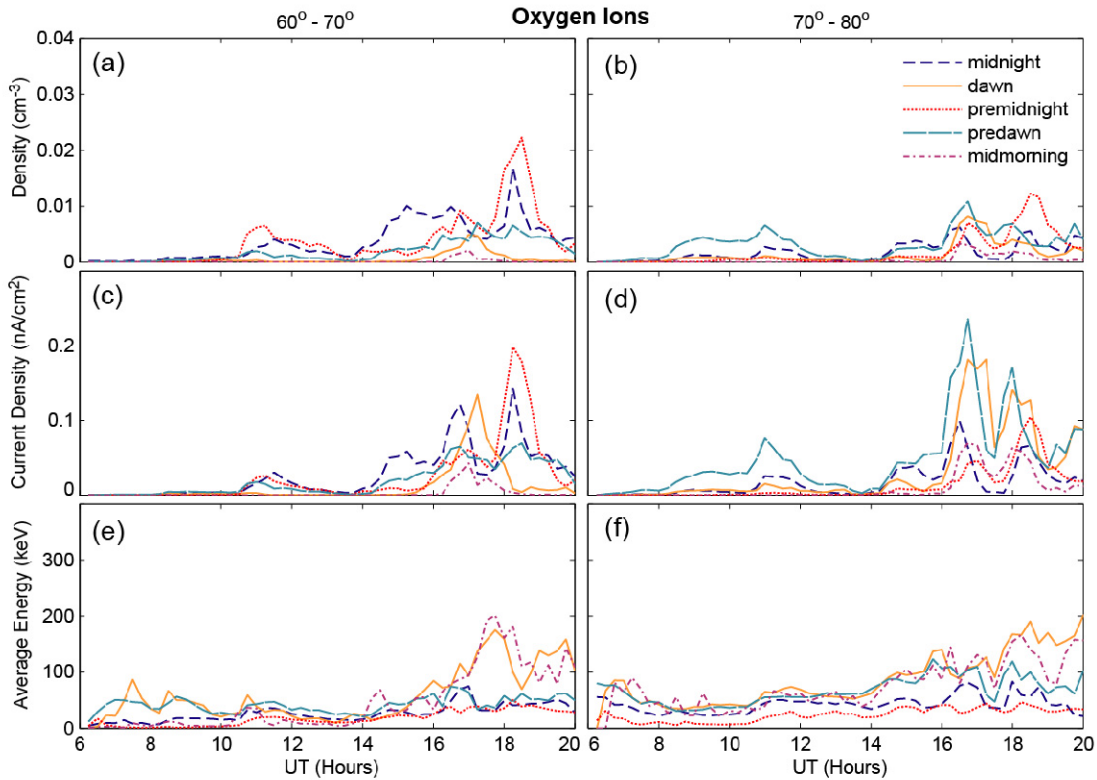


**Figure 5.10**  $O^+$  contribution to ring current (a and b) particle density and (c and d) current density from five ionospheric outflow regions extending from 19.5 MLT to 10.5 MLT for latitudes between  $60^\circ$  and  $70^\circ$  (column 1) and latitudes between  $70^\circ$  and  $80^\circ$  (column 2). (e and f) The average energies of particles originating for each of these outflow regions are also shown.

part of the storm (between 0800 and 1100 UT, Figure 5.10b). As the storm progresses, the midnight low sector becomes the dominant contributor to the RC density between 1400 and 1600 UT. During the main phase of the storm ( $\sim 1800$  UT), the premidnight sector at both low and high latitudes contributes significantly. Throughout the storm, the outflow regions from which particles experience the greatest levels of energization are the dawn and midmorning sectors (Figure 5.10e and Figure 5.10f). For the low-latitude outflow regions, the current density contributions closely follow the density contributions.

For  $H^+$  the premidnight, midnight, and predawn low-latitude sectors dominate the  $H^+$  density contribution to the RC during the majority of the storm. These regions are also the main contributors of the current density, even though they do not contribute the greatest energies. The greatest average energies are contributed by ions originating from the

midmorning and dawn sectors. For both  $H^+$  and  $O^+$ , the regions contributing most significantly to the total RC energy density tend to be the same regions which contribute the most particle density to the ring current, not necessarily the sectors with the largest average energies. These results agree with findings by *Lavraud and Jordanova* [2007] who used the kinetic drift-loss ring current-atmospheric model to simulate the effects of density and temperature on the proton ring current using idealized conditions and found that ring current strength is primarily controlled by the density.

In addition to considering the ring current energy density contribution for each outflow region separately, we also look at the total RC energy density for  $H^+$  and  $O^+$  summed over all outflow regions over the course of the storm (Figure 5.12). Results are shown both in terms of the total energy density in  $\text{keV}/\text{cm}^3$  (Figure 5.12b) and in terms of percent of the total (Figure 5.12c).

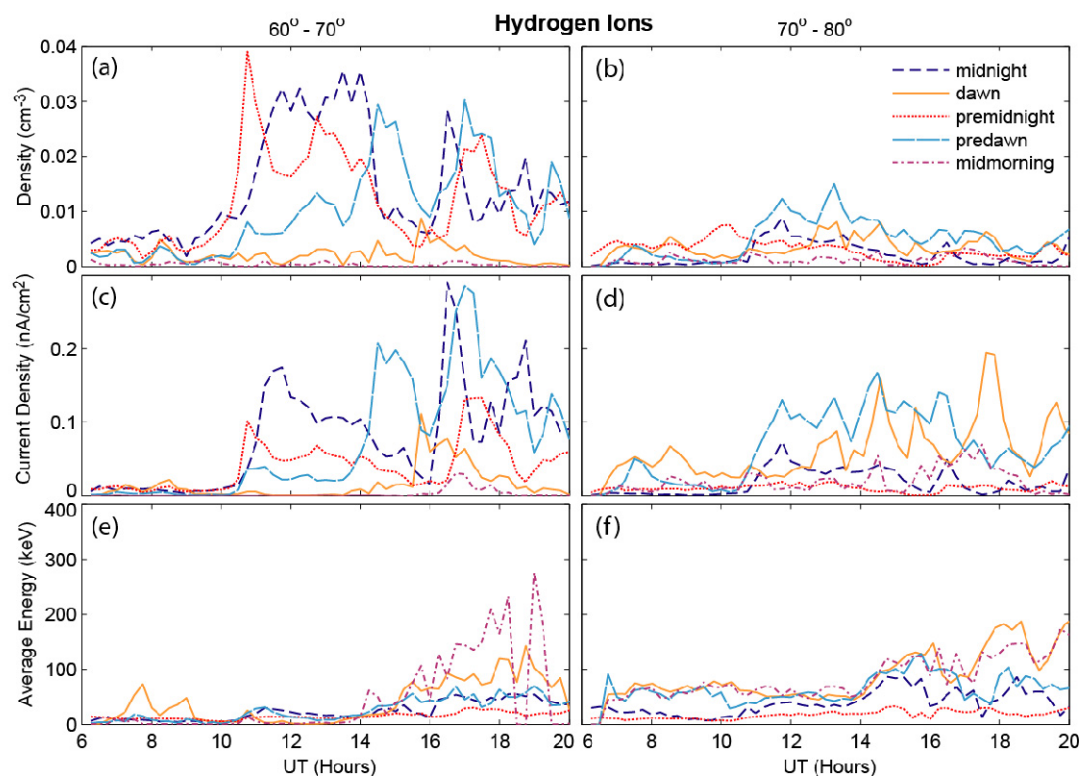


**Figure 5.11** Same format as Figure 5.10, but for  $H^+$  contribution to the ring current.

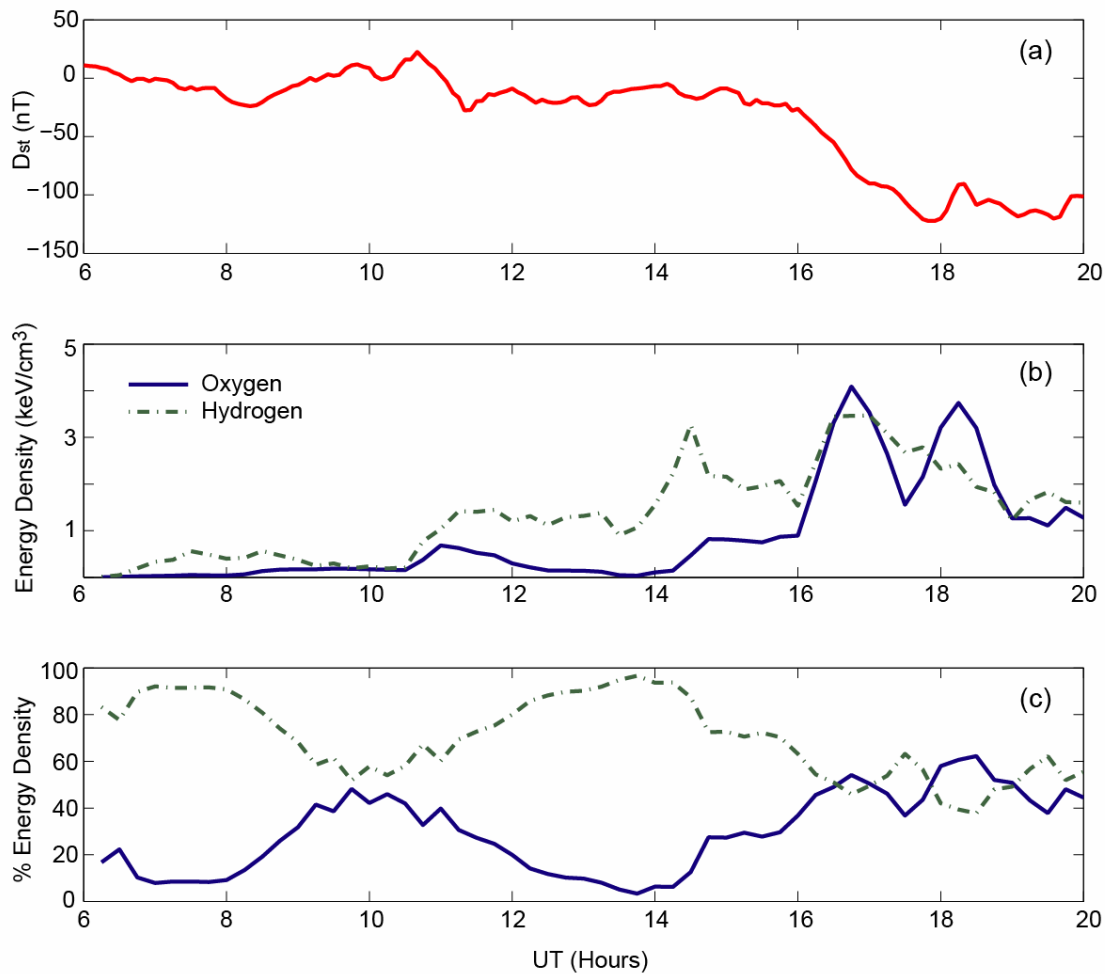


**Figure 5.12** (a) Geomagnetic  $Dst$  index plotted over the same time interval. Ring current energy density contribution from  $\text{H}^+$  (dashed green line) and  $\text{O}^+$  (solid blue line) over the course of the storm development (b) in terms of  $\text{keV}/\text{cm}^3$  and (c) as a percentage of the total ring current energy density from  $\text{H}^+$  and  $\text{O}^+$  of ionospheric origin.

Early in the storm  $\text{H}^+$  dominates contributing  $>80\%$  of the energy density at 0800 UT from ionospheric origin. Around 1100 UT an increase in the  $\text{H}^+$  energy density is observed along with a small increase in the  $\text{O}^+$  energy density. The  $\text{O}^+$  energy density then gradually declines between 1100 and 1400 UT. At 1600 UT when the  $Dst$  index begin to steeply decline, a steep increase in both  $\text{H}^+$  and  $\text{O}^+$  energy density is observed. At 1650 UT the  $\text{O}^+$  energy density reaches a peak value of  $4 \text{ keV}/\text{cm}^3$  and at this time the  $\text{O}^+$  energy density is greater than the  $\text{H}^+$  energy density. The increase in  $\text{O}^+$  corresponds to the decline in  $Dst$

observed to begin around 1600 UT and continue until 1800 UT. During the main phase of the storm  $H^+$  and  $O^+$  contribution to the energy density are roughly equal between 1700 to 2000 UT.

These results are consistent with findings by *Daglis* [1997] who, using CRRES spacecraft data, compared the relative contribution of  $H^+$  and  $O^+$  to the total ring current energy density for several storms that occurred in 1991 and found during the main decrease in *Dst*, the  $O^+$  contribution to the total RC energy density significantly increased relative to  $H^+$  for all storms. Significant variability between storms was observed for the amount of  $O^+$  energy density relative to  $H^+$ . For the 24 March 1991 storm,  $O^+$  contributed 66% of the total energy density at *Dst* minimum, whereas for the 4 June 1991, storm only about 55% of the energy density was from  $O^+$ . In some storms examined, the percent of  $O^+$  contribution to the ring current was as large as 70% [*Daglis et al.*, 1999], but in other storms, the contribution of  $O^+$  increased from <20% to ~50%.

In our simulation of the 10 March 1998 storm, we observe  $H^+$  and  $O^+$  contributions to the RC that are similar to those for the 6 April 1991 storm that was around 50%  $O^+$  contribution during the main phase of the storm. This increase in the  $O^+$  energy density contribution relative to the  $H^+$  contribution corresponds to the decline in *Dst*. We have also modeled two other geomagnetic storms occurring on 06 August 1998 and 29 October 2003, and particle tracking results for these storms also yield similar results to those for the 10 March 1998 storm: namely, early in the storm the  $H^+$  contribution dominates, while the  $O^+$  response is delayed and an increase in  $O^+$  energy density is not observed until later in the storm, corresponding to the minimum in *Dst*. For the 06 August 1998 storm,  $O^+$  contributes over 95% at 1215 UT, which corresponds to the minimum *Dst* value of -168 nT. The Halloween 2003 storm was a multi-day event with the first minimum in *Dst* occurring on 29 October 2003 at 0900 UT when *Dst* dipped to -212 nT. This decrease in *Dst* was associated with a peak in the  $O^+$  contribution to the ring current energy density: before 0730 UT the oxygen contribution was < 1%, while at 0900 UT oxygen reached a maximum contributing 63.5% of the energy density to the ring current. These results are

consistent with the findings by *Daglis* [1997] that large drops in *Dst* are due to an increased presence of oxygen from the ionosphere.

Comparing the model values for the  $H^+$  and  $O^+$  energy density to data [*Roeder et al.*, 1996], our values are roughly an order of magnitude too low for oxygen and 1-2 orders of magnitude too low for  $H^+$ . One reason for this may be that the energization rate is dependent on the initial energy of the ions and a higher initial energy may be required to obtain consistent results during storm time. Before the main decrease in *Dst* at 1600 UT, our values for oxygen are consistent with values observed for oxygen during substorms, whereas the values for  $H^+$  are lower than those typical of substorms [*Daglis et al.*, 1996]. One additional reason why our  $H^+$  results might be low while our  $O^+$  results agree with values reported by *Daglis et al.* [1996] is that  $H^+$  observed by satellites comes from both solar wind and ionospheric sources while the  $H^+$  in this study only comes from the ionosphere. Another potential reason could be due to the residence times of protons in the magnetotail, and perhaps not all the ring current ions come directly from the ionosphere, but some of these ions may enter the ring current after spending considerable time in the magnetotail.

## 5.6 Summary

The contribution of  $H^+$  and  $O^+$  of ionospheric origin to the storm time ring current has been investigated, specifically addressing how the contribution from 16 different ionospheric source regions varies over the course of the storm. Asymmetries are observed between  $H^+$  and  $O^+$  contributions.  $H^+$  begins contributing to the ring current densities much earlier in the storm development than  $O^+$  which could be explained by previous mass loading of the magnetotail by hydrogen ions. An increase in the contribution of  $O^+$  to the current density is observed from the predawn high-latitude region during each of the decreases in *Dst* examined for the 10 March 1998 storm. The dominant ionospheric species contributing to the ring current energy density is shown to vary during the course of the storm with a significant increase in ionospheric  $O^+$  contribution to the ring current associated with large decreases in *Dst*. Of the two decreases in *Dst* examined, one resembles more of a substorm

and the ring current is seen to be dominated by  $H^+$  energy density. The second decrease in  $Dst$  examined represents the main phase of the storm and a significant increase in the contribution of  $O^+$  to the storm time ring current is associated with this larger decrease in  $Dst$ .

Two factors that contribute to the increase in  $O^+$  concentration during the main phase of the storm are increased ionospheric outflow rate and increased efficiency at getting  $O^+$  into the inner magnetosphere. During the main phase of the storm, currents within the atmosphere heat the oxygen ions and raise their scale height, allowing an increase in  $O^+$  outflow to be observed. The multifluid model used to calculate the outflow rates uses a dynamic ionosphere and takes the currents that result in atmospheric heating into account. In addition to increased  $O^+$  outflow rates during the main phase of the storm, changes in the flow pattern of oxygen ions also results in increased oxygen contribution to the storm time ring current. During the early phase of the storm,  $O^+$  experiences strong cross-tail accelerations and, although there is earthward injection of the heavy ions, there are also significant losses of heavy ions down the tail. During the main phase of the storm, the oxygen ions experience stronger earthward acceleration, in association with the formation of a long, thin current sheet. These results agree with findings by *Daglis* [1997] and *Daglis et al.*, [1999] that during large storms, the ring current is dominated by particles of terrestrial origin and the percentage of  $O^+$  in the ring current significantly increases, with the simulation results for this event showing nearly 50–50 contributions to the ring current during the main phase of the storm.

More specifically, this work pinpoints the most likely origin of the ionospheric particles contributing to the storm time ring current contingent on the source location assumptions mentioned above. Through the use of single particle tracking, we find that during the early part of the storm, high-latitude outflow regions between 00 and 06 MLT are the most efficient sectors for contributing particle density to the ring current, whereas during the main phase of the storm there is a more even contribution from all MLTs, with the most efficient outflow regions being from low latitudes between 21 and 03 MLT. The variations in the source of outflowing ionospheric particles vary with the size, extent, and location of

the separatrix. During the early phase of the storm, a smaller more compact separatrix results in ring current particles originating from a limited region (mainly 00 to 06 MLT at high latitudes); however, during the main phase of the storm, the scope of the separatrix expands to include a wider source region and outflowing ions from all MLTs and latitudes contribute to the ring current.

Associated with the main phase of the storm and the large decrease in  $Dst$ , an overall increase in ionospheric outflow associated with the strongly southward IMF  $B_z$  is observed. This is associated with an expanded polar cap and contributions from all ionospheric outflow regions are observed. The sectors that contribute the majority of the energy are consistently the high latitude regions between 03 and 09 MLT. The results presented in this chapter provide a first link between MLT and magnetic latitude variations in ionospheric outflow and their individual contributions to the build-up of the ring current.

## Chapter 6: Importance of Temperature Anisotropies in Ring Current Development

This chapter uses the results from a newly developed multifluid code that incorporates temperature anisotropies to compare to single-particle tracking results. Both the isotropic and anisotropic versions of the multifluid code were run with the same initial conditions, which are described in section 6.3.1. The magnetic and electric fields from the isotropic version of the multifluid code were then used as inputs to the single-particle tracking model in order to compare the particle results, which are inherently anisotropic, with the results from the anisotropic version of the multifluid code.

Section 6.1 provides an overview of this chapter and section 6.2 discusses the motivation. In section 6.3.1 the boundary and initial conditions are discussed. Section 6.3.2 compares the moment results from the single particle tracking model to the results from both multifluid codes, and section 6.4 presents a summary of the major findings to date.

### 6.1 Overview

The 3D multifluid code has been used throughout this dissertation to model the magnetosphere for storm and substorm conditions, and this model does well at predicting substorm onset. This model also agrees well in the outer magnetosphere; however, the multifluid model consistently under predicts the intensity of currents in the inner magnetosphere, particularly during storm time. In order to resolve this issue, the multifluid code has been modified to incorporate temperature anisotropies [Kidder, 2011]. Building on previous single-particle tracking results which showed asymmetries between  $H^+$  and  $O^+$  energization mechanisms and injection into the ring current, this chapter applies single-particle tracking with time varying fields and compares these results to the isotropic and anisotropic versions of the multifluid model. Changes in ion number density, energy density, temperature and temperature anisotropies are examined during the development of

an idealized substorm. The bulk velocities and temperatures of plasma sheet ions are computed in three directions and distribution functions are compared between the single-particle tracking results and the isotropic and anisotropic versions of the multifluid model. This chapter also explores the development of the ring current using computed distribution functions discussed in section 6.3.2. It is known that in order for particles to contribute to the development of the ring current, a large component of the particle velocity needs to be in the perpendicular direction with respect to the magnetic field when the particle is in the inner magnetosphere. In this region, particles with high parallel velocities are lost into the atmosphere. Such results not only suggest the importance of including temperature anisotropies, but also point toward the underlying physical processes driving ring current enhancements. Anisotropies are physically necessary for convection and the isotropic-pressure approximation is inconsistent with magnetic-field models based on observations [Erickson and Wolf, 1980]. Instead of the idea of slow, steady, uniform, sunward convection in Earth's plasma sheet, sunward convection has been shown to be a time-dependant process in which plasma is suddenly and non-adiabatically released from plasma-sheet flux tubes. The inclusion of temperature anisotropies within physics-based models leads to the development of a stronger ring current.

## **6.2 Motivation**

Particle tracking results are inherently anisotropic. Particles can have different velocities in the  $x$ ,  $y$ , and  $z$  directions and the particles are able to respond to temperature anisotropies. Thus, particle tracking gives anisotropic results. In this way, particle tracking results can be used to compare to the newly developed version of the multifluid model which includes temperature anisotropies. This new anisotropic version of the multifluid code has yet to be validated and so the results in this chapter compare single-particle tracking results run using electric and magnetic fields from the isotropic fluid model to results from both the isotropic and anisotropic versions of the multifluid model. Results for all three methods are also compared with observations of known magnetospheric phenomena in order to identify which codes provide the most realistic description of the topology of the inner magnetosphere. Understanding what physics it is important to include in various regions of

the magnetosphere provides information about the physical processes that are important in those regions.

### **6.3 Comparison of Temperature Anisotropies**

For this comparison of temperature anisotropies between the multifluid versus single particle tracking results, both versions of the multifluid code were run using idealized solar wind conditions. In order to attain an initial equilibrium configuration for the magnetosphere, the simulations were run for 2 hours under quiescent conditions with IMF  $B_x$  and  $B_y$  set to 0 nT and IMF  $B_z$  set to 0.5 nT. Throughout the simulation a solar wind density of  $6 \text{ cm}^{-3}$  is used and the velocity of the solar wind is set to 450 km/s in the  $x$  direction, 30 km/s in the  $y$  direction, and 0 km/s in the  $z$  direction. Once an approximate equilibrium configuration is established, the  $B_z$  component of the IMF is increased to 2.5 nT at 0200 UT, and after additional 2.5 hours, the  $B_z$  component of the IMF is turned southward to  $-5$  nT at 0450 UT. Approximately one hour and 45 minutes later, the  $B_z$  component of the IMF is again turned northward, this time to 5 nT at 0623 UT.

The 3D simulations are solved on a ‘nested’ Cartesian grid system with varying resolution. In the highest resolution region, which extends from  $+14.7 R_E$  in the sunward direction to  $-44.3 R_E$  downtail,  $\pm 14.7 R_E$  in the  $y$  direction, and  $\pm 11.8 R_E$  in the  $z$  direction, the resolution is  $\sim 0.3 R_E$ . The resolution then increases with distance from the Earth to a resolution of  $2.4 R_E$  in the lowest resolution region, which extends from  $+47.2 R_E$  to  $-424.8 R_E$  in the  $x$  direction,  $\pm 118 R_E$  in the  $y$  direction, and  $\pm 94.4 R_E$  in the  $z$  direction. The largest grid defines the outer boundary of the simulation. The simulation inner boundary is set at  $2.6 R_E$  and the ionospheric density at the inner boundary held constant at  $200 \text{ cm}^{-3}$  for protons. The  $\text{O}^+$  density at the inner boundary varies in the vicinity of the auroral oval with a concentration of 5% of the proton density at auroral latitudes, typical for a period of low activity, and with the  $\text{O}^+$  concentration decreasing to zero at both the poles and the equator.

Electric and magnetic fields obtained from the multifluid model are saved at four minute intervals and a linear interpolation scheme is used to interpolate the field information between grid points and time steps (see section 3.2). For the particle tracking results presented in this chapter, only fields from the isotropic version of the multifluid code are used.

### **6.3.1 Particle Initialization**

Ionospheric hydrogen and oxygen ions are initialized on a grid slightly smaller than the highest resolution box in a region which extends from  $+7.4 R_E$  in the sunward direction to  $-44.3 R_E$  downtail,  $\pm 7.4 R_E$  in the  $y$  direction, and  $\pm 6 R_E$  in the  $z$  direction. In each of the 386,568 grid cells included in this region, ten superparticles are initialized, which results in a total of 3,865,680 particles initialized at the start of the simulation. Each superparticle represents roughly  $10^{21}$  ions. For both  $H^+$  and  $O^+$ , the particles are initialized in a Maxwellian distribution with a thermal velocity of 40 km/s. These initial parameters produce particles with average energies of 8 eV for  $H^+$  and 0.13 keV for  $O^+$ .

In order to account for the continuous outflow of ions from the ionosphere, every 30 seconds additional particles are injected into the simulation using a constant density method in which each of the grid cells in the spherical shell around the Earth maintains a density of 10 superparticles per grid cell. The spherical shell from which new particles are initialized is located near the inner boundary of the simulation and extends from  $\sim 3.5$  to  $4 R_E$  above the surface of the Earth. At 30 second time intervals, the density in each of the 4390 grid cells contained within the spherical shell is determined and for cells where there are fewer than 10 superparticles per cell, additional particles are added to maintain a constant density in this initialization region. This method continuously injects particle into the regions with the largest outflow rates, while supplementary particles are not added to regions where the ions are less mobile.

The total number of particles in the simulation at any giving time is limited to 10 million, and after 30 minutes of simulated time,  $\sim 4.8$  million particles have accumulated in the

inner magnetosphere. Using the constant density method to inject particles into the simulation,  $\sim 17,000$  superparticles are added to grid cells near the inner boundary every 30 seconds, yielding an outflow rate of approximately  $5.7 \times 10^{23}$  ions/sec.

### 6.3.2 Moments of the Ion Distribution Function

The previous two chapters explored the dynamics of individual particles, in this chapter the distribution function and the resulting moments of the particle distribution function are calculated. The particle distribution function is computed at each grid cell for all simulation space by linearly interpolating the particles onto the nearest grid cells. The moments of the particle distribution are then calculated at each grid point using the following equations

$$n_p(x, y, z) = \int f(x, y, z, \mathbf{v}) d^3\mathbf{v} \quad (6.1)$$

$$\mathbf{V}_p(x, y, z) = \frac{1}{n(x, y, z)} \int \mathbf{v} f(x, y, z, \mathbf{v}) d^3\mathbf{v} \quad (6.2)$$

$$P(x, y, z) = \frac{m}{3} \int f(x, y, z, \mathbf{v}) (\mathbf{v} - \mathbf{V}_p)^2 d^3\mathbf{v} \quad (6.3)$$

$$T = \frac{P(x, y, z)}{n(x, y, z)} \quad (6.4)$$

$$P_{ij}(x, y, z) = m \int (\mathbf{v} - \mathbf{V}_p)_i (\mathbf{v} - \mathbf{V}_p)_j \cdot f(x, y, z, \mathbf{v}) d^3\mathbf{v} \quad (6.5)$$

where  $n$  is the density,  $\mathbf{v}$  is the individual particle velocity,  $\mathbf{V}_p$  is the average bulk particle velocity,  $P$  is the scalar pressure for an isotropic plasma,  $m$  is the ion mass,  $T$  is the temperature, and  $P_{ij}$  is the pressure tensor for a non-isotropic plasma. The distribution function is determined at each grid point for all velocity space by interpolating the particle

equivalent density and velocity onto the nearest grid points and summing over all simulation particles.

Results for the calculated particle moments are compared to multifluid results for both the isotropic and anisotropic versions of the fluid code. By calculating the moment equations, the bulk particle density, velocity, and pressures can be compared to results from the multifluid model. All figures in section 6.4 are for a time  $\sim 30$  minutes after the IMF  $B_z$  component turned southward to  $-5$  nT at approximately 0500 UT.

## 6.4 Results

In Figure 6.1, a comparison of the densities shows differences between the isotropic and anisotropic versions of the multifluid model for hydrogen and oxygen ions. For both ion species the inner magnetosphere and tail regions show appreciable differences. The isotropic code yields a greater ion density near the magnetopause boundary (Figure 6.1a and Figure 6.1d), while in the anisotropic results there are higher densities over the polar regions (Figure 6.1b) and the distribution is more spherical in nature, especially for oxygen ions (Figure 6.1e). Slightly different color bars were used for  $H^+$  and  $O^+$  to allow for maximum contrast in order to bring out the finer detail in the density variations within the inner magnetosphere.

Particle tracking results are shown in the bottom two plots in Figure 6.1. In these images the density at each grid cell is calculated and the relative densities are shown in panels (c) and (f). The densities obtained from the particle tracking results have been scaled in such a way as to allow for easy visual comparison with the multifluid results, and thus the particle tracking results are showing the relative densities within the magnetosphere and are in arbitrary units that are not necessarily in the same units as the color bars. Comparison between the particle results and the multifluid results is difficult given the limitation of particle statistics and the difficulty resolving fine structures within the particle density distribution.

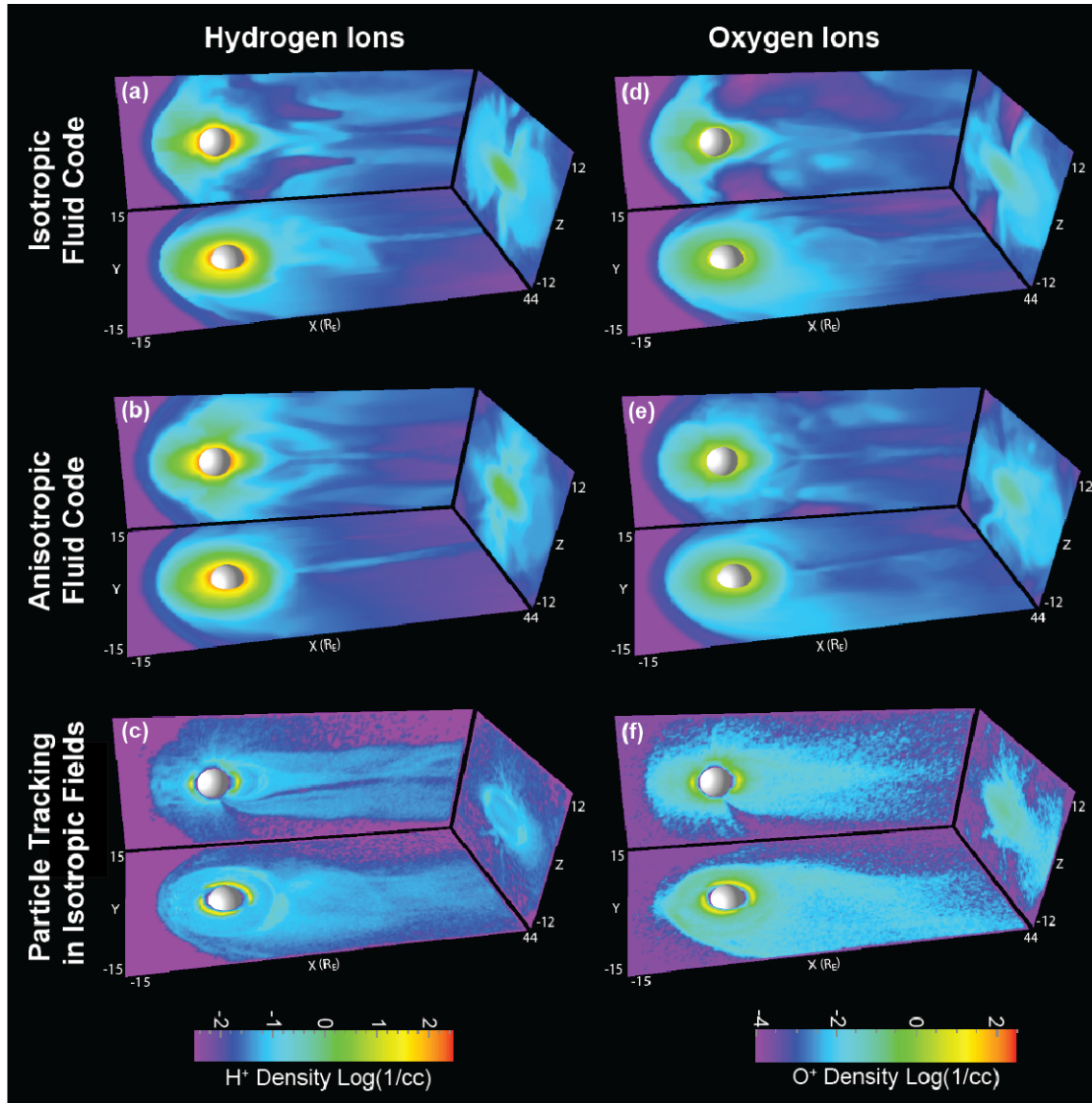


**Figure 6.1** Density plots from the isotropic and anisotropic multifluid codes as well as the density obtained from the single particle tracking code. Results are shown for hydrogen and oxygen ions and note that each has a slightly different color bar. Particle tracking results are only showing the relative densities.

Differences are also observed comparing the scalar pressure results for the three different codes (Figure 6.2). In the tail region and the inner magnetosphere the anisotropic code produces a longer, thinner current sheet and achieves higher overall pressures within the inner magnetosphere, particularly on the dusk side. As with the density plots, slightly different color bars were used for  $H^+$  and  $O^+$  in order to allow for maximum contrast and to bring out fine detail in variations in the scalar pressure within the inner magnetosphere.

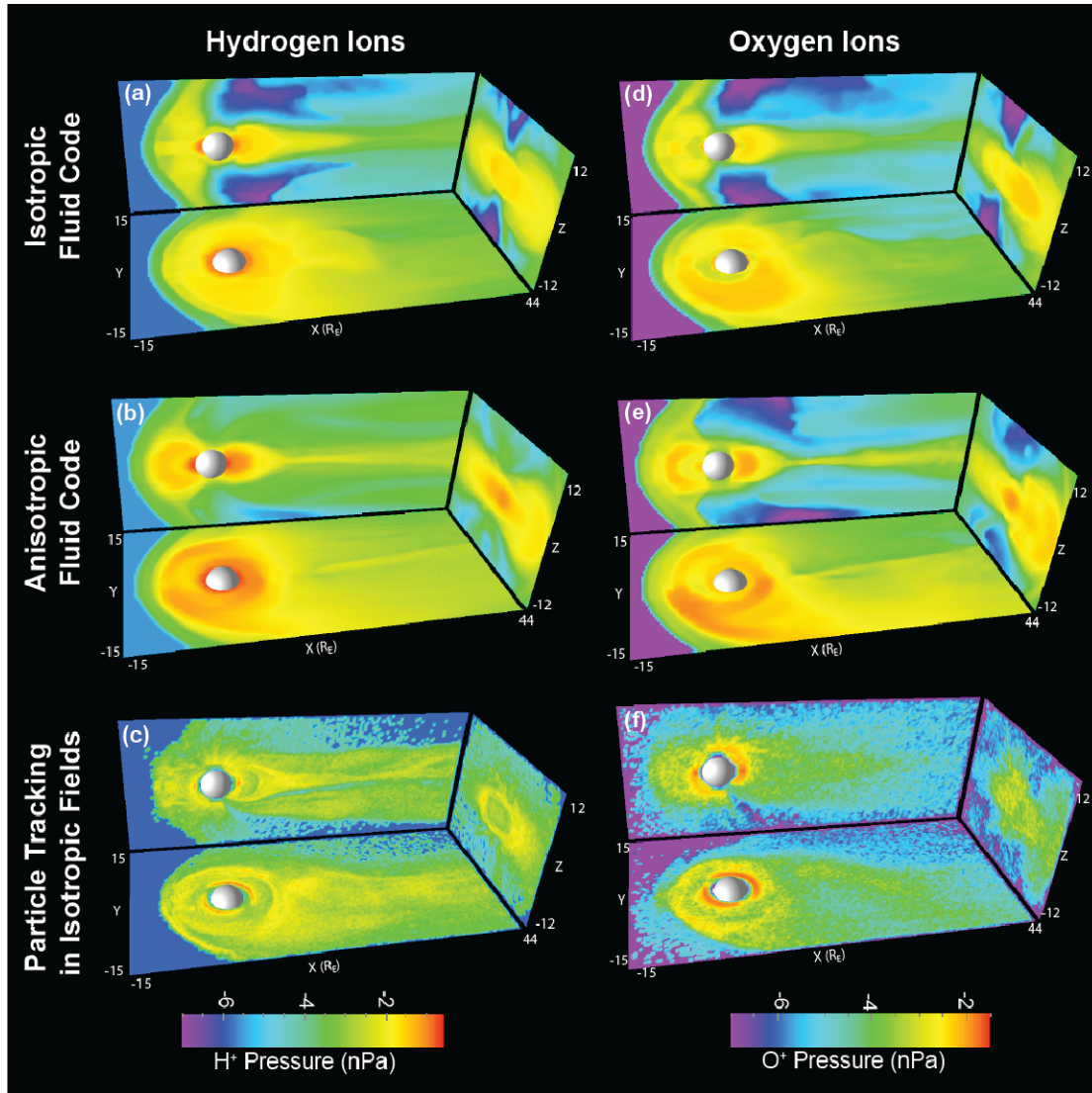


**Figure 6.2** Pressure plots from the isotropic and anisotropic multifluid codes as well as the pressure obtained from the single particle tracking code. Results are shown for hydrogen and oxygen ions and note that each has a slightly different color bar.

Particle-tracking results show some fine-scale structure, particularly for the hydrogen ions. Features such as the enhancement on the dusk side of the magnetopause, the high pressure region confined to the inner magnetosphere, and the lack of high pressure extending along the magnetopause in the  $z$  direction, all suggest that the particle tracking results more closely resemble the results from the anisotropic fluid model. These similarities can also be seen in the tail region, where a higher pressure current sheet extends in the  $x$  direction for the entire length of the image and higher pressure regions are also observed above and

below the current sheet compared to the isotropic case. For oxygen ions it is more difficult to compare to the multifluid results. One notable difference is the lack of an enhanced pressure region along the length of the magnetopause in the north / south direction in the anisotropic and particle-tracking results, while the isotropic code seems to consistently produce higher pressure along the length of the magnetopause. For both  $H^+$  and  $O^+$  the particle-tracking results seem to agree better with the results from the anisotropic model.

Model results are also compared with observations. In Figure 6.2b the current sheet has a thickness of  $\sim 1 R_E$ , which agrees with Cluster spacecraft observations of a thin current sheet extending  $1 R_E$  in the vertical direction during a quiet magnetosphere [Nakamura *et al.*, 2002]. In Figure 6.2c on the night side a region of low particle pressure is observed between two regions of higher pressure. This feature looks similar to the slot region known to exist between Earth's inner and outer radiation belts; however, the region of lower pressure in Figure 6.2c is located between 4 and 6  $R_E$  while the slot region, which is mainly observed in the electron radiation belts, is located between 2 and 3  $R_E$  [Ganushkina *et al.*, 2011]. Overall the enhanced presence large anisotropies in the dusk/dawn direction and the larger plasma pressure on the dusk side of the magnetosphere, suggest that the anisotropic fluid model is more realistic than the isotropic fluid model. The particle tracking results show increased pressure in the ring current region between dusk and midnight, which would be consistent with energetic ions injected into this region.

Using the newly developed anisotropic code, the anisotropic temperatures can be compared to the particle-tracking results in the  $x$ ,  $y$ , and  $z$  directions. For the single-particle tracking results, the temperature anisotropies were calculated by taking  $P_{xx}$ ,  $P_{yy}$ , and  $P_{zz}$ , at each grid cell and dividing these values by the density at each grid cell. The square root of the pressure divided by the density term was taken to obtain the thermal velocity in the  $x$ ,  $y$ , and  $z$  directions. In these results the temperature anisotropy is defined as a vector with components in the  $x$ ,  $y$ , and  $z$  directions; this definition differs from the standard definition of temperature anisotropy which is defined as the component perpendicular to the magnetic field divided by the component parallel to the magnetic field. Here the anisotropies are calculated relative to the  $x$ ,  $y$ , and  $z$  directions and are not dependent on the magnetic field.

The temperature anisotropies as defined in this chapter are obtained using the following

$$\delta = \left( \frac{3}{\sqrt{P_{xx}} + \sqrt{P_{yy}} + \sqrt{P_{zz}}} \right) \cdot (\sqrt{P_{xx}}, \sqrt{P_{yy}}, \sqrt{P_{zz}}) \quad (6.6)$$

Thus each component of the temperature anisotropy vector, defined above, is a unitless number between 0 and 3. In this way, when the value of the root mean square is the same in all directions, thus isotropic, a value of 1 is obtained for the temperature anisotropy at that location in each direction. When all of the thermal velocity is only in one direction, then the value for the temperature anisotropy in the given direction is 3 while the value of the temperature anisotropies in the other two directions would be 0. This is the method used to plot the temperature anisotropies discussed in Figure 6.3 and Figure 6.4, which show the temperature anisotropy results for  $H^+$  and  $O^+$ , respectively.

For the hydrogen ions shown in Figure 6.3, the single-particle tracking results more closely resemble the anisotropies generated by the anisotropic fluid code, particularly in the inner magnetosphere, compared to the results generated by the isotropic fluid model. Both codes produce regions of low temperature above and below the poles and increased temperature along the magnetopause in the  $x$  directions (Figure 6.3a and Figure 6.3d). However in the current sheet and tail regions these two codes do not agree as well with the fluid code producing regions of high  $P_{xx}$  above and below the thin current sheet (Figure 6.3a), while the inverse is observed in the results from the particle-tracking code, in which these same regions indicate low anisotropies in the  $x$  direction (Figure 6.3d). The greater variation observed in the tail of the particle-tracking results could be attributed to the lower particle statistics in this region due to the particle injection method used in which after the initial injection over a large area, particles are only added to the simulation in a spherical shell near the inner boundary of the simulation. The anisotropies in the  $y$  direction seem to agree relatively well in the tail, but not as well in the inner magnetosphere within  $\sim 4 R_E$  above and below the poles. This could again be due to the way in which the ions are initialized at the inner boundary (with a large velocity in the  $x$  and  $y$  directions, but a smaller velocity in

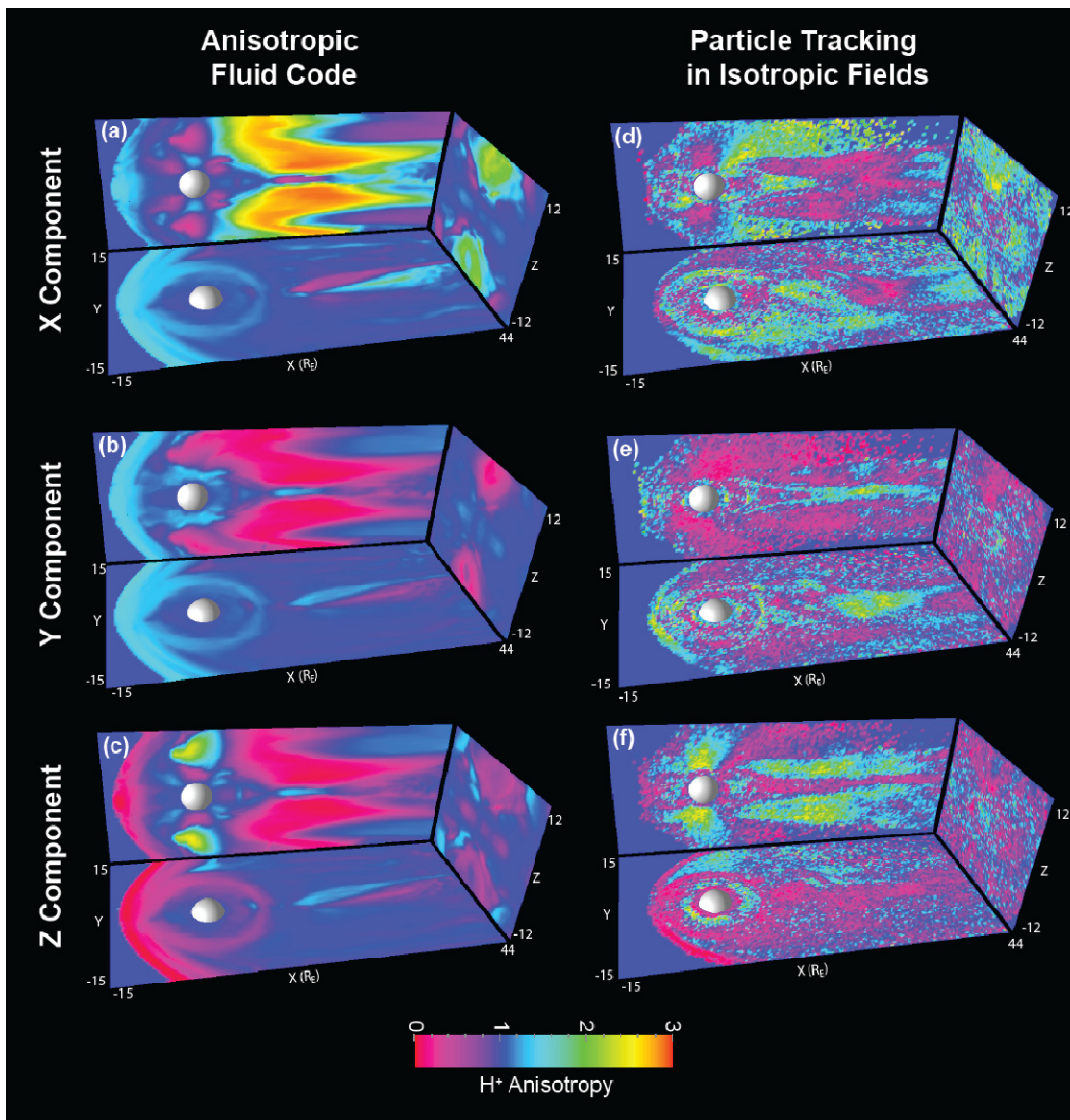


**Figure 6.3** Temperature anisotropy plots in  $x$ ,  $y$ , and  $z$  directions for hydrogen ions for the anisotropic fluid code (left side) and single particle tracking code (right side). Results show differences in the temperature anisotropies in all three directions. Single particle tracking results do not agree well in the inner magnetosphere and more particle statistics are needed to compare the anisotropies in the tail and lobe regions. In these results temperature anisotropies are calculated by taking the normalized thermal velocities in  $x$ ,  $y$ , and  $z$  directions and dividing these by the mean temperature at each grid cell.

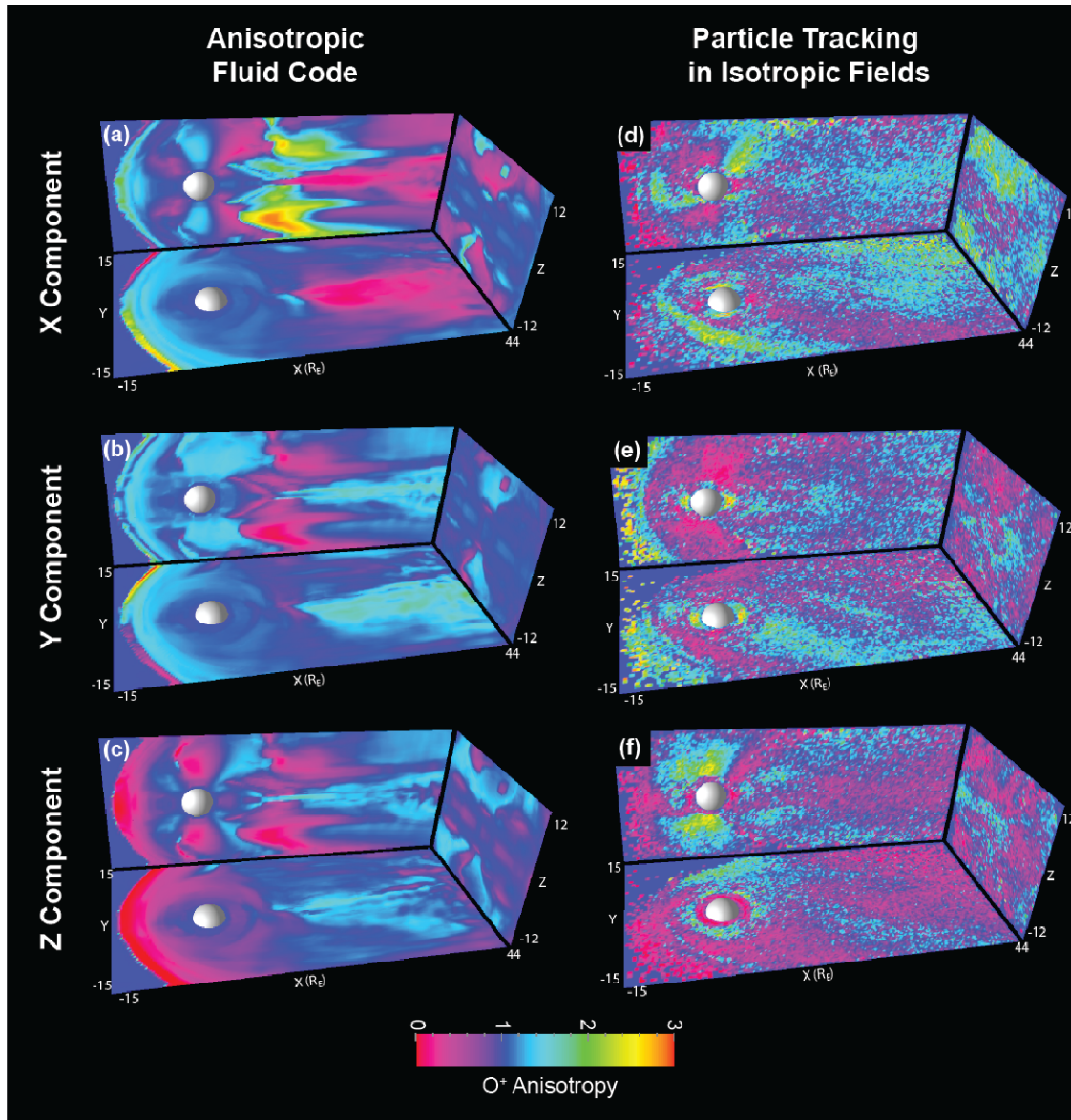


**Figure 6.4** Temperature anisotropy plots in  $x$ ,  $y$ , and  $z$  directions for oxygen ions for the anisotropic fluid code (left side) and single particle tracking code (right side). Results show differences in the temperature anisotropies in all three directions. Single particle tracking results do not agree well in the inner magnetosphere and more particle statistics are needed to compare the anisotropies in the tail and lobe regions. In these results temperature anisotropies are calculated by taking the normalized thermal velocities in  $x$ ,  $y$ , and  $z$  directions and dividing these by the mean temperature at each grid cell.

the  $z$  direction). In the bottom two panels, (c) and (f), large anisotropies in the  $z$  direction are observed over the poles in both images, while the tail shows the inverse with low anisotropies in the  $z$  direction above and below the thin current sheet (Figure 6.3c). Again the variation observed in the tail could be attributed to lower particle statistics and a different method for injecting the particles into the simulation may need to be considered, either initializing some particles in the tail or running the simulation much longer to allow for increased mass loading of the inner magnetosphere.

While the two models agreed in some regions of the magnetosphere and not in others for  $H^+$  ions, the  $O^+$  results are more difficult to decipher. The magnetopause appears to agree well in all six of the images in Figure 6.4. The  $x$  and  $y$  directions indicate large temperature anisotropies in the magnetopause in the  $xy$  plane. In the inner magnetosphere the particle-tracking model produces results that are the inverse of the fluid results, and outside of the inner magnetosphere it is difficult to compare the results due to the lack of fine structure observed in the single-particle tracking results for  $O^+$ . Thus the results in Figure 6.3 and Figure 6.4 are complicated to dissect since some regions agree well while others do not.

In order to further explore these anisotropies magnetic field lines are plotted on top of a color contour indicating the temperature anisotropies in the  $x$ ,  $y$ , and  $z$  directions for hydrogen and oxygen ions (Figure 6.5 and Figure 6.7, respectively). The top two panels in Figure 6.5 show the anisotropies in the noon-midnight meridian. In Figure 6.5a anisotropies in the  $x$  direction show large field-aligned temperature anisotropies in the tail above and below the current sheet where the field lines are mainly in the parallel to the ecliptic plane. In Figure 6.5b anisotropies in the  $y$  direction indicate minimal temperature anisotropies in the tail. In the bottom panel anisotropies in the  $z$  direction are plotted in the equatorial plane with the same magnetic field lines drawn in white in the above two images. L-shells of 4 and 8 are marked with yellow circles, and the ring current is located within this region. As can be seen in Figure 6.5c, the field lines are mainly dipolar in the ring current region and the low anisotropies in the  $z$  direction indicate that there is a large perpendicular temperature anisotropy.

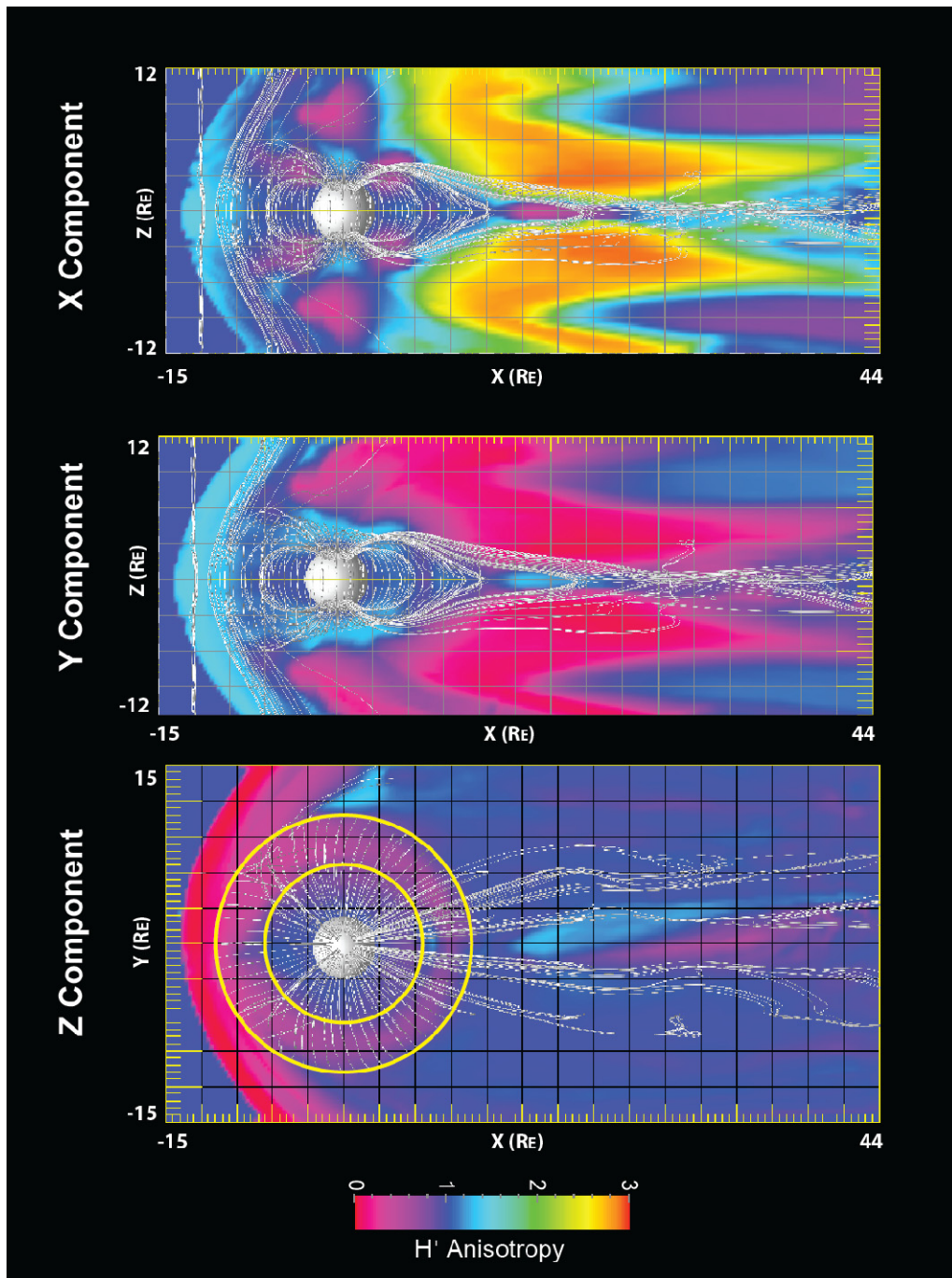


**Figure 6.5** White magnetic field lines plotted on top of a color contour indicating the temperature anisotropies for hydrogen ions in the  $x$ ,  $y$ , and  $z$  directions. (a) anisotropies in the  $x$  direction. (b) anisotropies in the  $y$  direction. (c) anisotropies in the  $z$  direction in the equatorial plane. Yellow circles define the L-shells of 4 and 8. In the region bounded by the yellow circles (the ring current region) field lines are mainly dipolar and the low anisotropies in the  $z$  direction indicate that there is a large perpendicular component to the temperature in this region.

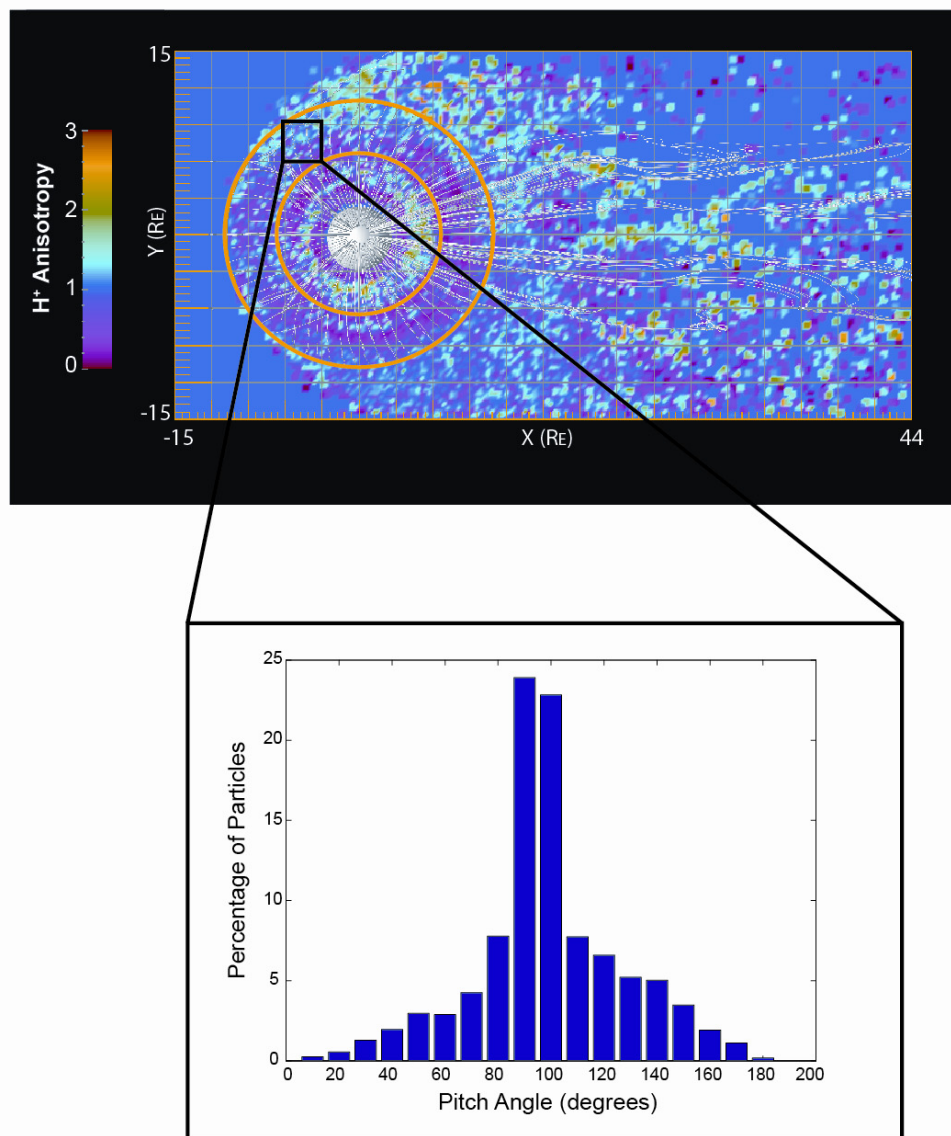


**Figure 6.6** Same region and time as Figure 6.5c but for the particle-tracking results. (a) white magnetic field lines plotted on top of a color contour indicating the temperature anisotropies for hydrogen ions in the  $z$  direction in the equatorial plane. Yellow circles define the L-shells of 4 and 8 (the ring current region) and in this region a large perpendicular component is observed, in agreement with the results shown in Figure 6.5c. (b) a bar graph showing the percentage of particles with a given pitch angle in a region where the agreement is not as clear. The vast majority of particles (>50%) have pitch angles between 70 and 110 degrees.

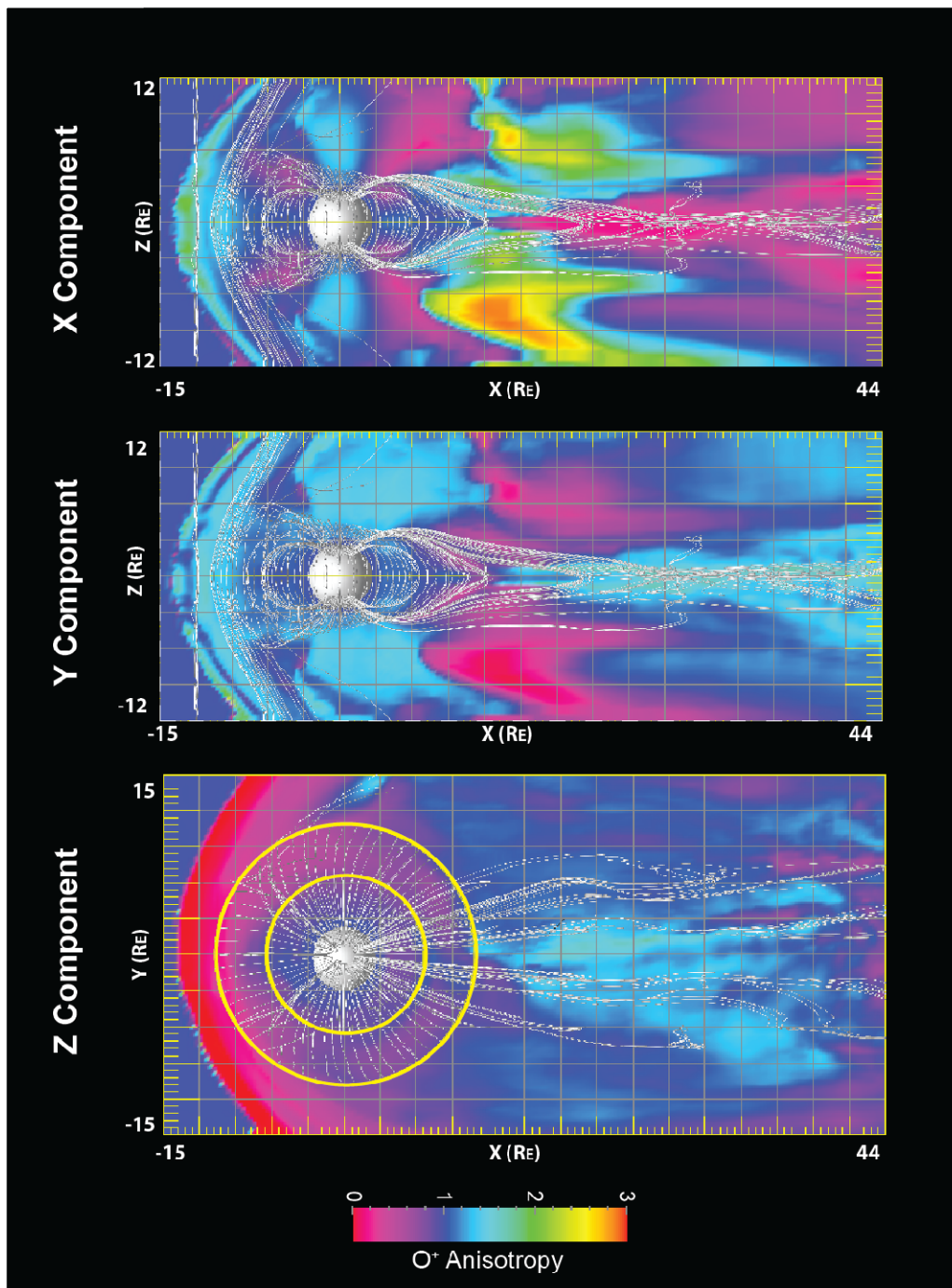


**Figure 6.7** Same as Figure 6.5 but this time showing results for oxygen ions. (a) anisotropies in the  $x$  direction are not as large or extensive as those observed for hydrogen ions. (b) large anisotropies in the  $y$  direction can be seen in the current sheet. Over the polar regions anisotropies are mainly observed in the  $x$  and  $y$  directions. (c) anisotropies in the  $z$  direction show a large perpendicular component to the temperature in the ring current region (within the yellow circles), similar to the results for hydrogen ions.

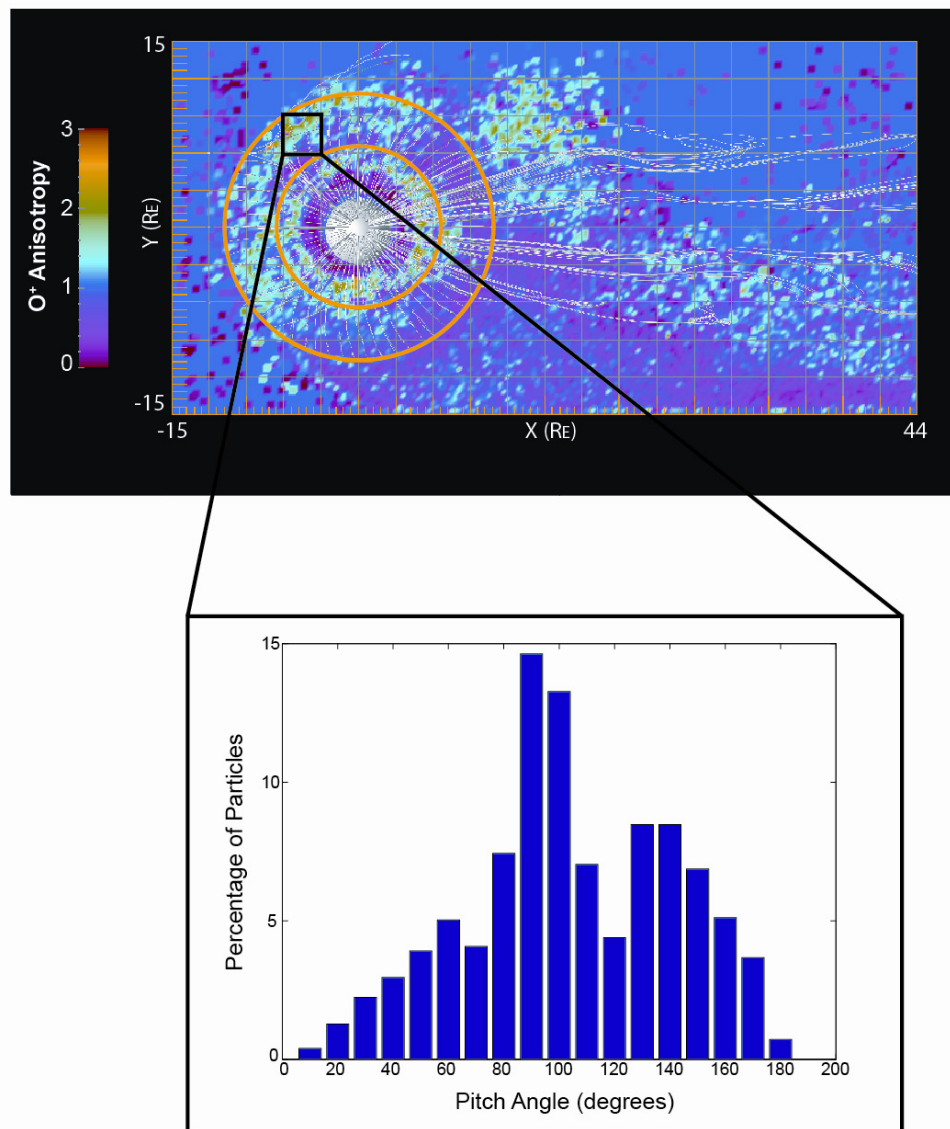


**Figure 6.8** Same as Figure 6.6 but showing results for oxygen ions. (a) within the ring current region, indicated by the yellow circles at 4 and 8  $R_E$ , the temperature anisotropies vary from mainly perpendicular to the magnetic field lines (night side) to regions with a high parallel component (day side). (b) a bar graph showing the percentage of particles with a given pitch angle in the region enclosed by the black square. For oxygen ions, the distribution is not as peaked as the distribution for hydrogen ions. Less than 50% of the particles have pitch angles between 70 and 110 degrees. Second smaller peak is observed centered around 130 degrees.

Comparing Figure 6.5c with particle-tracking results, Figure 6.6 shows the same color contour type plot for the  $H^+$  temperature anisotropies in the  $z$  direction in the equatorial plane. The ring current region is again marked with yellow circles and in this region a large perpendicular component is observed, in agreement with the results shown in Figure 6.5c. For one section of the ring current marked with a black square, the pitch angle distribution is plotted (Figure 6.6b). The magnetic field in this region is assumed to be entirely in the  $z$  direction and the pitch angle distribution shows that the vast majority of particles (>50%) have pitch angles between 70 and 110 degrees.

Results similar to those shown in Figure 6.5 are given for oxygen ions in Figure 6.7. In the top panel the anisotropies in the  $x$  direction are not as large or extensive as those observed for hydrogen ions. In the middle panel large anisotropies in the  $y$  direction can be seen in the current sheet. Over the polar regions anisotropies are mainly observed in the  $x$  and  $y$  directions indicating minimal temperature anisotropies in the  $z$  direction. Anisotropies in the  $z$  direction show a large perpendicular component in the ring current region (within the yellow circles), similar to the results for hydrogen ions.

Figure 6.8 is similar to Figure 6.6 but showing results for oxygen ions. Within the ring current region, indicated by the yellow circles at 4 and 8  $R_E$ , the temperature anisotropies vary from mainly perpendicular to the magnetic field lines (night side) to regions with a high parallel component (day side). When looking at the histogram of the pitch angle distribution for the region enclosed by the black square, the distribution is not as peaked as the distribution for hydrogen ions. Less than 50% of the particles have pitch angles between 70 and 110 degrees, and for oxygen ions a second smaller peak is observed centered around 130 degrees.

## **6.5 Summary**

Single-particle tracking results run using electric and magnetic fields from an isotropic version of the multifluid model have been compared to results from both the isotropic and anisotropic versions of the multifluid model. In order to identify which codes provide the

most realistic description of the topology of the inner magnetosphere, results for all three methods were also compared with observations of known magnetospheric phenomena. For the parameters analyzed in this chapter, the particle-tracking results consistently seem to more closely resemble the anisotropic model, and both of these models capture common magnetospheric features. These results suggest that incorporating temperature anisotropies within the multifluid model is important in order to realistically capture particle dynamics within the multifluid model.

Evaluating the moments of the particle distribution is not only helpful for model-to-model comparison, but is also the next step in the process of generating a combined multifluid / particle model, which incorporates particle tracking within the anisotropic multifluid model. While having two separate models has allowed the same electric and magnetic fields to be used several times to investigate the response of different ion species from several source regions over a similar timescale, these two separate codes permit only one-way communication between the two models: the fluid code generates background field information and the particle code uses that information as input. Combining these two models into one coupled model would allow for feedback between the particle dynamics and the global multifluid code with the ability to generate a self-consistent description of both large and small-scale magnetospheric processes.

The aim of this chapter has been to calculate the moments of the particle distribution, which will be used to incorporate particle feedback in a self-consistent model, and to compare the calculated moments and anisotropies with results from the multifluid model. In these results, more particle statistics, especially in the tail, would greatly aid in the comparison between the single-particle tracking results and the multifluid results. Discrepancy between the temperature anisotropies calculated from the single-particle tracking results and those obtained in the multifluid model also need to be further explored before the contributions from the particle distribution functions can be included in the bulk velocity and current density in Ohm's law, providing particle feedback within a combined multifluid / particle code. In such a code, the particles would contribute to the computation

of the electric field using an updated ion velocity in the modified Ohm's law and then this updated electric field would be incorporated into the remaining fluid equations through the induction equation, which is used to update the magnetic field, and the momentum equation. In this way the particles would be able to influence the electric and magnetic fields in the multifluid simulation and produce a self-consistent particle / multifluid model. However, before this can be achieved reliable bulk particle moments must be attained.

One of the difficulties mentioned in this chapter is the limitation due to particle statistics, particularly in the magnetotail. Number densities within the terrestrial magnetosphere span several orders of magnitude as one travels from the dense plasmasphere ( $10^2$ - $10^4$   $\text{cm}^{-3}$ ) to the tenuous lobes ( $0.01$   $\text{cm}^{-3}$ ), and this presents the problem of what constitutes a statistically accurate sample of particles in a grid cell. A doubling or tripling of particle densities in the lobe would correspond to uncertain fluctuations in the inner magnetosphere. Thus the issue of particle statistics needs to be addressed before incorporating the effects of the particle population on the electric and magnetic fields through the simulation space.

## Chapter 7: Space Weather Implications for Extrasolar Planets

In addition to contributing to the development of the ring current, energetic particles that precipitate into a planet's atmosphere can excite the atoms and molecules in the upper atmosphere and create aurora. Auroras are seen on all planets in our solar system with magnetic fields, and it is expected that auroras are also present on exoplanets that possess magnetic fields. This chapter focuses on the possibility of detecting extrasolar planet UV auroral emissions, which likely have the greatest prospects for observability. There are numerous reasons to search for and study auroral emissions generated by extrasolar giant planets (EGPs). First, UV auroral emission is a means of detecting a planet directly as opposed to the indirect methods employed to date, such as radial velocity and pulsar timing [Udry *et al.*, 2006; Bastian *et al.*, 2000; Charbonneau *et al.*, 2006]. Second, detecting an obvious auroral signature would provide evidence of the presence of a planetary magnetic field [Bhardwaj and Gladstone, 2000a], a benefit unique to this detection method. Third, UV auroral emission could play a role in characterizing the near-space environment around these planets, providing information about basic atmospheric composition and the deposition energies of the impacting particles. Fourth, most stars with orbiting extrasolar planets do not have continuum emission in the UV, so by observing the ultraviolet aurora, more favorable contrast ratios could be obtained compared to observations at visible wavelengths.

### 7.1 Overview

This chapter presents an analysis of the expected ultraviolet auroral emission strengths from extrasolar giant planets and the feasibility of detecting such exoplanetary aurora. Using Jupiter as a template and taking into account some basic properties involved in auroral production, possible emission fluxes are estimated for a given set of planetary system parameters. Via this global approach, the influence of various physical parameters

on auroral emission is investigated and the possibility of detecting UV auroral emissions with current and future technology is discussed. Potential candidate planets for UV observation are presented.

## **7.2 Background**

### **7.2.1 EGP Detection Methods**

Since the discovery of the first extrasolar planet by *Mayor and Queloz* [1995], over 697 extrasolar planets have been identified orbiting 573 stars of spectral types F to M, with 81 known multi-planet systems<sup>1</sup>. The majority of the planets discovered to date have been found via indirect methods of detection that rely on observing a planet's effects on the host star. The most successful indirect detection technique is the radial velocity method in which the influence of a planet's gravity on the host star is measured [*Beuzit et al.*, 2006; *Udry et al.*, 2006]. Other indirect methods used to date include pulsar timing [*Wolszczan*, 1994], photometric transits [*Charbonneau et al.*, 2006], and gravitational microlensing [*Bond et al.*, 2004].

While indirect methods work well for initial planet detection, the amount of planetary information they provide is limited. From radial velocity measurements, a planet's orbital period and eccentricity can be derived; however, the unknown inclination angle of the planet's orbit only allows an estimation of the planet's minimum mass,  $M_p \sin(i)$ . Direct UV auroral detections would offer new qualitative information about these planets, i.e. information about the planet's magnetic field, magnetosphere, near-space environment, and composition of the upper atmosphere.

### **7.2.2 Planetary Magnetic Fields**

One of the properties that could be determined by a direct detection of an exoplanetary aurora is the presence of a magnetic field. Our solar system only provides a small sample

---

<sup>1</sup> <http://exoplanet.eu/catalog.php> accessed November 13, 2011

of planetary magnetospheres; identifying exoplanetary magnetospheres would add to the diversity of planets available for comparative study. Knowledge of whether extrasolar planets possess magnetic fields is important for understanding how magnetic fields form and persist. Despite continued research on the dynamo mechanism, the conditions necessary for the existence of a planetary dynamo remain imperfectly understood [Stevenson, 2001]; however, the composition and structure of the core, as well as the planetary rotation rate, are all believed to influence the strength of planetary magnetic fields.

From an astrobiological perspective, the presence of a planetary magnetic field may be required for life to persist on a planet or satellite. The effects of a planetary magnetic field on life are not entirely understood, but it is known that a magnetosphere reduces the rate of atmospheric escape due to ion sputtering [Rochette, 2001; Lammer *et al.*, 2001]. Magnetic fields also provide protection from destructive cosmic radiation – high energy particles known to cause devastating mutagenic effects on surface organisms [Rochette, 2001]. A more speculative connection is the possible necessity of a magnetic field for the genesis of life. Magnetic fields may have influenced the complex chemical reactions that lead to life through the effect of magnetic fields on electronic energy levels and on the orientation of magnetically anisotropic molecules [Weaver *et al.*, 2000]. A recent experiment by *Rikken and Raupach* [2000] demonstrated that magnetic fields can produce chiral imbalance in molecules, which would affect key prebiotic chemical reactions.

While the specifics of the relationship between magnetic fields and life are not entirely understood, the possible connections suggested above imply that planetary magnetism could likely be linked to the possibility of extant life on other planets. In this way, the question of whether extrasolar planets have magnetic fields is a question of interest to astrobiologists.

### **7.2.3 Future of EGP Characterization**

Despite the steadily increasing number of extrasolar planet detections, there remains limited availability to describe and characterize EGPs. For the nine planets known to transit their parent star, accurate estimates of mass and radius can be obtained, placing constraints on the physical structure of these bodies [*Charbonneau et al.*, 2006]. Transits also offer a means to investigate the atmospheres of these exoplanets through the use of transmission spectra (See *Seager and Sasselov*, [1998]; *Charbonneau et al.*, [2002]; *Vidal-Madjar et al.*, [2003, 2004]).

Searching and studying UV auroral emission could offer another method of characterizing extrasolar planets and their near space environments - a method which is not limited to transiting planets. UV aurorae are atmospheric emissions produced directly by excited species in the planet's upper atmosphere. Atmospheric atoms and molecules are excited directly by precipitating energetic particles resulting in the emission of auroral light [*Bhardwaj and Gladstone*, 2000a]. Detecting UV auroral emissions would indicate the presence of a planetary atmosphere. Such observations could provide basic information about EGPs' atmospheric composition, which could be used for comparative study of exoplanetary atmospheres.

### **7.2.4 UV Stellar Continuum**

The far ultraviolet (900 – 2000 Å), in particular, is a good wavelength region when considering star/planet contrast ratios because of the minimal stellar continuum in this region. At visible wavelengths (4000 – 7000 Å), direct detections of extrasolar planets are exceedingly difficult because the star can be  $10^7$  to  $10^{10}$  times more luminous than the planet in this wavelength region [*Burrows*, 2005; *Beuzit et al.*, 2006]. The majority of main sequence stars have their peak emission in the visible, but fall off according to Wien's approximation at shorter wavelengths.

This chapter uses an analytic model to predict auroral emission strengths for the known extrasolar planets in order to determine the best EGPs for future UV observations. In

section 7.3, aurora of the solar system planets are discussed (section 7.3.1), and then the sample of candidate planets and the use of Jupiter as a template is presented. In section 7.4, model parameters and assumptions are introduced. In section 7.5, the predictive model is explained. In section 7.6, observing considerations are presented with focus on the chosen wavelength range (section 7.6.1) and observing techniques (section 7.6.2). In section 7.7, the results are discussed and a list of several promising candidate planets for observation with future UV telescopes is given. Section 7.8 is a discussion of the results and remaining uncertainties.

## **7.3 Auroral Emission from EGPs**

### **7.3.1 Solar System Analogues: Jupiter as a Template**

Spectacular displays of green and red light illuminating the night sky at latitudes less than 20 degrees from the geomagnetic poles are characteristic of the aurora on Earth. While Earth's aurora is the easiest to observe (with peak emission in the visible at 5577 Å and 6300 Å for the green and red lines, respectively) and is the most extensively studied planetary aurora, it is nowhere near the brightest or most powerful aurora in the solar system – a distinction held by Jupiter [*Bhardwaj and Gladstone, 2000b*]. Since the discovery of ultraviolet auroral emissions from Jupiter during the 1979 flyby of Voyager 1, aurora have been discovered and studied on all four giant planets in our solar system (Jupiter, Saturn, Uranus, and Neptune). Recently, *Bertaux et al.* [2005] announced the discovery of aurora on Mars. Thus, in our solar system, examples of aurora are present on planets of varied mass, rotational period, and distance from the Sun.

Aurora occur at the interface between a planet's atmosphere and magnetosphere. Auroral emissions from both the terrestrial and giant planets are produced by precipitating magnetospheric particles, however, in each situation different plasma acceleration processes are involved. For the Earth, the ultimate energy source is from the solar wind, which interacts with the planet's magnetosphere. At 1 AU, the solar wind has a velocity around 450 km/s, a density of 5 ions/cm<sup>3</sup>, and a magnetic field intensity around 2-5 nT

[Kivelson and Russell, 1995]. For the outer planets, their larger size (~4–11 times) and faster rotational period (~1.5–2.5 times) contribute to stronger internal magnetic fields (~20–20000 times) and more extensive magnetospheres. Their aurora is powered largely by energy extracted from planetary rotation, with a contribution from the solar wind [Bhardwaj and Gladstone, 2000a; Bagenal, 1992; Waite et al., 2001]. Compared to the Earth, which has a magnetic dipole moment of  $7.906 \times 10^{15}$  Tesla m<sup>3</sup>, Jupiter has a magnetic dipole moment 20,000 times stronger and a magnetosphere larger than any other object in the solar system [Bagenal, 1992]. In addition to their larger magnetic moments and magnetospheres, the giant planets' plasma sources include their satellites and rings, both embedded within their magnetospheres. These factors all contribute to Jupiter's spectacular aurora, which has an implied power input of  $\sim 10^{14}$  W, 1000 times greater than the Earth's aurora. Saturn and Uranus have an implied power input of  $\sim 10^{11}$  W, and Neptune with an estimated input power of  $\sim 10^9$  W has a relatively weak aurora [Bhardwaj and Gladstone, 2000b].

Since the majority of extrasolar planets found to date are giant planets with masses comparable to the mass of Jupiter and since Jupiter's aurora is the most well studied of the solar system giant planets, we will use Jupiter as a template for the auroral generation process. While Jupiter's plasma sources include the solar wind and the Io plasma torus, in this model we are only considering stellar wind input power.

### **7.3.2 Sample of EGPs**

Forty planets from 34 different planetary systems are evaluated in this chapter. Within this sample there are seven multi-planet systems out of which two systems, 55 Cnc and Ups And, each have three giant plants while the other five systems have two giant planets. Nine transiting planets have been included in this survey. Details for the 40 planets are given in Table 7-1; stellar characteristics for the 34 planets-hosting stars are given in Table 7-2. All the planets orbit F, G, and K stars with the exception of Gliese 876 b, Gliese 876 c, and GJ 436 b which orbit M dwarfs. The distance to the stars ranges from

**Table 7-1** Values for the extrasolar planets of interest. The first five values listed (name, period, mass, semimajor axis, and eccentricity) were obtained from *Schneider* [2006], the last two parameters (magnetic dipole moment and magnetosphere radius) were calculated (see text section 7.5.1 and section 7.5.2). Maximum values for the magnetic dipole moment and magnetopause radius are given.

Planet name	Period (days)	Planet mass ( $M_{Jup}$ )	Semimajor axis (AU)	Eccentricity	Magnetic dipole moment ( $\mathcal{M}_{Jup}$ )	Magnetopause radius ( $R_{Jup}$ )
47 Uma b	1098	2.54	2.09	0.06	4.73	39.4
47 Uma c	2594	0.79	3.79	0.10	0.64	24.0
51 Peg b	4.23	0.47	0.052	0.00	0.28	5.7
55 Cnc b	14.67	0.78	0.115	0.02	0.67	8.0
55 Cnc c	43.93	0.217	0.24	0.44	0.08	4.1
55 Cnc d	4517.4	3.92	5.257	0.33	9.72	60.4
70 Vir b	116.7	7.44	0.48	0.40	28.16	43.0
Eps Eri b	2502	0.86	3.3	0.61	0.78	11.7
GJ 3021 b	133.82	3.32	0.49	0.51	7.37	10.9
GJ 436 b	2.64	0.07	0.029	0.15	0.012	1.7
Gliese 86 b	15.77	4.01	0.11	0.05	10.09	13.8
Gliese 876 b	60.94	1.935	0.209	0.03	3.01	21.6
Gliese 876 c	30.1	0.56	0.13	-	0.38	8.5
HD 114762 b	83.9	11.02	0.3	0.34	54.04	47.6
HD 128311 b	448.6	2.18	1.099	0.25	4.85	16.5
HD 128311 c	919	3.21	1.76	0.17	6.98	23.7
HD 147506 b	5.63	8.64	0.068	0.52	35.86	19.8
HD 147513 b	540	1.0	1.26	0.52	1.01	7.3
HD 160691 b	654.5	1.67	1.5	0.31	2.36	23.9
HD 160691 c	2986	3.1	4.17	0.57	6.58	40.3
HD 162020 b	8.43	13.75	0.072	0.28	78.04	30.0
HD 168443 b	58.116	7.2	0.29	0.53	26.70	28.9
HD 189733 b	2.22	1.15	0.0312	0.00	1.27	6.4
HD 192263 b	24.348	0.72	0.15	0.00	0.58	6.2
HD 209458 b	3.52	0.69	0.045	0.07	0.54	5.3
HD 217107 b	7.126	1.37	0.074	0.13	1.69	9.0
HD 217107 c	3150	2.1	4.3	0.55	3.44	35.3
HD 3651 b	62.2	0.2	0.284	0.63	0.07	3.7
HD 39091 b	2063.8	10.35	3.29	0.62	48.7	67.8
HD 80606 b	111.8	3.41	0.439	0.93	7.71	11.8
Rho CrB b	39.9	1.04	0.22	0.04	1.07	11.5
Tau Boo b	3.31	3.9	0.046	0.01	10.60	15.2
TrES-1 b	3.03	0.61	0.039	0.135	0.44	2.2
TrES-3 b	1.31	1.92	0.023	-	3.00	7.7
Ups And b	4.617	0.69	0.059	0.01	0.54	4.0
Ups And c	241.5	1.89	0.829	0.28	2.89	15.0
Ups And d	1248	3.75	2.53	0.27	9.03	32.0
WASP-2 b	2.15	0.88	0.03	-	0.81	5.5
X0-1 b	3.94	0.9	0.049	-	0.84	6.5
X0-3 b	3.19	12	-	0.2	62.3	23.7

3.5 parsecs to 33 parsecs. The selected planets range in mass from  $M_p \sin(i) = 0.2 M_{Jup}$  to  $M_p \sin(i) = 11.02 M_{Jup}$  and their semi-major axes range from 0.0423 AU for TrES-3 to 5.257 AU for 55 Cnc d. These planets are all considered giant planets - planets larger than terrestrial planets, which have a mass  $\sim 0.003 M_{Jup}$ , but less massive than brown dwarfs (the

**Table 7-2** Stars hosting extrasolar planets (Values from *Fischer and Valenti* [2005]; *Wood et al.* [2002]; *Stevens* [2005] and *Schneider* [2006]). Values calculated Eq 7.4 and 7.5(see text section 8.3.4).

Star name	Spectral type	$T_{eff}$ (K)	$\log g$ ( $\text{cm s}^{-2}$ )	Star radius ( $R_{\odot}$ )	Star distance (pc)	Log X-ray lum. ( $\text{erg s}^{-1}$ )	X-ray flux ( $\text{erg cm}^{-2} \text{s}^{-1}$ )	Mass-loss rate ( $\dot{M}_{\odot}$ )
47 Uma	G0V	5882	4.38	1.16	14.1	-	-	-
51 Peg	G2.5IVa	5786	4.45	1.11	15.4	26.80	$8.4 \times 10^3$	0.27
55 Cnc	G8V	5234	4.45	0.93	12.5	-	-	-
70 Vir	G5V	5544	4.07	1.89	18.1	27.05	$5.2 \times 10^3$	0.46
Eps Eri	K2V	5145	4.57	0.79	3.5	28.33	$5.6 \times 10^5$	17.4
GJ 3021	G6V	5580	4.56	0.82	17.6	28.94	$2.1 \times 10^6$	85.7
GJ 436	M2.5	3350	-	0.47	10.2	-	-	-
Gliese 86	K1V	5150	4.59	0.79	10.9	28.00	$2.6 \times 10^5$	7.2
Gliese 876	M4	3180	4.70	0.41	4.69	26.49	$3.0 \times 10^4$	0.16
HD 114762	F9V	5952	4.54	1.22	28	-	-	-
HD 128311	K0V	4965	4.83	0.73	16.6	28.47	$9.1 \times 10^5$	26.0
HD 147506	F8	6290	-	1.41	135	-	-	-
HD 147513	G3/G5V	5929	4.61	0.96	12.9	29.03	$1.9 \times 10^6$	104.7
HD 160691	G3IV/V	5784	4.30	1.29	15.3	27.44	$2.7 \times 10^4$	1.42
HD 162020	K2V	4688	-	0.71	31.26	-	-	-
HD 168443	G5V	5579	4.25	1.56	33	-	-	-
HD 189733	K1-K2	4954	-	0.75	19.3	-	-	-
HD 192263	K0V	4975	4.60	0.65	19.9	27.91	$3.2 \times 10^5$	6.19
HD 209458	G0V	5942	-	1.12	47	-	-	-
HD 217107	G8IV	5704	4.54	1.12	19.7	-	-	-
HD 3651	K0V	5220	4.45	0.88	11	27.21	$3.1 \times 10^4$	0.86
HD 39091	G1V	5949	4.36	1.12	18.2	27.48	$4.0 \times 10^4$	1.68
HD 80606	G5V	5572	4.44	0.90	58.4	27.44	$2.7 \times 10^4$	1.42
Rho CrB	G2V	5822	4.36	1.30	17.4	-	-	-
Tau Boo	F7V	6387	4.26	1.44	15.6	28.99	$7.7 \times 10^5$	83.4
TrES-1	K0V	-	-	0.82	157	-	-	-
TrES-3	-	-	-	0.80	325	-	-	-
Ups And	F8V	6212	4.25	1.64	13.5	28.25	$1.1 \times 10^5$	11.5
WASP-2	K1V	-	-	0.83	140	-	-	-
X0-1	G1V	-	-	0.93	200	-	-	-
X0-3	F6	-	-	-	-	-	-	-

**Table 7-3** Planetary parameters of interest for known extrasolar planets.

Planetary parameter	Symbol	Comment
Semi-major axis	$a$	Known for all planets
Orbital period	$P_{orb}$	Known for all planets
Eccentricity	$e$	Known for most planets, if unknown an eccentricity of 0 was used
Projected mass	$M_p \sin(i)$	Known for all planets
Angle of inclination	$i$	Known only for the 9 known transiting planets, value varied between 20 – 70 degrees
Planetary mass	$M_p$	Known only for the 9 known transiting planets
Planetary radius	$R_p$	Known only for transiting planets, assumed $\sim M_p^{0.33}$ for Jupiter-like planets
Core radius	$R_c$	Unknown, assumed $\sim M_p^{0.44}$ [Farrell et al., 1999]
Density	$\rho$	Unknown, assumed Jupiter-like
Thermal conductivity	$\sigma$	Unknown, assumed Jupiter-like
Rotational period	$\omega$	Unknown, assumed $\omega \sim P_{orb}$ for planets with $a < 0.1$ AU and $e < 0.2$ , otherwise $\omega = \omega_{Jup}$

lower mass limit for a brown dwarf is taken to be  $14 M_{Jup}$  for the purposes of this study). We are considering planets which could be Jupiter-like and since Jupiter's atmosphere is 87% molecular hydrogen [dePater and Lissauer, 2001], the sample has been limited to bodies that do not have atmospheric temperatures above 3000 K - the temperature at which 9% of  $H_2$  would be dissociated. For a Sun-like G2 star this would translate into a star/planet distance of 0.01 AU, and for an F5 star (hotter than any of the selected host stars) this would be a distance of 0.013 AU. Thus, all candidate planets are far enough away from their host star to maintain an atmosphere of at least 91%  $H_2$ .

## **7.4 Parameters and Assumptions**

The calculation of the auroral brightness of a planet requires the use of many planetary and stellar parameters, both known and unknown. These parameters are listed in Table 7-3 and Table 7-4 along with the assumptions used for unknown parameters.

### **7.4.1 Known Planetary Parameters**

As mentioned above, for all planets radial velocity measurements can be used to determine the semi-major axis  $a$ , the orbital period  $P_{orb}$ , and the projected mass  $M_p \sin(i)$ . When a planet transits its star, the angle of inclination  $i$ , the actual planetary mass  $M_p$  and the planetary radius  $R_p$  can also be obtained. For planets where  $i$ ,  $M_p$ , and  $R_p$  were not known, the inclination was varied between 20-70 degrees, and the planetary radius was assumed to be  $R_p \sim M_p^{0.33}$ , as described in section 7.4.2.1.

### **7.4.2 Unknown Planetary Parameters**

The core radius  $R_c$ , rotational period  $\omega$ , density  $\rho$ , and thermal conductivity  $\sigma$ , are unknown for all extrasolar planets (to some extent these values are still uncertain for many of the giant planets in our solar system). These four parameters are important in estimating the strength of a potential planetary magnetic field (see Table 7-3). For the purposes of this

model, the planetary magnetic field is assumed to be produced by an intrinsic source characterized by a magnetic dipole moment (see section 7.5.1).

#### 7.4.2.1 Planet and Core Radius

For determining the radius of a Jupiter-like planet this study follows *Farrell et al.* [1999] and uses the approximation

$$R_p \propto M_p^{1/3} \quad (7.1)$$

with the core radius  $R_c$ , for an evolved planet assumed to be

$$R_c \propto M_p^{0.44}. \quad (7.2)$$

The core radius is used in calculating the magnetic dipole moment in the *Busse* [1976]; *Stevenson* [1983]; *Mizutani et al.* [1992]; and *Sano* [1993] relationships (Table 7-5).

#### 7.4.2.2 Rotational Period

Another unknown parameter of importance is the rotation period  $\omega$ . Here we assumed either a rotation period of 0.4 days, similar to that of the giant planets in our solar system, or we assumed the planet to be tidally locked, in which case  $\omega \sim P_{orb}$ . The potential for tidal dissipation is significant since many of the known extrasolar planets orbit very close to their parent star, allowing tidal interactions to influence the spin and orbital properties of the planet [*Rasio et al.*, 1996; *Ogilvie and Lin*, 2004; *Faber et al.*, 2005]. The mechanisms and consequences of tidal dissipation in exoplanetary systems remain imperfectly understood; several factors influence synchronization timescales including the orbital distance, eccentricity, and mass of the involved bodies. Multi-planetary systems further complicate the situation. In this model a planet was assumed to be tidally locked when it orbited closer than 0.2 AU from its star and had an eccentricity of less than 0.2. Planets with either a semi-major axis greater than 0.2 AU or an eccentricity greater than 0.2 were assumed to have Jupiter-like rotation periods of 0.4 days.

### **7.4.2.3 Density, Thermal Conductivity, and Atmospheric Composition**

For the purposes of this study, we consider only Jovian-like planets, and thus we have assumed a density  $\rho$  and conductivity  $\sigma$  similar to that of Jupiter. The model also assumes a planet whose major atmospheric constituents are atomic and molecular hydrogen, similar to the atmosphere of Jupiter, which is comprised of 86% H<sub>2</sub>, 13% He, and < 1% of H<sub>2</sub>O, CH<sub>4</sub>, NH<sub>3</sub>, and H<sub>2</sub>S in terms of percentage abundances by number of molecules for the planet's atmosphere below the clouds [Beatty *et al.*, 1999].

### **7.4.3 Known Stellar Parameters**

Since aurora are produced via star-planet interactions, it is important to consider the stellar parameters (shown in Table 7-4) in addition to the planetary parameters when calculating the expected auroral emissions from extrasolar planets. Known stellar parameters include spectral type, stellar distance  $D_s$ , mass  $M_*$ , and radius  $R_*$ . Parameters known for select stars include the metallicity  $Z$  (potentially important for planet formation) and X-ray luminosity  $L_x$ , which is useful for determining stellar mass-loss rates, a proxy for stellar wind density.

### **7.4.4 Unknown Stellar Parameters**

The most important unknown stellar parameters when calculating expected planetary auroral emission are the stellar wind density and velocity. In our solar system, the solar wind interacts with a planet's magnetic field and deposits energy into the planet's magnetosphere. Estimating the intensity of the stellar wind is thus essential in predicting auroral emission strengths.

#### **7.4.4.1 Stellar Wind**

The majority of extrasolar planets found to date are in close orbit around G - M type main-sequence stars. For our Sun, a fairly typical main-sequence G class star, the extreme temperature and density of the solar corona result in hydrodynamic expansion of the outer

corona into interplanetary space [*Parker, 1958*]. This expanding magnetized plasma represents an outward streaming of matter from the Sun, i.e. the solar wind. Since the Sun is a typical main-sequence star, it is expected that all similar cool main-sequence stars with hot coronae will possess stellar winds [*Parker, 1960*].

While it can be surmised that most stars possess stellar winds, observing and measuring these winds can be quite complicated due to the high temperature and low density of the plasma. The high temperature and ionization of the plasma make imaging and spectroscopic techniques insufficient for detecting stellar winds. Low mass-loss rates can result in densities that are undetectable using remote techniques. Even for the Sun, there are significant challenges associated with making remote observations of the solar wind; spacecraft are often required to make in situ measurements to obtain information about the coronally-driven wind in our solar system [*Woo, 1977*].

Of all the spectral types, low-mass stars like the Sun have proven to be the most difficult stellar type for which to remotely observe the stellar winds. Stars hotter than solar-type, such as massive O and B type stars, have powerful winds that are comparatively easy to detect spectroscopically using the P Cygni line profiles [*Owocki, 1990*]. Estimates of stellar mass-loss rates can also be obtained for Wolf-Rayet stars, cool red giants, and supergiants; however, stellar winds of late-type main-sequence stars, such as the Sun, have been notoriously difficult to measure [*Bradford and Drake, 2001*].

An observational method using known parameters, such as age, rotation rate, activity level, and X-ray luminosity is necessary in order to estimate wind conditions remotely. From such parameters, insight into the expected stellar winds emitted by exoplanet host stars can be obtained. Knowledge of stellar winds allows a more complete understanding of the physical interactions likely to occur in these distant planetary systems: the size of the planet's magnetosphere and brightness of the planet's auroral emissions.

#### 7.4.4.2 X-Ray Emission and Mass-Loss Rates

Since stellar winds originate in the coronae of stars, it seems reasonable to associate stellar mass-loss rates with coronal activity. All stars seemingly support active regions, which include spots, flares, and prominences, that result from the activity of underlying magnetic fields. For lower mass stars, such as the Sun, the heat and energy of the corona causes the emission of X-rays. During periods of high magnetic activity, increases in the stellar activity cycle are reflected in the star's X-ray luminosity [Favata *et al.*, 2004]. Magnetic activity can be measured as a function of the flux of X-rays; this makes the coronal X-ray surface flux a good indicator of the magnetic activity level of a star.

Wood *et al.* [2002] derived a scaling relation that correlates mass-loss rates ( $\dot{M}_*$ ) with X-ray flux ( $F_x$ )

$$\dot{M}_* \propto F_x^{1.15 \pm 0.20} \quad (7.3)$$

with the X-ray flux computed from the X-ray luminosity via the equation

$$F_x = \frac{L_x}{4\pi R_*^2} \quad (7.4)$$

where  $L_x$  is the X-ray luminosity, and  $R_*$  is the radius of the star. This relationship provides an observable proxy for estimating stellar wind density.

#### 7.4.4.3 Estimating Stellar Wind Parameters

Applying the relationships discussed above to estimate the stellar winds expected for planet-hosting stars, we first parameterize mass-loss rates to estimate the total mass leaving the star [Stevens, 2005].

$$\frac{\dot{M}_*}{\dot{M}_\odot} = \left(\frac{R_*}{R_\odot}\right)^2 \left(\frac{F_x}{F_{x,\odot}}\right)^{1.15 \pm 0.02} \quad (7.5)$$

where  $\dot{M}_*$  is the total mass-loss rate from the planet-hosting star,  $\dot{M}_\odot$  is the mass-loss rate from the Sun ( $2 \times 10^{-14} M_\odot \text{ yr}^{-1}$ ),  $R_*$  is the radius of the star,  $R_\odot$  is the radius of the Sun ( $7 \times 10^5 \text{ km}$ ), and  $F_{x,\odot}$  is the X-ray surface flux from the Sun ( $3.1 \times 10^4$ ) [Stevens, 2005].

Relevant stellar parameters are provided in Table 7-2 for selected stars known to host extrasolar planets. The spectral type, stellar distance, mass, and radius are taken from *Espresate* [2005]. Values for the X-ray luminosities were obtained using the NEXXUS database, a database of nearby X-ray and extreme ultraviolet emitting stars. NEXXUS catalogues all known stars that are identified as X-ray and extreme UV sources from ROSAT data, and are within a distance of 25 parsecs of the Sun [Schmitt and Liefke, 2004]. For stars where the X-ray luminosities are unknown and the stellar mass-loss rates cannot be computed, a value of 1.0 was used for the following calculations.

In this predictive model, the density of the stellar wind was assumed to be proportional to the mass-loss rate, and stellar wind velocity, temperature, and magnetic field strength were assumed to be solar-like, a justified approximation given that the majority of stars in the sample are within half a solar mass of the Sun.

**Table 7-4** Stellar parameters of interest for stars known to host extrasolar planets. Solar wind values for  $v_{sw}$ ,  $T_{sw}$ , and  $B_{sw}$  obtained from *Kivelson and Russell* [1995].

Stellar parameter	Symbol	Comment
Spectral type	-	Known for all planet-hosting stars
Stellar distance	$D_s$	Known for all planet-hosting stars
Stellar mass	$M_*$	Known for most stars, no value assumed
Stellar radius	$R_*$	Known for most stars, no value assumed
Metallicity	$Z$	Known for many stars, thought to be important for planet formation
Stellar age	$t$	Difficult to determine for main sequence stars; known for very young and old stars
X-ray luminosity	$L_x$	Known for select stars (see NEXXUS database)
X-ray flux	$F_x$	Can be calculated from X-ray luminosity (Eq 8.4)
Stellar wind density	$n_{sw}$	Unknown, assumed to be proportional to mass-loss rate scaled with orbital distance
Stellar wind velocity	$v_{sw}$	Unknown, assumed to be solar-like, $v_{sw} = 4.5 \times 10^5 \text{ m/s}$
Stellar wind temperature	$T_{sw}$	Unknown, assumed to be solar-like, $T_{sw} = 4.0 \times 10^4 \text{ K}$
Stellar wind magnetic field	$B_{sw}$	Unknown, assumed to be solar-like, $B_{sw} = 5 \times 10^{-9} \text{ T}$

## 7.5 Predictive Model

The physical process through which aurora are created is complex, and even within our solar system the conditions giving rise to auroral emissions vary substantially from planet to planet. The problem of predicting expected auroral signal strengths is further complicated in the case of extrasolar planets for which little information is known.

Aurora are electromagnetic emissions emanating from the high-latitude regions of a planet (see section 7.3). They result from the energy flux of the stellar wind deposited in a planetary magnetosphere and the release of that energy through dissipation processes [Bhardwaj and Gladstone, 2000b]. In order to estimate the amount of energy produced by the star-planet interaction, an approximate value for the size of the magnetosphere is needed. To calculate the magnetospheric radius, a pressure balance between the stellar wind and the planetary magnetic field is used (Eq 7.6). Below is a systematic look at the steps used in this predictive model to estimate the auroral emission strength from known exoplanets.

### 7.5.1 Planetary Magnetic Dipole Moment

The planetary dipole moment  $\mathcal{M}$  is important for determining the planetary magnetic pressure  $B_p^2/2\mu_0$ , which in turn influences the location of the magnetopause and the amount of stellar energy the planet accumulates. This is an elusive quantity; even in our own solar system magnetic dipole moments remain poorly understood [Stevenson, 2003]. Several papers including Busse [1976]; Stevenson [1983]; Mizutani *et al.* [1992]; Sano [1993]; Cain *et al.* [1995]; Farrell *et al.* [1999] and Stevens [2005] have explored a relationship between magnetic dipole moments and other planetary parameters searching for scaling relations to explain the magnetic fields observed in our solar system. Scaling laws from five of these papers are listed in Table 7-5. These relationships were used to plot the expected magnetic moment for planets in our solar system (Figure 7.1). For Saturn and Uranus, all five relationships overestimate the magnetic dipole moment (the actual value is represented by a \*), but for the other four planets, a few of the scaling laws come close.

**Table 7-5** Scaling laws for calculating planetary magnetic dipole moment  $\mathcal{M}$  and the subscript  $c$  denotes values for the planet's core (Adapted from *Grieffmeier et al. [2004]*).

Scaling Relation	Reference
$\mathcal{M} \propto \rho_c^{1/2} \omega r_c^4$	<i>Busse, 1976</i>
$\mathcal{M} \propto \rho_c^{1/2} \omega^{1/2} r_c^3 \sigma^{-1/2}$	<i>Stevenson, 1983</i>
$\mathcal{M} \propto \rho_c^{1/2} \omega^{3/4} r_c^{7/2} \sigma^{-1/4}$	<i>Mizutani et al., 1992</i>
$\mathcal{M} \propto \rho_c^{1/2} \omega r_c^{7/2}$	<i>Sano, 1993</i>
$\mathcal{M} \propto M_p^{1.66}$	<i>Stevens, 2005</i>

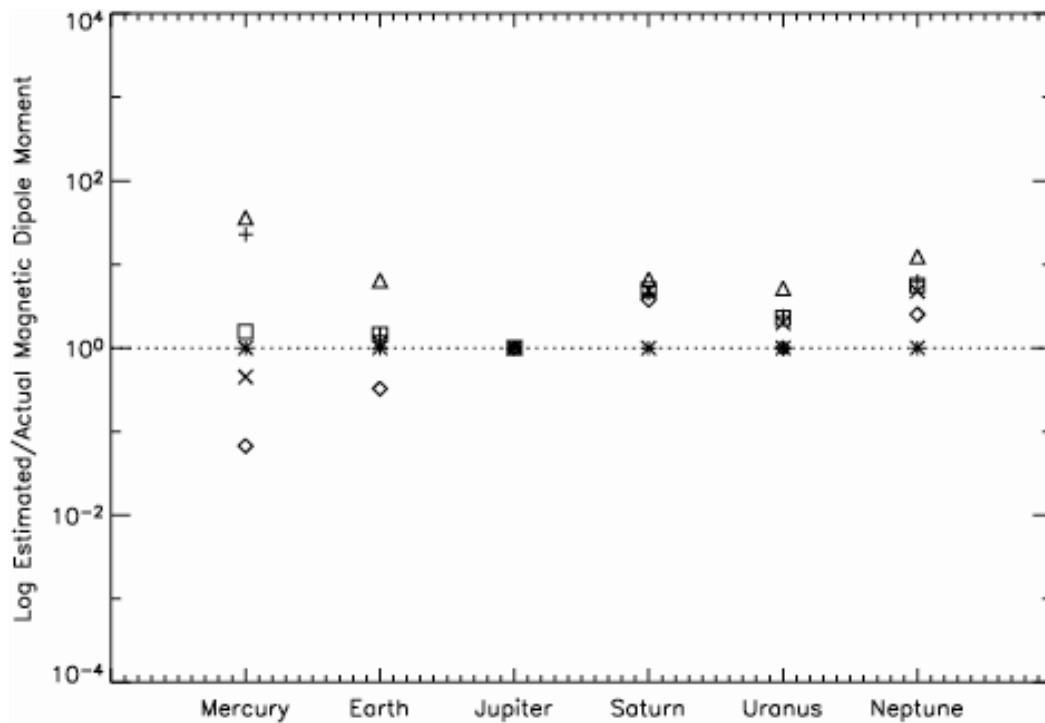


**Figure 7.1** The planetary magnetic moment for 6 bodies in our solar system calculated using the scaling relations listed in Table 7-3. The \* represents the actual planetary magnetic moment. The diamonds represent the Busse relationship; the triangles represent the Stevenson relationship; the squares represent the Mizutani relationship; the X represents the Sano relationship; the + represents the Stevens relationship.

For the purposes of this model, the planetary magnetic dipole moment was calculated using all five different scaling relations. The highest and lowest values computed using these relationships were used for the maximum and minimum values expected for the magnetic dipole moment, providing a range of possible magnetic moments. The potential for a brighter aurora may depend on the strength of the magnetic dipole moment, however, there is still ambiguity surrounding the generation of planetary magnetic fields and the many factors that may influence the strength of the dipole moment, such as rotation rate and core radius.

### 7.5.2 Magnetopause Distance

To calculate the magnetospheric radius  $R_{mp}$ , a pressure balance between the stellar wind and the planetary magnetic field is used:

$$[p_{ram} + p_B + p_{KE}]_{sw} = \frac{B_p^2}{2\mu_o} \quad (7.6)$$

Where  $p_{ram}$ ,  $p_B$ , and  $p_{KE}$  are the stellar wind ram pressure, magnetic pressure, and kinetic pressure, respectively. These are balanced by the planetary magnetic pressure and the magnetospheric particle pressure and flow. However the magnetospheric particle pressure and flow are small compared to the magnetic pressure and can thus be neglected. The planetary magnetic pressure is generated by the planetary magnetic field  $B_p$ , which at the in the equatorial plane is defined as

$$B_p(r) = \frac{\mathcal{M}}{r^3} \quad (7.7)$$

Equations 7.6 and 7.7 can be used to determine the standoff distance of the magnetopause

$$R_{mp} = \left[ \frac{\mathcal{M}^2}{2\mu(p_{ram} + p_B + p_{KE})_{sw}} \right]^{1/6} \quad (7.8)$$

where  $\mathcal{M}$  is the range of values obtained above (section 7.5.1),  $\mu_o$  is the magnetic permeability of free space, and

$$p_{ram} = \rho v^2, \quad (7.9)$$

$$p_{B,sw} = \frac{B^2}{2\mu_o}, \quad (7.10)$$

$$p_{KE,sw} = nk(T_p + T_e). \quad (7.11)$$

These three stellar wind quantities are found assuming solar values for  $v$ ,  $B$ , and  $T$  (Table 7-4). The density of the stellar wind at the location of the exoplanet is found by taking the solar wind density at 1 AU ( $10^3 \text{ cm}^3$ ) dividing that by the square root of star-planet separation distance  $d$ , and then multiplying by stellar mass-loss rate  $\dot{M}$ .

### 7.5.3 Stellar Wind Power

The brightness of the aurora is a diagnostic of the energy input to the atmosphere and of magnetospheric processes. Here we disregard the contribution of planetary rotational energy and additional plasma sources from satellites and rings, and we only consider the energy input from the stellar wind. To estimate the power delivered to the planet by the stellar wind, the magnetospheric cross section  $\pi R_{mp}^2$  was multiplied by the mass density of the stellar wind  $\rho$ , and the stellar wind velocity cubed

$$P_{sw} = \rho v^3 \pi R_{mp}^2 \quad (7.12)$$

The predicted stellar wind power received by selected EGPs compared to the stellar wind power received by Jupiter is given in Table 7-6. For Jupiter, a value of  $P_{sw} = 10^{14} \text{ W}$  is used.

**Table 7-6** Predicted stellar wind power for selected EGPs are compared to the solar wind power at Jupiter. \* signifies a transiting planet.

Planet name	Planet mass $\left(\frac{M_p}{M_{Jup}}\right)$	Semi-major axis $\left(\frac{a}{a_{Jup}}\right)$	Stellar wind power $\left(\frac{P_{sw}}{P_{sw,Jup}}\right)$	
			Lower limit	Upper limit
Jupiter	1.00	1.00	1.00	1.00
47 Uma b	2.55	0.40	8.21	10.69
47 Uma c	0.76	0.72	1.27	1.34
51 Peg b	0.47	0.01	16.60	80.56
55 Cnc b	0.79	0.02	11.33	121.65
55 Cnc c	0.22	0.05	21.91	33.17
55 Cnc d	3.93	1.01	3.26	7.12
70 Vir b	7.47	0.09	99.18	250.34
Epsilon Eri b	0.86	0.63	35.72	36.54
GJ 3021 b	3.33	0.09	2000.41	4205.45
GJ 436 b*	0.07	0.01	4.76	19.18
Gl 86 b	4.03	0.02	136.33	3038.18
Gliese 876 b	1.94	0.04	39.60	47.60
Gliese 876 c	0.56	0.03	31.30	35.86
HD 114762 b	11.06	0.06	222.75	614.63
HD 128311 b	2.59	0.20	283.45	370.69
HD 128311 c	3.22	0.34	80.00	166.91
HD 147506 b*	8.64	0.01	3442.64	8981.78
HD 147513 b	1.00	0.24	384.93	385.02
HD 160691 b	1.68	0.29	16.94	19.50
HD 160691 c	3.11	0.80	8.46	17.51
HD 162020 b*	13.80	0.01	2796.89	8114.47
HD 168443 b	7.23	0.06	437.33	1095.74
HD 189733 b*	1.15	0.01	339.20	1029.48
HD 192263 b	0.72	0.03	16.84	255.05
HD 209458 b*	0.69	0.01	94.32	394.95
HD 217107 b	1.38	0.01	71.06	476.21
HD 217107 c	2.11	0.83	7.08	8.72
HD 3651 b	0.20	0.05	25.00	38.76
HD 39091 b	10.39	0.63	44.35	120.64
HD 80606 b	3.42	0.08	1565.69	3311.56
rho CrB b	1.04	0.04	73.58	73.80
Tau Boo b	4.15	0.01	290.43	2292.68
TrES-1*	0.61	0.01	2270.31	8666.71
TrES-3*	1.94	0.00	1264.95	2811.27
Ups And b	0.69	0.01	258.69	1296.63
Ups And c	1.90	0.16	158.89	189.66
Ups And d	3.76	0.49	38.94	84.15

### 7.5.4 Auroral Brightness

The aurora is an inherently dynamic phenomenon which changes over short and long timescales. For the purposes of computing the surface brightness of the aurora  $\Sigma$ , we consider the case of a static aurora during a stellar quiet period. (The aurora could be orders of magnitude larger during active periods.) The computation of the surface

brightness depends on an assumed efficiency  $e$  for the conversion of stellar wind power into UV auroral emission

$$\Sigma \propto \frac{P_{sw} e}{\pi R_p^2} \quad (7.13)$$

where  $P_{sw}$  is the power delivered to the planet by the stellar wind,  $e$  is the assumed efficiency (energy received compared to the auroral output), and  $R_p$  is assumed to be  $\sim M_p^{0.33}$  for all non-transiting planets.

The efficiency of energy conversion into UV auroral brightness is an unconstrained parameter. In our solar system efficiencies vary greatly, thus making it difficult to determine what value to use for the efficiency. Jupiter's apparently high efficiency (>100%) is due in large part to the presence of the Io plasma torus and additional plasma sources beyond the solar wind contribution [Bhardwaj and Gladstone, 2000b]. In this model we do not consider the effects of satellites or rings, which would increase the efficiency of the system. In this study, a value of 10% is chosen for the efficiency.

### 7.5.5 Integrated Flux

The auroral flux (in  $ergs\ cm^{-2}\ s^{-1}$ ) emitted by the planet is then scaled for stellar distance to represent the flux received at Earth

$$F = \frac{P_{sw} e}{4\pi D_s^2} \quad (7.14)$$

where  $D_s$  is the distance the host star is from Earth and  $e$  is the efficiency which set to 10% for these calculations. The auroral fluxes for the EGPs in this survey are listed in Table 7-7 and Table 7-8 for the Werner and Lyman wavelength bands, respectively (see section 7.6.1). Using the auroral flux the number of photons collected by a given telescope can

then be computed for a specified exposure time and collecting area. Possible UV instruments for observation are discussed in section 7.6.2.

### **7.5.6 Contrast Ratio**

In order to gauge the potential observability of a EGP's aurora, we need to determine the contrast between the signal from the planet and the signal from the host star at UV wavelengths. The contrast ratio necessary to identify a planet depends on the instrument being used for the observation and the observing time (see section 7.7.1). When determining the stellar flux in the UV, models such as the *Allard et al.* [2000] and *Kurucz* [1993] stellar atmosphere models produce results that can be orders of magnitude too low. Instead, we use Tom Ayres' CoolCAT site, an HST STIS Echelle Spectral Catalog of late-type stars. Spectra of stars with similar spectral types were used and then scaled for stellar distance. The spectra were integrated over the Werner and Lyman bands to obtain the stellar flux in each of these regions. Results for all 34 planet-hosting stars are given in column 4 of Table 7-7 and Table 7-8.

## **7.6 Observing Auroral Emissions**

Auroral emissions cover a wide range of the electromagnetic spectrum and have also been observed at X-ray, UV, near-IR, far-IR, and radio wavelengths [*Bhardwaj and Gladstone, 2000a; Livengood et al., 1992*]. UV, visible, and IR aurorae are atmospheric emissions produced when ambient atmospheric species are excited by the precipitating species directly (UV emission) or indirectly (IR emission), while radio and X-ray aurorae are beam emissions produced by the precipitating particles themselves [*Bhardwaj and Gladstone, 2000a; Bhardwaj and Gladstone, 2000b*]. Auroral emissions at different wavelengths provide a different set of information, and thus it is valuable to search for auroral emissions over a range of wavelengths.

Searches for radio aurora have been pursued by *Winglee et al.* [1986] and *Bastian et al.* [2000] using the Very Large Array (VLA) to observe nearby stars at 333 and 1465 MHz

(and a few at 74 MHz in the case of *Bastian et al.* [2000]). *Farrell et al.* [1999; 2003] observed Tau Boo with the VLA at 74 MHz and quoted an upper flux limit of 0.12 Jy, and *Butler* [2003] explores the prospect of detecting EGP radio emissions using future instruments such as the Square Kilometer Array (SKA) or the Low-Frequency Array (LOFAR). There have also been detections of EGPs in the IR [*Beichman et al.*, 2005; *Deming et al.*, 2005, 2000].

Here we present a case for searching for ultraviolet auroral emissions. The ultraviolet is an ideal range in which to search for extrasolar auroral emissions because i) the gas giant planets in our solar system all emit intense aurora in the ultraviolet [*Bhardwaj and Gladstone*, 2000a], ii) there is only weak stellar continuum to compete with the signal from the planet in this region, and iii) the two signals can be separated by the Doppler effect.

### 7.6.1 UV Auroral Emissions

Intense ultraviolet auroral emissions have been detected and observed on Jupiter by the UV spectrometer on Voyager [*Broadfoot et al.*, 1979], by the International Ultraviolet Explorer (IUE) [*Clarke et al.*, 1980; *Livengood and Moos*, 1990; *Harris et al.*, 1996], and by the Hubble Space Telescope (HST) [*Gérard et al.*, 1993; *Clarke et al.*, 1994; *Prangé et al.*, 1998].

The bulk of Jupiter's UV auroral emissions come from atomic and molecular hydrogen [*Prangé*, 1992]. The atmospheric composition of the giant planets is close to solar, with H species and He far more abundant than C, N, or O [*Bhardwaj and Gladstone*, 2000b]. In the case of atomic hydrogen, the strongest emission line is the Ly- $\alpha$  line at 1216 Å. For molecular hydrogen, H<sub>2</sub>, the prominent emission lines are observed in the Werner ( $C^1\Pi_u \rightarrow X^1\Sigma_g^+$ ; 1230 - 1300 Å) and Lyman ( $B^1\Sigma_u^+ \rightarrow X^1\Sigma_g^+$ ; 1550 - 1620 Å) bands. These auroral emissions result from inelastic collisions between primary and secondary electrons with the ambient H<sub>2</sub> ground state [*Gustin et al.*, 2004]. The color ratio between the fluxes

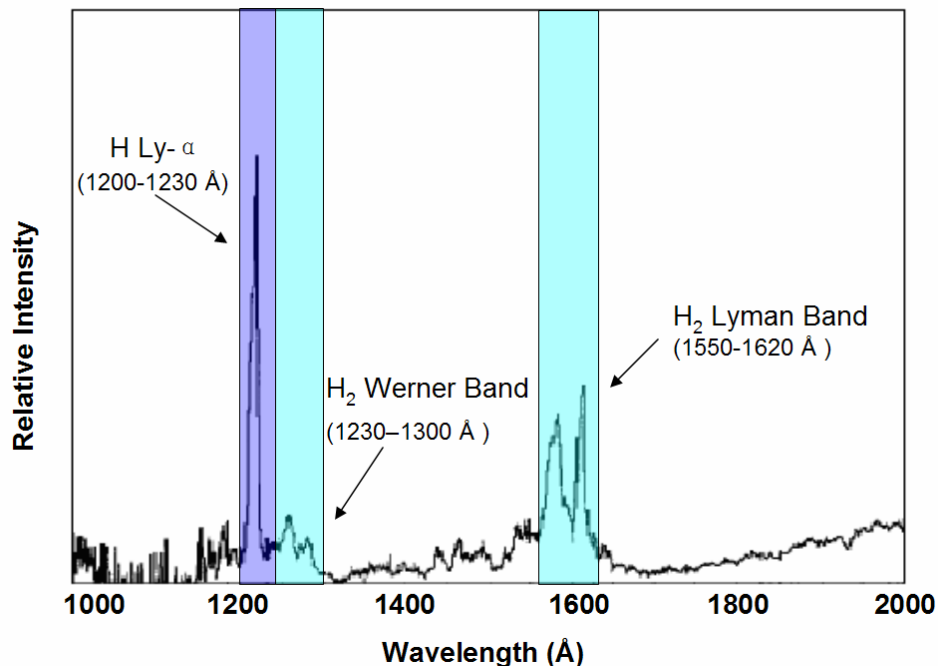


**Figure 7.2** Spectrum of Jupiter's aurora in the UV taken with the International Ultraviolet Explorer (IUE) on 20 December 1990. Blue regions mark bandpasses of  $\text{H}_2$  auroral emission. Left band pass ranges from 1230 to 1300 Å and features results primarily from  $\text{H}_2$  Werner band emissions. The band pass on the right ranges from 1550 to 1620 Å and contains primarily Lyman band features. The purple region marks the the  $\text{H Ly-}\alpha$  emission line, the prominent spike at 1216 Å, which has both auroral and stellar contributions. (Image adapted from *Harris et al.* [1996])

escaping in these two wavelength regions can be used as a qualitative measure of the  $\text{H}_2$  absorption by methane  $\text{CH}_4$  layers in the atmosphere [*Rego et al.*, 1999].

In this short-wavelength region, G, K, and M stars emit mostly at discrete wavelengths corresponding to atomic transitions for species such as H, C, and O. Assuming a Jupiter-like planet whose major atmospheric constituents are atomic and molecular hydrogen, we would expect significant auroral emission in the Lyman and Werner bands (Figure 7.2). Since molecular hydrogen is not found in most stellar spectra, the auroral  $\text{H}_2$  emissions could stand out against the spectrum of the host star depending on the strength and composition of the continuum radiation of the host star.

In order to improve a weak signal, spectral lines can be added together into distinct wavelength bands. In the case of the H<sub>2</sub> Werner and Lyman bands, the two brightest bandpasses are considered: one combining photons with wavelengths from 1230 to 1300 Å (the Werner band), and one combining wavelengths from 1550 to 1620 Å (the Lyman band; see Figure 7.2). From models of electron impact UV emission spectrum of molecular hydrogen, it is calculated that 10% of the total H<sub>2</sub> emission is located in the 1230 to 1300 Å wavelength band, and 11% of the total emission is in the 1550 to 1620 Å bandpass [Liu *et al.*, 1995; 1998]. While the H Ly- $\alpha$  emission at 1216 Å is very strong (Figure 7.2), stars also have strong emissions at this wavelength and so for the purposes of detecting planetary auroral signatures, we focus on the two molecular hydrogen bands which are not found in most stellar spectra.

### **7.6.2 Current and Future UV Instruments**

Ultraviolet radiation ranges from approximately 200 to 4000 Å with the UV bandpass divided into four subdivisions: near-UV (NUV; 3000-4000 Å), mid-UV (MUV; 2000-3000 Å), far-UV (FUV; 900-2000 Å), and extreme-UV (EUV; ~200-900 Å). All MUV, FUV, and EUV observations must be made from space due to the significant opacity from atmospheric ozone absorption at wavelengths below ~3000 Å [Stern, 1999]. Observations of the H<sub>2</sub> Lyman and Werner bands, both in the FUV, must therefore be obtained using space-based instruments. Two major space telescopes to view the near- and far-UV spectrum of the sky are the Far Ultraviolet Spectroscopic Explorer (FUSE) and the Hubble Space Telescope (HST). FUSE, launched in 1999 as part of NASA's Origins project, is a general purpose Earth orbiting observatory with high-resolution ( $\lambda/\Delta\lambda = 24,000-30,000$ ) spectroscopic capabilities [Moos *et al.*, 1997]. The FUSE instrument has an effective area of 20-80 cm<sup>2</sup> and 1.5 arcsecond angular resolution. The spectroscopic capabilities of FUSE cover the wavelength region between 905 Å and 1195 Å, just below the region of interest (1200 - 1700 Å) for observing EGPs aurora in the Lyman and Werner bands. The other space-based telescope with ultraviolet capabilities is HST, whose past and present UV instruments are described below.

### 7.6.2.1 *Space Telescope Imaging Spectrograph (STIS)*

STIS is a spectrograph which was installed on HST in 1997 with observing capabilities ranging from the near-IR through the FUV [Baum, 1997]. Of the three detectors installed on STIS, the MAMA (Multi-Anode Microchannel Array) detectors are used in the UV. The STIS/FUV-MAMA operates in the UV from 1150-1700 Å covering a  $25 \times 25$  arcseconds field of view (FOV), with 0.024 arcsecond pixels, negligible read noise, and dark current of  $7 \times 10^{-6}$  counts/pixel/sec. STIS has two spectroscopic modes capable of observing in the region of interest: the G140L and G140M gratings. The G140L covers the wavelength region from 1150-1730 Å with a central wavelength at 1425 Å, an average dispersion of 0.6 Å/pixel, and a plate scale of 0.025 arcsec/pixel. The throughput for the Werner band is 3.4% and the throughput for the Lyman band is ~1% [Kim *et al.*, 2003]. The power system of STIS, which failed in August of 2004, was repaired in 2009 by space shuttle astronauts during Servicing Mission 4 (SM4).

### 7.6.2.2 *Advanced Camera for Surveys (ACS)*

The Advanced Camera for Surveys, launched in 2002, is a third generation axial instrument aboard HST. ACS has three independent, high-resolution channels covering the ultraviolet through the near-IR regions of the spectrum, a large detector area and quantum efficiency, and coronagraphic, polarimetric and grism capabilities.

The Solar Blind Channel (SBC), is optimized for UV observations from 1150 - 1700 Å over a  $29 \times 26$  arcsecond FOV. This channel has a plate scale of  $\sim 0.032$  arcseconds/pixel and a peak efficiency of 7.5%. ACS also provides low resolution ( $\lambda/\Delta\lambda \sim 100$  at 1500 Å) FUV prism spectroscopy in the SBC from 1250 Å to 1800 Å [Gonzaga *et al.*, 2005]. Using the LiF<sub>2</sub> prism (PR110L), the throughput for the Werner and Lyman bands ranges from 4.6% to 1.8% (see Figure 7.3). The SBC is currently operating using only side 1 of two redundant set of electronics [Walsh, 2006].

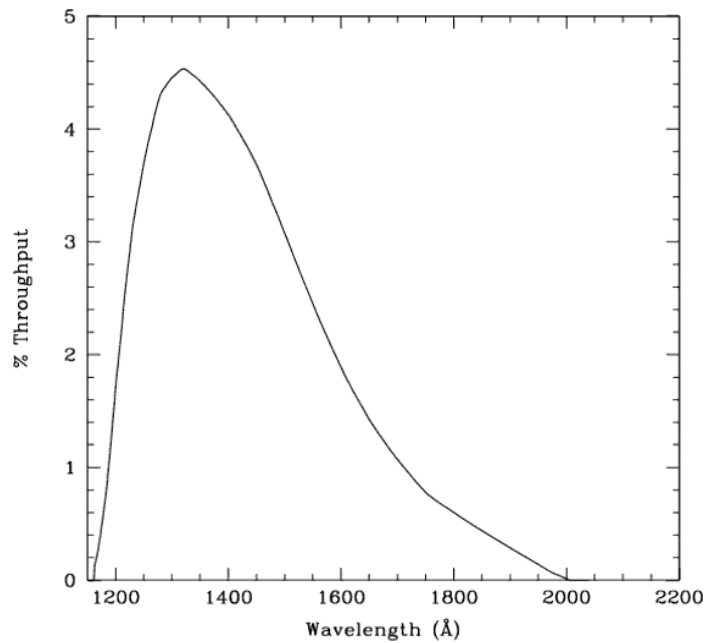


**Figure 7.3** Integrated system throughput for SBC/PR110LP from the ACS Instrument Handbook for Cycle 15 (From *Gonzaga et al.* [2005]).

### 7.6.2.3 *Cosmic Origins Spectrograph (COS)*

HST's Cosmic Origins Spectrograph, an ultraviolet instrument designed to acquire high resolution ( $\lambda/\Delta\lambda \sim 20\text{-}30,000$ ) spectra in the FUV (900-2000 Å), was installed on HST during the 2009 servicing mission. COS achieves a  $S/N=10$  and  $\lambda/\Delta\lambda=20,000$  for flux levels of  $1\text{-}2 \times 10^{-15}$  ergs  $\text{cm}^{-2}\text{s}^{-1}\text{Å}^{-1}$  in a 10,000 second integration across much of the 900-2000 Å bandpass [*Morse et al.*, 1998]. COS is considerably more sensitive than STIS at comparable spectral resolution as shown in Figure 7.4, which plots the end-to-end systems throughputs for the FUV channel. In this channel, the peak effective area using the G130M grating is  $\sim 2700$   $\text{cm}^2$  at 1300 Å [*Sembach et al.*, 2003]. For the Werner and Lyman bands, the effective area is about  $2500$   $\text{cm}^2$  at 1200 Å and  $1000$   $\text{cm}^2$  at 1600 Å. The throughput is  $\sim 6\%$  and  $2.5\%$ , respectively. These are both slightly better than the throughputs for the ACS SBC/PR110L. A potential problem with COS is the instrument's inability to look at bright targets. COS was designed to observe far away stars, and thus care needs to be taken to ensure that the planet-hosting stars are within the instrument's brightness limits.

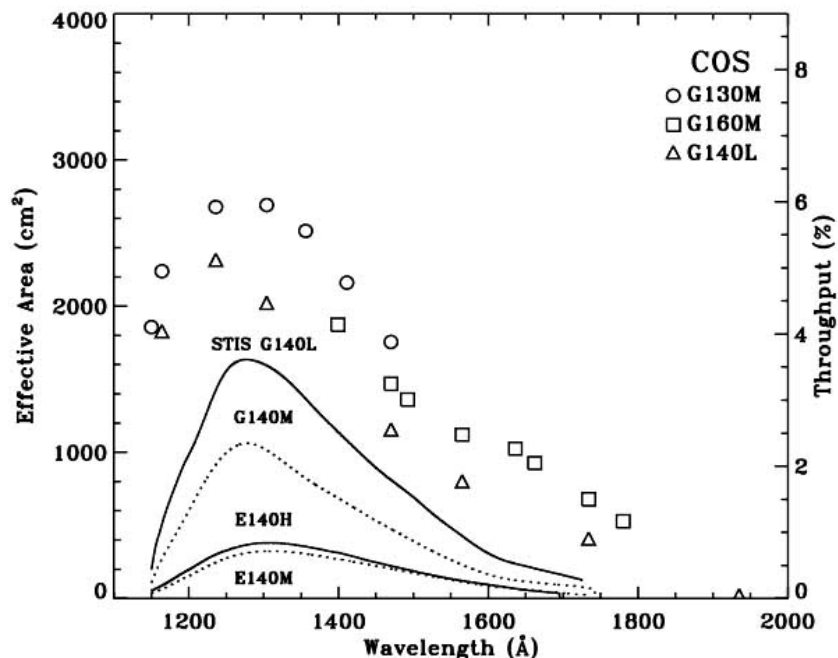


**Figure 7.4** COS FUV effective areas and throughputs (unfilled circles, squares, and triangles) compared to values for several STIS modes (dashed and dotted lines). All values are end-to-end system values. Plot from the HST/COS Instrument Mini-Handbook (from *Sembach et al.* [2003]).

## 7.7 Results

The expected auroral flux from selected EGPs, the UV flux from the host star, the ratio of the planetary to stellar flux, and the star-planet angular separation for the Werner and Lyman bands are given in Table 7-7 and Table 7-8, respectively. The UV auroral signal from the planet was divided by the signal from the host star in the corresponding wavelength band to give the planet/star contrast ratio (columns 5, 6, and 7). In the Werner band, the low stellar flux results in 15 planets with average contrast ratios of  $>10^{-3}$ . These 15 candidate planets are (in order of greatest average contrast ratio) GJ 3021 b, HD 80606 b, Gliese 86 b, HD 128311 b, HD 168443 b, HD 192263 b, HD 128311 c, HD 147513 b, Rho CrB b, HD 309091 b, HD 217107 b, Peg 51 b, 55 Cnc b, HD 3651 b, and 70 Vir b. Higher stellar flux in the Lyman band results in slightly lower contrast ratios. In this band 11 planets have an average contrast ratio of  $>10^{-3}$ , all of the same planets listed above with the exception of Rho CrB b, HD 39091, 51 Peg b, and HD 3651. In both wavelength bands the top five candidate planets are:

- (i) GJ 3021 b
- (ii) HD 80606 b
- (iii) Gliese 86 b
- (iv) HD 128311 b
- (v) HD 168443 b

In both the Werner and Lyman band regions, GJ 3021 b yields the greatest planet/star contrast ratio of  $2.81 \times 10^{-2}$  and  $2.01 \times 10^{-2}$ , respectively. Given our analysis of the expected auroral emission strengths, there are several factors that contribute to favorable contrast ratio of this system. First, GJ 3021 b is a  $3.32 M_{Jup}$  planet orbiting close to its star ( $\alpha=0.49$ ) with an eccentricity of  $e = 0.51$ . Given these parameters, the planet was not assumed tidally locked, and a rotational period of 0.4 days was used in the model. The planet's large mass and core radius ( $R_c = 1.70 R_{c,Jup}$ ), combined with its rapid rotational period, resulted in an estimated magnetic dipole moment 7.4 times the magnetic moment of Jupiter. With such a large magnetic moment and given the significant stellar mass-loss from the host-star,  $\dot{M} = 85.7 \dot{M}_{\odot}$ , this planet is predicted to generate an aurora three orders of magnitude brighter than Jupiter's. If we assume the planet is tidally locked, then the lower limit for the expected auroral flux is reduced by one order of magnitude, but the upper limit remains the same. Even assuming a tidally-locked planet, GJ 3021 b would still remain one of the top 5 most promising candidates. The host-star, GJ 3021, is of spectral type G6V, slightly cooler than solar type, and is 17.6 parsecs away.

Planet HD 80606 b has an average planet/star contrast ratio of  $2.21 \times 10^{-2}$  in the Werner band and  $2.51 \times 10^{-2}$  in the Lyman band. HD 80606 b is another large planet with  $M_p \sin(i) = 3.41 M_{Jup}$  also orbiting about half an AU from its star, but with a slightly larger eccentricity of  $e = 0.927$ . Again, a rotational period of 0.4 days was assumed. HD 80606 b has a core radius  $R_c = 1.72 R_{c,Jup}$  and an estimated magnetic dipole moment 7.7 times the magnetic moment of Jupiter. The host-star is of spectral type G5V and has a mass-loss rate similar to solar,  $\dot{M} = 1.42 \dot{M}_{\odot}$ . This planet is also predicted to generate an aurora  $10^6$  times as bright as the aurora produced by Jupiter.

The third potential candidate planet, Gliese 86 b, is assumed to be tidally-locked,  $\omega = P_{orb}$ . Even as such, this planet's predicted auroral brightness is estimated to be five orders of magnitude brighter than Jupiter's aurora. The host-star is a K1V star 10.9 parsecs from Earth with a mass-loss rate of  $7.2 \dot{M}_{\odot}$ . The planet is  $4.01 M_{Jup}$  with a semi-major axis of only 0.11 AU and an eccentricity of 0.046. This close circular orbit would likely result in tidal-locking, yet the planet is still estimated to produce intense UV auroral emission.

**Table 7-7** Results in Werner Band. The upper and lower limits for the planet flux given in columns two and three are for the total planetary auroral emissions in the Werner band (10% of the total UV auroral emission [Liu et al., 1995; 1998])

Planet name	Planet flux <sup>2</sup> (photons/cm <sup>2</sup> /sec)		Star flux (photons/cm <sup>2</sup> /sec)	Planet/star flux			Angular sep. (arcsec)
	Lower limit	Upper limit		Lower limit	Upper limit	Average	
47 Uma b	2.40E-09	3.20E-09	9.20E-05	2.61E-05	3.47E-05	3.04E-05	0.157
47 Uma c	3.73E-10	4.00E-10	9.20E-05	4.05E-06	4.35E-06	4.20E-06	0.280
51 Peg b	3.97E-09	1.97E-08	5.58E-06	7.12E-04	3.53E-03	2.12E-03	0.004
55 Cnc b	3.26E-09	3.58E-08	1.03E-05	3.17E-04	3.48E-03	1.90E-03	0.009
55 Cnc c	6.31E-09	9.77E-09	1.03E-05	6.13E-04	9.48E-04	7.80E-04	0.018
55 Cnc d	9.40E-10	2.10E-09	1.03E-05	9.13E-05	2.04E-04	1.47E-04	0.392
70 Vir b	1.06E-08	2.73E-08	1.77E-05	5.99E-04	1.54E-03	1.07E-03	0.022
Epsilon Eri b	1.80E-07	1.89E-07	3.79E-04	4.76E-04	4.98E-04	4.87E-04	1.031
GJ 3021 b	3.33E-07	7.16E-07	1.87E-05	1.78E-02	3.83E-02	2.81E-02	0.028
Gliese 86 b	5.83E-08	1.33E-06	3.91E-05	1.49E-03	3.40E-02	1.77E-02	0.010
Gliese 876 b	9.20E-08	1.13E-07	1.47E-04	6.26E-04	7.68E-04	6.97E-04	0.044
Gliese 876 c	7.25E-08	8.50E-08	1.47E-04	4.93E-04	5.78E-04	5.36E-04	0.028
HD 114762 b	1.47E-08	4.14E-08	2.36E-04	6.23E-05	1.76E-04	1.19E-04	0.011
HD 128311 b	5.32E-08	7.11E-08	5.26E-06	1.01E-02	1.35E-02	1.18E-02	0.061
HD 128311 c	1.50E-08	3.20E-08	5.26E-06	2.86E-03	6.09E-03	4.47E-03	0.106
HD 147513 b	1.20E-07	1.22E-07	3.48E-05	3.44E-03	3.51E-03	3.48E-03	0.098
HD 160691 b	3.74E-09	4.40E-09	5.65E-06	6.63E-04	7.79E-04	7.21E-04	0.098
HD 160691 c	1.87E-09	3.96E-09	5.65E-06	3.31E-04	7.00E-04	5.16E-04	0.273
HD 168443 b	2.08E-08	5.32E-08	5.32E-06	3.91E-03	1.00E-02	6.95E-03	0.009
HD 192263 b	2.20E-09	3.40E-08	3.66E-06	6.01E-04	9.30E-03	4.95E-03	0.008
HD 217107 b	2.69E-09	1.84E-08	4.16E-06	6.46E-04	4.42E-03	2.53E-03	0.002
HD 217107 c	2.68E-10	3.37E-10	4.16E-06	6.43E-05	8.09E-05	7.26E-05	0.116
HD 3651 b	1.07E-08	1.69E-08	1.16E-05	9.21E-04	1.46E-03	1.19E-03	0.026
HD 39091 b	5.43E-09	1.51E-08	3.99E-06	1.36E-03	3.79E-03	2.57E-03	0.160
HD 80606 b	2.38E-08	5.14E-08	1.70E-06	1.40E-02	3.02E-02	2.21E-02	0.008
rho CrB b	1.37E-08	1.40E-08	4.37E-06	3.12E-03	3.20E-03	3.16E-03	0.013
Tau Boo b	6.68E-08	5.39E-07	7.59E-04	8.80E-05	7.10E-04	3.99E-04	0.003
Ups And b	7.38E-08	3.78E-07	1.01E-03	7.30E-05	3.74E-04	2.24E-04	0.004
Ups And c	4.53E-08	5.53E-08	1.01E-03	4.49E-05	5.47E-05	4.98E-05	0.062
Ups And d	1.11E-08	2.45E-08	1.01E-03	1.10E-05	2.43E-05	1.76E-05	0.188

<sup>2</sup>These values are assuming an efficiency of 10%. For a much lower or higher efficiency, then these “Lower” or “Upper” limits might be considerably different.

HD 128311 b is in a multi-planet system with HD 128311 c, both of which are expected to have favorable planet/star contrast ratios due to the relatively low UV emission from their host star, a low mass K dwarf. An advantage to observing a multi-planet system is that the light from each planets' aurora could be combined to obtain an even larger planet/star contrast ratio. These two planets are slightly more massive than Jupiter (2.18 and 3.21  $M_{Jup}$ , respectively) and have highly eccentric orbits. HD 128311 b has a semi-major axis of 1.099 AU with a periastron of 0.714 AU and an apastron of 1.326 AU. HD 128311 c has a semi-major axis of 1.76 AU with its orbital distance ranging from 1.42 AU to 2.06 AU. Both planets have relatively long orbital periods, 448 and 919 days, respectively.

**Table 7-8** Results in Lyman Band. The upper and lower limits for the planet flux given in columns two and three are for the total planetary auroral emissions in the Lyman band (11% of total UV auroral emission [*Liu et al.*, 1995; 1998])

Planet name	Planet flux <sup>2</sup> (photons/cm <sup>2</sup> /sec)		Star flux (photons/cm <sup>2</sup> /sec)	Planet/star flux			Angular sep. (arcsec)
	Lower limit	Upper limit		Lower limit	Upper limit	Average	
47 Uma b	3.31E-09	4.40E-09	8.26E-05	4.00E-05	5.33E-05	4.67E-05	0.157
47 Uma c	5.13E-10	5.52E-10	8.26E-05	6.21E-06	6.68E-06	6.44E-06	0.280
51 Peg b	5.47E-09	2.72E-08	8.03E-05	6.81E-05	3.38E-04	2.03E-04	0.004
55 Cnc b	4.49E-09	4.94E-08	1.34E-05	3.35E-04	3.68E-03	2.01E-03	0.009
55 Cnc c	8.69E-09	1.35E-08	1.34E-05	6.48E-04	1.00E-03	8.26E-04	0.018
55 Cnc d	1.29E-09	2.89E-09	1.34E-05	9.66E-05	2.16E-04	1.56E-04	0.392
70 Vir b	1.46E-08	3.77E-08	2.14E-05	6.82E-04	1.76E-03	1.22E-03	0.022
Epsilon Eri b	2.48E-07	2.60E-07	4.62E-04	5.38E-04	5.63E-04	5.50E-04	1.031
GJ 3021 b	4.59E-07	9.87E-07	2.27E-05	2.02E-02	4.35E-02	3.18E-02	0.028
Gliese 86 b	8.02E-08	1.83E-06	4.76E-05	1.69E-03	3.84E-02	2.01E-02	0.010
Gliese 876 b	1.27E-07	1.56E-07	1.90E-04	6.66E-04	8.19E-04	7.43E-04	0.044
Gliese 876 c	9.98E-08	1.17E-07	1.90E-04	5.25E-04	6.16E-04	5.71E-04	0.028
HD 114762 b	2.02E-08	5.71E-08	6.12E-04	3.31E-05	9.33E-05	6.32E-05	0.011
HD 128311 b	7.33E-08	9.80E-08	9.95E-06	7.36E-03	9.85E-03	8.61E-03	0.061
HD 128311 c	2.07E-08	4.41E-08	9.95E-06	2.08E-03	4.44E-03	3.26E-03	0.106
HD 147513 b	1.65E-07	1.69E-07	4.22E-05	3.90E-03	4.00E-03	3.95E-03	0.098
HD 160691 b	5.15E-09	6.07E-09	8.14E-05	6.33E-05	7.46E-05	6.89E-05	0.098
HD 160691 c	2.57E-09	5.45E-09	8.14E-05	3.16E-05	6.70E-05	4.93E-05	0.273
HD 168443 b	2.86E-08	7.33E-08	6.44E-06	4.44E-03	1.14E-02	7.91E-03	0.009
HD 192263 b	3.03E-09	4.69E-08	6.92E-06	4.38E-04	6.78E-03	3.61E-03	0.008
HD 217107 b	3.70E-09	2.53E-08	5.40E-06	6.85E-04	4.69E-03	2.69E-03	0.002
HD 217107 c	3.68E-10	4.64E-10	5.40E-06	6.82E-05	8.59E-05	7.71E-05	0.116
HD 3651 b	1.47E-08	2.33E-08	2.19E-05	6.72E-04	1.07E-03	8.69E-04	0.026
HD 39091 b	7.48E-09	2.08E-08	5.75E-05	1.30E-04	3.62E-04	2.46E-04	0.160
HD 80606 b	3.27E-08	7.08E-08	2.06E-06	1.59E-02	3.44E-02	2.51E-02	0.008
rho CrB b	1.88E-08	1.93E-08	6.29E-05	2.99E-04	3.07E-04	3.03E-04	0.013
Tau Boo b	9.19E-08	7.42E-07	1.96E-03	4.69E-05	3.79E-04	2.13E-04	0.003
Ups And b	1.02E-07	5.21E-07	2.63E-03	3.86E-05	1.98E-04	1.18E-04	0.004
Ups And c	6.24E-08	7.62E-08	2.63E-03	2.37E-05	2.90E-05	2.63E-05	0.062
Ups And d	1.53E-08	3.38E-08	2.63E-03	5.81E-06	1.28E-05	9.33E-06	0.188

Their orbital distances and large eccentricities suggest that these planets are not tidally locked. However, if we assume  $\omega = P_{orb}$ , then we observe a two order of magnitude decrease in the lower limit for the expected auroral flux, while the upper limit remains constant.

HD 168443 b is larger than the previous planets ( $7.2 M_{Jup}$ ) with a semi-major axis of 0.29 and an eccentricity of 0.53. This planet, which orbits HD 168443, another spectral type G star, is also in multi-planet system, and the sister planet, HD 168443 c, might contribute to the auroral signal as well.

### **7.7.1 The UV Advantage**

Observing EGPs in the ultraviolet provides three major advantages over observing the planets at visible wavelengths. First, planet/star contrast ratios in the ultraviolet are predicted to be  $10^{-2}$  to  $10^{-6}$  orders of magnitude better than the expected planet/star contrast ratios in the visible,  $\sim 10^{-7}$  to  $10^{-10}$  [Burrows, 2005]. Contrast ratios are better by  $\sim 10^4$  in the UV, the photon flux would be significantly lower in this region than the photon flux in the visible, which results from planet-reflected star light. Long observing times ( $\sim 2$ -100 hours) would be required to collect  $10^3$  photons using the HST/ACS SBC in the Werner band. In the Lyman band, observing times  $> 10^3$  hours are required for some of the 40 planets in this survey. If the star's light could be suppressed by a factor of 100 (i.e. with the use of a coronagraph) then it would take less than an hour to achieve a S/N ratio of 10 for the majority of the EGPs. Given the lower flux limit for the top candidate planets, it would take about 30 minutes to achieve a S/N ratio of 10.

Second, observing in the ultraviolet provides higher spatial resolution compared to the visible. Spatial resolution scales as  $\sim \lambda/D$ , where  $\lambda$  is the wavelength of the observation and  $D$  is the diameter of the telescope. By observing at shorter wavelengths, higher spatial resolution can be achieved. With increased spatial resolution, planets orbiting closer to their host stars can be resolved; a significant advantage since the majority of known EGPs orbit at small angular separations from their host stars. At visible wavelengths the

resolution limit would be ~2-6 times larger. The higher spatial resolution in the UV results in planets detected ~0.2 times closer to their host stars. Planets orbiting closer to their stars will also be brighter by ~8.5 times.

The third advantage to observing at ultraviolet wavelengths is that light is concentrated according to  $(\lambda/D)^2$ . At smaller wavelengths, the light from the planet's aurora will be more concentrated than in the visible or infrared. Highly concentrated auroral light aids in detecting planets over background light from the star.

### 7.7.2 Detecting a Solar System Analogue

While there are several advantages in searching for extrasolar planets at ultraviolet wavelengths, detecting a solar system analogous to our own would still prove difficult even with the observational advantages of the UV. Assuming a planetary system identical to our own with a solar-type host star and a Jupiter-sized planet at 5.2 AU with Jupiter's known auroral emission strengths, we consider planetary systems at various distances from Earth. Distances range from 5 to 500 parsecs and auroral emission values used are the average UV emissions from Jupiter scaled for distance. Planet auroral flux values, as seen from Earth, and planet/star contrast ratios are calculated for these solar system analogues (Table 7-9). Solar flux values were obtained from the UARS Solar UV Irradiance Reference Spectrum, the average of UARS SUSIM and SOLSTICE data from 29 March 1992, and flux values were scaled for distance to the planetary systems.

**Table 7-9** Results for detecting a solar system analogue at various distances from Earth. The values used are average values for Jupiter's auroral emissions, scaled for distance to the planetary systems.

Distance to planetary system (parsecs)	Planet flux (photons/cm <sup>2</sup> /sec)		Star flux (photons/cm <sup>2</sup> /sec)		Planet/star flux (photons/cm <sup>2</sup> /sec)		Ang. sep. (arcsec)
	Werner band	Lyman band	Werner band	Lyman band	Werner ratio	Lyman ratio	
5	2.09E-08	2.88E-08	4.21E-07	2.46E-06	4.96E-02	1.17E-02	1.04
10	5.23E-09	7.20E-09	1.05E-07	6.15E-07	4.98E-02	1.17E-02	0.52
15	2.32E-09	3.20E-09	4.67E-08	2.73E-07	4.97E-02	1.17E-02	0.35
20	1.31E-09	1.80E-09	2.63E-08	1.54E-07	4.98E-02	1.17E-02	0.26
50	2.09E-10	2.88E-10	4.21E-09	2.46E-08	4.96E-02	1.17E-02	0.10
100	5.23E-11	7.20E-11	1.05E-09	6.15E-09	4.98E-02	1.17E-02	0.05
150	2.32E-11	3.20E-11	4.67E-10	2.73E-09	4.97E-02	1.17E-02	0.03
200	1.31E-11	1.80E-11	2.63E-10	1.54E-09	4.98E-02	1.17E-02	0.03
300	5.81E-12	8.00E-12	1.17E-10	6.83E-10	4.97E-02	1.17E-02	0.02
500	2.09E-12	2.88E-12	4.21E-11	2.46E-10	4.96E-02	1.17E-02	0.01

**Table 7-10** Time required to collect 1,000 photons from a Jupiter-type planet in a planetary system analogous to the solar system using the JWST.

System distance (parsecs)	Werner band (hours)	Lyman band (hours)
5	53.1	38.6
10	212.5	154.3
15	478	347.1
20	849.9	617
50	5311.6	3856.3

The observing times required to collect 1,000 photons from these hypothetical planets would be  $>10^3$  hours using the HST/ACS SBC for even the best scenario (an analogous system only 5 parsecs from Earth). However, if we consider the use of the future James Webb Space Telescope (JWST), which is projected to launch in 2018, observing times become more reasonable for some of the closer planetary systems (Table 7-10). These calculations assume an 8 m primary mirror with a throughput of 50%.

Next, we compare the observing times required to collect 1,000 photons from these solar-system-analogue Jupiters to known extrasolar planets. The observing times necessary to collect the same number of photons from auroral emissions of known extrasolar planets is computed again assuming the use of the JWST with the results given in Table 7-11. These values are calculated for both the Werner and Lyman bands using the upper limits for the expected auroral emission strengths, hence these times represent the lower limit for the amount of time required to collect 1,000 photons using the JWST.

## **7.8 Discussion and Conclusions**

This chapter has presented a critical analysis of the expected auroral emission from EGPs considering both planetary and stellar parameters. Many parameters influence the expected auroral output and no single parameter can serve as the sole indicator of likely candidate planets.

**Table 7-11** Time required to collect 1,000 photons from several known EPGs using the JWST.

Planet name	Werner band (hours)	Lyman band (hours)
47 Uma b	347.7	252.3
47 Uma c	2774.9	2013.3
51 Peg b	56.4	40.9
55 Cnc b	31	22.5
55 Cnc c	113.8	82.6
55 Cnc d	529.7	384.3
70 Vir b	40.6	29.5
Epsilon Eri b	5.9	4.3
GJ 3021 b	1.6	1.1
Gl 86 b	0.8	0.6
Gliese 876 b	9.8	7.1
Gliese 876 c	13.1	9.5
HD 114762 b	26.8	19.5
HD 128311 b	15.6	11.3
HD 128311 c	34.7	25.2
HD 147513 b	9.1	6.6
HD 160691 b	252.3	183.1
HD 160691 c	280.9	203.8
HD 168443 b	20.9	15.2
HD 192263 b	32.6	23.7
HD 217107 b	60.4	43.8
HD 217107 c	3300.8	2394.9
HD 3651 b	65.6	47.6
HD 39091 b	73.6	53.4
HD 80606 b	21.6	15.7
rho CrB b	79.4	57.6
Tau Boo b	2.1	1.5
Ups And b	2.9	2.1
Ups And c	20.1	14.6
Ups And d	45.3	32.9

Considering stellar characteristics, stellar mass-loss rates are important as many of the top candidate planets had mass-loss rates greater than the solar rate; however, three of the top 14 stars had mass-loss rates less than the solar value. Of the 15 most promising candidate planets, all orbit stars of spectral type G and K. The top ten planet-hosting stars range from G3V to K1V, all slightly cooler than solar type stars (G2V). Stellar distance did not play a large role since we are considering the planet/star contrast ratios.

Among the most promising candidate planets, planetary characteristics vary widely. The magnetic dipole moment, thought to be an important factor contributing to the intensity of a planet's aurora, does not show a consistent trend. HD 114762 b is estimated to have the largest dipole moment,  $\mathcal{M} = 54 \mathcal{M}_{Jup}$ , six times the average dipole moment for the 40 planet sample, and yet HD 114762 b has an expected auroral emission flux less than the sample average. Of the top 11 candidate planets, the magnetic dipole moments range from

the second largest for HD 39091 b ( $\mathcal{M} = 48 \mathcal{M}_{Jup}$ ), to the second smallest for HD 3651 b ( $\mathcal{M} = 0.12 \mathcal{M}_{Jup}$ ).

The effect of tidal locking is another influential factor. Magnetic dipole moments were calculated twice, once assuming all planets were tidally locked, and a second time assuming only planets in orbits closer than 0.2 AU with an eccentricity of less than 0.2 were tidally locked, while all other planets were assumed to have a rotational period of 0.4 days. Results for the tidally-locked vs. not tidally-locked case vary substantially for the minimum values of the magnetic dipole moment, but do not vary for the maximum values. The difference between a tidally-locked planet and a planet with a rotational period of 0.4 days varies by as much as  $10^2$ , suggesting that rotation rate does have an effect on the strength of the planetary dipole moment, and as such, significantly affects the expected auroral emission strength. Thus, the ability to predict the rotational period of EGPs is essential for determining the most promising candidate planets.

### **7.8.1 Model limitations**

Several potentially influential parameters in calculating the expected auroral strength from EGPs remain to be explored:

- (i) The activity level of the host star likely has a significant impact since on Earth both dynamic and static aurora are observed between quiet periods and periods of solar activity.
- (ii) The presence of satellites and/or rings around the planet could contribute a plasma source, as is the case of Io for Jupiter. According to *Scharf* [2006] it is likely that many of the extrasolar planets found to date have orbiting satellites since all the giant planets in our solar system are known to have satellites. These additional plasma sources would greatly increase the strength of the expected aurora.
- (iii) Stellar UV chromospheric emissions for the host-stars also need to be taken into account. UV emission likely scales as a function of X-ray flux, a quantity that is known for

the majority of host stars; however, the only published correlation between X-ray flux and UV flux is for M dwarfs [*Hawley and Johns-Krull, 2003*]. It is likely that stars with larger X-ray emissions will have larger UV emissions, but the exact correlation is unknown and remains for future work.

(iv) The efficiency of the conversion of stellar wind power to auroral emission remains highly uncertain. *Yelle [2004]* states that the efficiency of auroral emission might be higher for planets hotter than Jupiter since the molecular hydrogen can be in a higher vibrational state, which absorbs the Lyman  $\alpha$  photons from the star efficiently and possibly results in stronger auroral emission.

### **7.8.2 Future Observing Prospects**

Several proposed future missions might be better suited to make the required observations; these mission include the Stellar Imager (SI), a UV-Optical, space-based interferometer designed to enable 0.1 milli-arcsecond spectral imaging [*Carpenter et al., 2006*], and the World Space Observatory (WSO), an 1.7 meter space telescope operating at the second Lagrangian point and consisting of three UV spectrometers [*Barstow et al., 2003*]. The most promising of these two future instruments is the Stellar Imager, which has  $\lambda$ -coverage in the UV from 1200-3200 Å, with an angular resolution of 50  $\mu$ as at 1200 Å. This interferometer would consist of 20-30 formation-flying “mirrorstats” with a beam combining hub providing a maximum baseline of 1000 m. The minimum field of view (FOV) is  $> 4$  mas and the spectral resolution in the UV is 10 Å [*Carpenter et al., 2006*].

In summary, a detailed analysis of the expected UV auroral emission from EGPs has been performed and on the basis of the results presented here, the prospect of detecting EGP aurora could be feasible using future high-contrast space-based instruments.

## Chapter 8: Summary and Future Work

The goal of this dissertation has been to examine the plasma physics processes that drive ring current enhancements, and the findings presented in the previous chapters represent significant gains in our understanding of the development and composition of the ring current during geomagnetic storms and substorms. This chapter provides a brief summary of the major findings and then discusses potential areas where future efforts could be placed to further this line of research.

### **8.1 Summary of Major Findings**

First we examined the energization of ionospheric ions in the terrestrial magnetotail and the trapping of these particles in the ring current. Using single-particle tracking in combination with multifluid simulations we investigated the processes that drive the injection of particles into the inner magnetosphere, the mechanisms through which the particles are energized, and the conditions that lead to the formation of both the asymmetric and symmetric components of the ring current.

Next we examined the contribution from various ionospheric source regions to the storm time ring current and the effect of the IMF  $B_z$  component on producing a symmetric ring current. We investigated the dominant ionospheric species contributing to the ring current energy density, the ionospheric source regions that are the primary contributors of particles and energy to the storm time ring current, and the way in which these results vary over the course of the storm. Using our results, we determined the most geo-optimal locations for ionospheric ions to contribute to the ring current. The following sections summarize the major findings presented in this dissertation.

### **Particle Energization Depends on Magnetotail Structures**

Findings show that for particle energization, structures within the magnetotail are more important in determining when particles get accelerated than the time elapsed since particles were launched from the ionosphere. For the case of an idealized substorm with a continuously southward IMF, particle acceleration was observed to correspond with the formation of an injection front associated with an earthward moving flux rope at substorm onset. Substorm development was noted by the presence of a large flux rope and a thin, kinked current sheet, and such features were shown to play a central role in particle acceleration and their presence resulted in increased particle energization.

### **Important Role of Small-Scale Structures in Particle Energization**

Small-scale structures such as the kinks in the thin current sheet were found to play an important role in particle energization. Results showed that oxygen ions followed the sinusoidal path bounded by the Hall electric field as the particles convected duskward due to the cross-tail current, and as the oxygen ions moved through these kinks, they gained energy. Flux ropes forming within the current sheet were observed to be bounded above and below by the Hall current, and intensifications in the Hall component of the electric field were found to occur on the outer edge of the kinks. In order to resolve the kinks, high-resolution capabilities are necessary, as evidenced by substantial differences between low-resolution and high-resolution results. When kinks and the thin current sheet are under-resolved, the peak magnitude of the Hall current was found to be significantly reduced. In the low-resolution simulations, particles were not energized in the tail by small-scale plasma structures as observed in the high-resolution case, but rather the particles were only energized when they encountered hot plasma near the low-latitude boundary layer. This resulted in lower energization levels and ring current formation was not observed.

### **Acceleration Mechanisms Differ Between $H^+$ and $O^+$**

During substorms asymmetries were observed between ionospheric  $H^+$  and  $O^+$  acceleration mechanisms. Once oxygen ions reached the thin current sheet, their large gyroradius compared to the thin current sheet resulted in  $O^+$  breaking the frozen-in condition and

moving independently of the field lines. Oxygen ions were observed to convect duskward according to the cross-tail current, and they gained more energy than the protons, which moved earthward on reconnecting field lines and were energized by bursty bulk flows closer to the plasma sheet inner boundary. This resulted in  $H^+$  flowing in a field-aligned direction, while  $O^+$  flowed perpendicular to the field. These two perpendicular ion streams provided a possible explanation for the two separate ion components observed by THEMIS: one ion component flowing in a field-aligned direction and other ion component flowing perpendicular to the field.

### **Northward Turning IMF Traps Particles in the Ring Current**

It was found that a northerly turning IMF at, or shortly after, onset is important in producing a symmetric ring current, but the degree of turning is not as critical. After the outflowing ionospheric ions have been accelerated during an initial period of southward IMF, a northward turning of the IMF is found to be necessary to trap energetic particles in orbit around the Earth and to form a symmetric ring current. During periods of southward IMF, when the magnetopause is compressed, energetic particles convecting around Earth encounter the dayside reconnection region near local noon and are lost over the polar cap. However, with a northward turning of the IMF, the magnetopause moves out, allowing particles previously energized during the southward IMF to become trapped and convect beyond the dayside reconnection region. While a northward turning was found to be essential for particle trapping, the magnitude of the northward turning did not significantly affect ring current formation. Findings suggest that as long as the degree of northward turning is sufficient to allow the magnetosphere to expand enough for particles to convect past noon, the strength of the northward  $B_z$  component of the IMF does not appreciably affect the trapping of particles in the ring current.

### **Large Decreases in *Dst* Associated with Increased $O^+$ in the Ring Current**

It was found that while the dominant ionospheric species contributing to the ring current energy density varies over the duration of a storm, a significant increase in ionospheric  $O^+$  contribution to the ring current is always associated with large decreases in *Dst*. For a small decrease in *Dst*, such as is observed during a substorm, the ring current energy

density was found to be dominated by hydrogen ions. However, during large decreases in *Dst*, such as during storm main phase, a significant increase in the contribution of oxygen ions is observed.

### **Additional $O^+$ in the Ring Current due to Enhanced Outflow and Efficiency**

The increase in  $O^+$  concentration observed during the main phase of a storm was determined to result from two factors: an increased ionospheric outflow rate and an increased efficiency at accumulating  $O^+$  in the inner magnetosphere. During the main phase of the storm, currents within the atmosphere heat the oxygen ions and raise their scale height, allowing an increase in oxygen ion outflow to be observed. In addition to increased  $O^+$  outflow rates during the main phase of the storm, changes in the flow pattern of oxygen ions also contributed to the increased presence of oxygen in the storm time ring current. While  $O^+$  experiences strong cross-tail acceleration during the early phase of the storm, there are also significant losses down the tail. The efficiency of ionospheric  $O^+$  amassing in the ring current increases during the main phase of the storm when oxygen ions experience stronger earthward acceleration and more ions collect in the ring current region.

### **Identification of Primary Ionospheric Source Regions of Ring Current Ions**

This work produced the first maps of the relative contributions of various ionospheric outflow regions to the storm time ring current. The outflow regions considered spanned all MLTs and latitudes, and both outflowing  $H^+$  and  $O^+$  were modeled. It was found that during the early part of the storm, high latitude outflow regions near midnight were the most efficient sectors at contributing particle density to the ring current, while during the main phase of the storm greater contribution from all MLTs was observed. The source regions of outflowing ionospheric particles were found to vary with the size, extent, and location of the separatrix. During the early phase of the storm, a smaller more compact separatrix resulted in ring current particles originating from a limited region extending from 00 to 06 MLT at high latitudes. During the main phase of the storm, the polar cap was found to expand to include a wider source region and outflowing ions from all MLTs and latitudes were observed to contribute to the ring current with low latitudes between 21

and 03 MLT contributing most significantly. The sectors that contributed the majority of the energy were consistently the high latitude regions on the dawn side. These results provided the first link between MLT and magnetic latitude variations in ionospheric outflow and the amount that individual ionospheric regions contribute to the build-up of the ring current.

### **Possibility of Detecting Auroral Emissions from Extrasolar Planetary Systems**

A detailed analysis of the expected UV auroral emission from extrasolar giant planets found that detecting such auroral signatures could be feasible using future high-contrast space-based telescopes. Such results have astrobiological implications as they help us to define and characterize these distant worlds and their atmospheres. Detection of an auroral signature provides information about the composition of a planet's atmosphere and the potential of an intrinsic magnetic field. A planetary magnetic field could generate a magnetosphere, which would enshroud the planet and offer protection from intense stellar radiation effects and from atmospheric stripping due to a stellar wind. Knowing such planetary properties would not only enhance the amount we know about these distant worlds, but also be useful from an astrobiological standpoint and aid astrobiologists in determining the habitability of observed exoplanets.

## **8.2 Recommendations for Future Work**

The results presented in this work support several avenues of further investigation. A potential future line of research is to use the newly developed coupled particle / multifluid code discussed in section 3.3 to investigate the extent to which the ring current particles affect the global electric and magnetic fields in the magnetosphere. This new coupled model has enormous potential to more accurately investigate the dynamics of the inner magnetosphere, a region in which, when using the two codes separately, we have observed that the multifluid code constantly underestimates the magnitude of magnetic field. This is likely due to the inability of a multifluid description to fully capture the ring current's contribution to the magnetic field in this region.

The inclusion of feedback from the particles in the multifluid / particle code will not only provide insight into the problem of the disparate magnetic field magnitudes in the inner magnetosphere, but will also enable better modeling of this complicated and coupled region. Using a self-consistent treatment is the next step in investigating both the large and small-scale processes that drive particle dynamics within the global magnetosphere. Thus, by using a fluid description for all species globally and invoking individual particles for the high energy tail in key regions, a realistic treatment of a full planetary magnetosphere can be realized, which is necessary to develop accurate space weather models.

On Earth space weather affects a wide range of technologies and services, and developing predictive space weather models is key not only for our explorations of space, but also for our continued technological development. The effects of severe space weather on Earth make us question the consequences of such effects on planets in other planetary systems. As we search for life elsewhere in the universe, one question that remains to be answered is what effects radiation belts and ring currents have on the habitability of a planet. When considering the ring current, astrobiologists are interested in the question: Is the ring current protective or harmful for extant and developing life, and under what conditions? Specifically when considering the habitability of extrasolar planets in orbit around stars other than familiar G type stars like the Sun, we want to know: Can a ring current help protect a planet, such as an earth-like planet in the habitable zone of an M dwarf star that has significant stellar activity and large UV fluxes? Such questions could be explored using models such as those presented in this dissertation.

As our society becomes increasingly dependent on technology and as the number of satellites in orbit continues to grow, understanding space weather and developing strategies to alleviate the effects of space storms becomes increasingly important. This dissertation has contributed substantially to our understanding of the development and composition of the ring current during geomagnetic storms and substorms. Such an understanding is critical in order to characterize, forecast, and mitigate the effects of space weather.

## Bibliography

- Abe, T., D.J. Knudsen, A.W. Yau, S. Watanabe, and E. Sagawa (2001), Simultaneous satellite and radar observations of the polar ion outflow and the flux variation with the geomagnetic condition, *Adv.Space Res.*, *27*, 8, 1403–1412.
- Allard, F., P.H. Hauschild, and A. Schweitzer (2000), Spherically symmetric model atmospheres for low-mass pre-main-sequence stars with effective temperatures between 2000 and 6800 K, *Astrophysical Journal*, *539*, 366–371.
- Andersson, L., W.K. Peterson, and K.M. McBryde (2004), Dynamic coordinates for auroral ion outflow, *J.Geophys.Res.*, *109*, A08201, doi:10.1029/2004JA010424.
- Andre, M., and A. Yau (1997), Theories and observations of ion energization and outflow in the high latitude magnetosphere, *Space Sci.Rev.*, *80*, 27–48.
- Angelopoulos, V., et al.(2008), Tail reconnection triggering substorm onset, *Science*, *321*, 5891, 931–935.
- Ashour-Abdalla, M., M. El-Alaoui, V. Perroomian, R.J. Walker, J. Raeder, L.A. Frank, and W.R.Paterson (1999), Source distributions of substorm ions observed in the near-Earth magnetotail, *Geophys.Res.Lett.*, *26*, 955–958.
- Bagenal, F. (1992), Giant planet magnetospheres, *Annu. Rev. Earth Planet. Sci.*, *20*, 289–328.
- Baker, D.N., and I.A. Daglis (2006), Radiation belts and ring current, in *Space Weather - Physics and Effects*, edited by V.Bothmer and I.A.Daglis, 173–202, Springer Verlag, Berlin.
- Barstow, M.A., et al. (2003), The WSO: a world-class observatory for the ultraviolet, *SPIE*, *4854*, 364–374.
- Bastian, T.S., G.A. Dulk, and Y. Leblanc (2000), A search for radio emission from extrasolar planets, *Astrophysical Journal*, *545*, 1058–1063.
- Baum, S.A. (1997), *The 1997 HST calibration workshop with a new generation of instruments*, p. 3.
- Baumjohann, W., and R.A. Treumann (2006), *Basic Space Plasma Physics*, Imperial College Press, London.
- Beatty, J.K., C.C. Petersen, and A. Chaikin, eds. (1999), *The new solar system fourth edition*, Cambridge University Press, Cambridge.

- Beaulieu, J.P., et al. (2006), Discovery of a cool planet of 5.5 Earth masses through gravitational microlensing, *Nature*, 439, 437–440.
- Beichman, C.A., et al. (2005), Planets and infrared excesses: preliminary results from a Spitzer MIPS survey of solar-type stars, *Astrophysical Journal*, 622, 1160–1170.
- Bertaux, R.-L., et al. (2005), Discovery of aurora on Mars, *Nature*, 435, 790–704.
- Beuzit, J. L., et al. (2007), Direct detection of exoplanets, *Protostars and Planets V*, 951, 717–732.
- Bhardwaj A. and R. Gladstone (2000a), Auroras on Saturn, Uranus, and Neptune, *Adv. Space Res.*, 26, 1551–1558.
- Bhardwaj, A. and R. Gladstone (2000b), Auroral emissions of the giant planets, *Rev. of Geophys.*, 38, 295–354.
- Birn, J., M.F. Thomsen, J.E. Borovsky, G.D. Reeves, D.J. McComas, R.D. Belian, and M. Hesse (1997), Substorm electron injections: Geosynchronous observations and test particle simulations, *J. Geophys. Res.*, 103(A5), 9235–9248
- Bond I.A., et al. (2004), OGLE 2003-BLG-235/MOA 2003-BLG-53: A Planetary Microlensing Event, *Astrophysical Journal*, 606, L155–L158.
- Bothmer, V., and I.A. Daglis (Eds.) (2007), *Space Weather-Physics and Effects*, Springer, Berlin.
- Bradford, W.J. and J.J. Drake (2001), Observability of stellar winds from late-type dwarfs via charge exchange x-ray emission, *Astrophysical Journal*, 546, L57–L60.
- Brautigam, D.H. (2002), CRRES in review: space weather and its effects on technology, *J. Atmos. Sol. Terr. Phys.*, 64, 1709–1721.
- Broadfoot A.L., et al., (1979), Extreme ultraviolet observations from Voyager 1 encounter with Jupiter, *Science*, 204, 979–982.
- Burrows A. (2005), A theoretical look at the direct detection of giant planets outside the solar system, *Nature*, 433, 261–268.
- Busse, F.H. (1976), Generation planetary magnetism by convection, *Phys. Earth Planet. Inter.*, 12, 350–358.
- Butler, B.J. (2003), Long wavelength emission from extrasolar planets, *Bulletin American Astro. Soc.*, 35, 750.
- Cain, J.C., et al. (1995), The magnetic bode fallacy, *J. Geophys. Res.*, 100, 9439–9454.
- Carpenter, K.G., et al. (2006), Imaging terrestrial planets with a free-flying occulter and space telescope: an optical simulation, *SPIE*, 5491, 262–271.

- Cash, M.D., R.M. Winglee, and E.M. Harnett (2010a), Ring current formation influenced by solar wind substorm conditions, *J. Geophys. Res.*, *115*, A05218, doi:10.1029/2009JA014909.
- Cash, M.D., R.M. Winglee, and E.M. Harnett (2010b), Storm time production of ring current ions: Variation in particle energization and injection with ionospheric source region, *J. Geophys. Res.*, *115*, A00J12, doi:10.1029/2010JA015759.
- Chappell, C., T. Moore, and J. Waite Jr. (1987), The ionosphere as a fully adequate source of plasma for the Earth's magnetosphere, *J. Geophys. Res.*, *92(A6)*, 5896–5910.
- Charbonneau, D., Brown, T. M., Burrows, A., and G. Laughlin (2007), When extrasolar planets transit their parent stars, *Protostars and Planets V*, *951*, 701–716.
- Charbonneau, D., Brown, T., Noyes, R., and R. Gilliland (2002), Detection of an extrasolar planet atmosphere, *Astrophysical Journal*, *568*, 377–384.
- Choi, H.-S., et al. (2011), Analysis of GEO spacecraft anomalies: Space weather relationships, *Space Weather*, *9*, S06001, doi:10.1029/2010SW00059.
- Clarke, J.T., et al. (1994), Hubble Space Telescope Goddard high-resolution spectrograph H2 rotational spectra of Jupiter's aurora, *Astrophysical Journal*, *430*, L73–L76.
- Clarke, J.T., H.W. Moos, S.K. Atreya, and A.L. Lane (1980), Observations from earth orbit and variability of the polar aurora on Jupiter, *Astrophysical Journal*, *241*, L179–L182.
- Collin, H., R. Sharp, and E. Shelley (1984), The magnitude and composition of the outflow of energetic ions from the ionosphere, *J. Geophys. Res.*, *89(A4)*, 2185–2194.
- Daglis, I. A., W. I. Axford, S. Livi, B. Wilken, M. Grande, and F. Soraas (1996), Auroral ionospheric ion feeding of the inner plasma sheet during substorms, *J. Geomagn. Geoelectr.*, *48*, 729–739.
- Daglis, I.A. (1997), The role of magnetosphere–ionosphere coupling in magnetic storm dynamics, in *Magnetic Storms, Geophys. Monogr. Ser.*, vol.98, edited by B. T. Tsurutani et al., pp. 107–116, AGU, Washington, D. C.
- Daglis, I.A., and W.I. Axford (1996), Fast ionospheric response to enhanced activity in geospace: Ion feeding of the inner magnetotail, *J. Geophys. Res.*, *101*, 5047–5065.
- Daglis, I.A., et al. (1999a), Variations of the ion composition during a large magnetic storm and their consequences, *Phys. Chem. Earth*, *24*, 229–232.
- Daglis, I., et al. (1999b), The terrestrial ring current: Origin, formation, and decay, *Rev. Geophys.*, *37(4)*, 407–438.

- Daglis, I.A., S. Livi, E.T. Sarris, and B. Wilken (1994), Energy density of ionospheric and solar wind origin ions in the near-Earth magnetotail during substorms, *J. Geophys. Res.*, *99*(A4), 5691–5703.
- De Michelis, P., I. Daglis, and G. Consolini (1997), Average terrestrial ring current derived from AMPTE/CCE–CHEM measurements, *J. Geophys. Res.*, *102*(A7), 14103–14111.
- de Pater I., and J.J. Lissauer (2001), *Planetary Sciences*, Cambridge Univ. Press, Cambridge.
- Delcourt, D.C. (2002), Particle acceleration by inductive electric fields in the inner magnetosphere, *J. Atmos. Sol. Terr. Phys.*, *64*, 551–559.
- Delcourt, D.C., and J.A. Sauvaud (1998), Recirculation of plasma sheet particles into the high-latitude boundary layer, *J. Geophys. Res.*, *103*, 26521–26532.
- Delcourt, D.C., T.E. Moore, and C.R. Chappell (1994), Contribution of low-energy ionospheric protons to the plasma sheet, *J. Geophys. Res.*, *99*, 5681–5689.
- Deming D., J. Harrington, S. Seager, and L.J. Richardson (2006), Strong infrared emission from the extrasolar planet HD 189733b, *Astrophysical Journal*, *644*, 560–564.
- Deming, D., S. Seager, L.J. Richardson, and J. Harrington (2005), Infrared radiation from an extrasolar planet, *Nature*, *434*, 740–743.
- Ebihara, Y., M. Yamada, S. Watanabe, and M. Ejiri (2006), Fate of outflowing suprathermal oxygen ions that originate in the polar ionosphere, *J. Geophys. Res.*, *111*, A04219, doi:10.1029/2005JA011403.
- Elliott, H.A., et al. (2001), Solar wind influence on the oxygen content of ion outflow in the high-altitude polar cap during solar minimum conditions, *J. Geophys. Res.*, *106*(A4), 6067–6084.
- Erickson, G.M., and R.A. Wolf (1980), Is steady convection possible in the Earth's magnetotail?, *Geophys. Res. Lett.*, *7*(11), 897–900.
- Esprete J., 2005, Catalog of 156 confirmed extrasolar planets and their 133 parent stars, astro-ph/0508317.
- Faber J.A., F.A. Rasio, and B. Willems (2005), Tidal interactions and disruptions of giant planets on highly eccentric orbits, *Icarus*, *175*, 248–262.
- Farrell W.M., M.D Desch., and P. Zarka (1999), On the possibility of coherent cyclotron emission from extrasolar planets, *J. Geophys. Res.*, *104*, 14025–14032.

- Favata F., et al. (2004), High-amplitude, long-term X-ray variability in the solar-type star HD 81809: The beginning of an X-ray activity cycle?, *Astronomy and Astrophysics*, 418, L13–L16.
- Fischer D.A., and J. Valenti (2005), The planet-metallicity correlation, *Astrophysical Journal*, 622, 1102–1117.
- Fok, M.-C., R. Wolf, R. Spiro, and T. Moore (2001), Comprehensive computational model of Earth's ring current, *J. Geophys. Res.*, 106(A5), 8417–8424.
- Fok, M.-C., T. Moore, and D. Delcourt (1999), Modeling of inner plasma sheet and ring current during substorms, *J. Geophys. Res.*, 104(A7), 14557–14569.
- Fok, M.-C., T. Moore, and M. Greenspan (1996), Ring current development during storm main phase, *J. Geophys. Res.*, 101(A7), 15311–15322.
- Frank, L.A. (1967), On the extraterrestrial ring current during geomagnetic storms, *J. Geophys. Res.*, 72(15), 3753–3767.
- Ganushkina, N.Y., et al. (2011), Locations of boundaries of outer and inner radiation belts as observed by Cluster and Double Star, *J. Geophys. Res.*, 116, A09234, doi:10.1029/2010JA016376.
- Gérard, J.C., V. Dols, R. Paresce, R. Prangé (1993), Morphology and time variation of the Jovian far UV aurora: Hubble Space Telescope observations, *J. Geophys. Res.*, 98, 18793–18801.
- Gloeckler, G., et al. (1985), First composition measurement of the bulk of the storm-time ring current (1 to 300 keV/e) with AMPTE–CCE, *Geophys. Res. Lett.*, 12(5), 325–328.
- Gonzaga, S., et al. (2005), “ACS Instrument Handbook”, Version 6.0, (Baltimore: STScI)
- Grißmeier, J.-M., et al. (2004), The effect of tidal locking on the magnetospheric and atmospheric evolution of “Hot Jupiters”, *Astronomy and Astrophysics*, 425, 753–764.
- Gustin, J., et al. (2004), Jovian auroral spectroscopy with FUSE: analysis of self-absorption and implications for electron precipitation, *Icarus*, 171, 336–355.
- Hamilton, D., et al. (1988), Ring current development during the great geomagnetic storm of February 1986, *J. Geophys. Res.*, 93(A12), 14343–14355.
- Harnett, E.M., R.M. Winglee, A. Stickle, and G. Lu (2008), Prompt ionospheric/magnetospheric responses 29 October 2003 Halloween storm: Outflow and energization, *J. Geophys. Res.*, 113, A06209, doi:10.1029/2007JA012810.

- Harnett, E.M., R.M. Winglee, and C. Paty (2006), Multi-scale/multi-fluid simulations of the post plasmoid current sheet in the terrestrial magnetosphere, *Geophys. Res. Lett.*, *33*, L21110, doi:10.1029/2006GL027376.
- Harris, W., et al. (1996), Analysis of Jovian Auroral H Ly-alpha Emission (1981–1991), *Icarus*, *123*, 350–365.
- Hawley, S.L. and C.M. Johns–Krulls (2003), Transition region emission from very low mass stars, *Astrophysical Journal*, *588*, L109–L112.
- Howarth, A. and A.W. Yau (2008), The effects of IMF and convection on thermal ion outflow in magnetosphere-ionosphere coupling, *J. Atmos. Sol. Terr. Phys.* *70*, 2132–2143.
- Imber, S.M., et al. (2011), A THEMIS survey of flux ropes and traveling compression regions: Location of the near-Earth reconnections site during solar minimum, *J. Geophys. Res.*, *116*, A02201, doi:10.1029/2010JA016026.
- Jordanova, V., L. Kistler, C. Farrugia, and R. Torbert (2001), Effects of inner magnetospheric convection on ring current dynamics: March 10–12, 1998, *J. Geophys. Res.*, *106*(A12), 29705–29720.
- Jordanova, V., L. Kistler, J. Kozyra, G. Khazanov, and A. Nagy (1996), Collisional losses of ring current ions, *J. Geophys. Res.*, *101*(A1), 111–126.
- Kelley, M.C. (2009), *The Earth's Ionosphere: Plasma Physics and Electrodynamics*, Academic Press.
- Kidder, A.R. (2011), *Dynamic heavy ions and magnetic reconnection at Mercury and Saturn*. (Doctoral Dissertation). University of Washington, Seattle.
- Kim, Q.J., et al. (2003), *STIS Instrument Handbook, Version 7.0*, (Baltimore: STScI)
- Kivelson, M.G. and C.T. Russell C.T (1995), *Introduction to Space Physics*, Cambridge Univ. Press, Cambridge.
- Kozyra J.U., et al. (2002), Multistep *Dst* development and ring current composition changes during the 4–6 June 1991 magnetic storm, *J. Geophys. Res.*, *107* (A8), 1224, doi:10.1029/2001JA00023.
- Krimigis, S., et al. (1985), Magnetic storm of September 4, 1984: A synthesis of ring current spectra and energy densities measured with AMPTE/CCE, *Geophys. Res. Lett.*, *12*(5), 329–332.
- Lammer, H., W. Stumptner and G.J. Molina-Cuberos (2002), *Astrobiology: the quest for the conditions of life*, Springer Press, Berlin.

- Lavraud, B. and V.K. Jordanova (2007), Modeling the effects of cold–dense and hot–tenuous plasma sheet on proton ring current energy and peak location, *Geophys. Res. Lett.*, *34*, L02102, doi:10.1029/2006GL027566.
- Lennartsson, O.W., and R.D. Sharp (1982), A comparison of the 0.1–17 keV/e ion composition in the near equatorial magnetosphere between quiet and disturbed conditions, *J. Geophys. Res.* *87 (A8)*, 6109–6120.
- Lennartsson, W. (1987), Plasma sheet ion composition at various levels of geomagnetic and solar activity, *Physica Scripta.*, *36*, 367–371.
- Lennartsson, W. (1992), A scenario for solar wind penetration of Earth's magnetic tail based on ion composition data from the ISEE 1 spacecraft, *J. Geophys. Res.*, *97(A12)*, 19221–19238.
- Li X., T.E. Sarris, D.N. Baker, W.K. Peterson, and H.J. Singer (2003), Simulation of energetic particle injections associated with a substorm on August 27, 2001, *Geophys. Res. Lett.*, *30 (1)*, 1004, doi:10.1029/2002GL015967.
- Li, X., D. Baker, M. Temerin, G. Reeves, and R. Belian (1998), Simulation of dispersionless injections and drift echoes of energetic electrons associated with substorms, *Geophys. Res. Lett.*, *25(20)*, 3763–3766.
- Liu S., M.W. Chen, J.L. Roeder, L.R. Lyons, M. Schulz (2005), Relative contribution of electrons to the stormtime total ring current energy content, *Geophys. Res. Lett.*, *32*, L03110, doi:10.1029/2004GL021672.
- Liu, X., et al. (1995), High-resolution electron-impact study of the far-ultraviolet emission spectrum of molecular hydrogen, *Astrophysical Journal Sup. Series*, *101*, 375.
- Liu, X., et al. (1998), Electron-impact excitation and emission cross sections of the H<sub>2</sub> Lyman and Werner systems, *J. Geophys. Res.*, *103*, 26739–26758.
- Livengood, T.A. and H.W. Moos (1990), Jupiter's north and south polar aurorae with IUE data, *J. Geophys. Res.*, *17*, 2265–2268.
- Livengood, T.A., et al. (1992), Jovian ultraviolet auroral activity, 1981–1991, *Icarus*, *97*, 26–45.
- Lotko, W. (2007), The magnetosphere-ionosphere system from the perspective of plasma circulation: A tutorial, *J. Atmos. Sol. Terr. Phys.*, *69*, 191–211.
- Lui, A., and D. Hamilton (1992), Radial profiles of quiet time magnetospheric parameters, *J. Geophys. Res.*, *97(A12)*, 19325–19332.
- Lui, A., R. McEntire, and S. Krimigis (1987), Evolution of the ring current during two geomagnetic storms, *J. Geophys. Res.*, *92(A7)*, 7459–7470.

- Mayor, M. and D. Queloz (1995), A Jupiter-mass companion to a solar-type star, *Nature*, 378, 355–359.
- Mizutani, H., T. Yamamoto, and A. Fugimara (1992), A new scaling law of the planetary magnetic fields, *Adv. Space Res.*, 12, 265–279.
- Moore, T. E., and D.C. Delcourt (1995), Large-scale structure of magnetospheric plasma, *Surveys in Geophysics*, 16, 363–387.
- Moore, T. E., et al. (2005), Plasma sheet and (nonstorm) ring current formation from solar and polar wind sources, *J. Geophys. Res.*, 110, A02210, doi:10.1029/2004JA010563.
- Moore, T., R. Arnoldy, J. Feynman, and D. Hardy (1981), Propagating substorm injection fronts, *J. Geophys. Res.*, 86(A8), 6713–6726.
- Moore, T.E., et al. (1999) Ionospheric mass ejection in response to a CME, *Geophys. Res. Lett.*, 26, 2339.
- Moos, W., K. Sembach, and L. Bianchi (1997), Far Ultraviolet Astronomy and Origins: The FUSE Mission, *APS Conf. Series*, 148, 304.
- Morse, J.A., et al. (1998), Performance overview and science goals of the Cosmic Origins Spectrograph for the Hubble Space Telescope, *Proc. SPIE*, 3356, 361–368.
- Nakamura, R., et al. (2002), Fast flow during current sheet thinning, *Geophys. Res. Lett.*, 29 (23), 2140, doi:10.1029/2002GL016200.
- Ogilvie, G.I., and D.N.C. Lin (2004), Tidal dissipation in rotating giant planets, *Astrophysical Journal*, 610, 477–509.
- Owocki, S.P. (1990), Winds from hot stars, *Rev. in Mod. Astron.*, 3, 98–123.
- Parker, E.N. (1958), Dynamics of the interplanetary gas and magnetic fields, *Astrophysical Journal*, 128, 664.
- Parker, E.N. (1960), The hydrodynamic theory of solar corpuscular radiation and stellar winds, *Astrophysical Journal*, 132, 821.
- Parks, G.K. (2004), *Physics of Space Plasmas*, Westview Press.
- Peterson, W.K., H.L. Collin, M. Boehm, A.W. Yau, C. Cully, and G. Lu (2002), Investigation into the spatial and temporal coherence of ionospheric outflow of January 9–12, 1997, *J. Atmos. Sol. Terr. Phys.*, 64, 1659.
- Prangé, R. (1992), The UV and IR Jovian aurorae, *Adv. Space Res.*, 12, 379–389.
- Prangé, R., et al. (1998), Detailed study of FUV Jovian auroral features with the post-COSTAR HST faint object camera, *J. Geophys. Res.*, 103, 20195–20216.

- Rasio, F.A., et al. (1996), Tidal decay of close planetary orbits, *Astrophysical Journal*, 470, 1187.
- Rego, D., R. Prangé and L. Ben Jaffel (1999), Auroral Lyman  $\alpha$  and H<sub>2</sub> bands from the giant planets 3. Lyman  $\alpha$  spectral profile including charge exchange and radiative transfer effects and H<sub>2</sub> color ratios, *J. Geophys. Res.*, 104, 5939–5954.
- Richard, R.L., R.J. Walker, and M. Ashour-Abdalla (1994), The population of the magnetosphere by solar winds ions when the interplanetary magnetic-field is northward, *Geophys. Res. Lett.*, 21, 2455–2458.
- Rikken, G.L.J.A. and E. Raupach (2000), Enantioselective magnetochiral photochemistry, *Nature*, 405, 932–935.
- Rochette, P. (2001), Magnetism and the putative early Martian life, *Exo-/astro-biology: Proceedings of the First European Workshop*, 203–206.
- Rodriguez-Merino, L.H., et al. (2005), UVBLUE: A new high-resolution theoretical library of ultraviolet stellar spectra, *Astrophysical Journal*, 626, 411–424.
- Roeder, J.L., et al. (1996), CRRES observations of the composition of the ring-current ion populations, *Adv. Space Res.* 17, (10)17–(10)24.
- Sanchez-Lavega, A. (2004), The magnetic field in giant extrasolar planets, *Astrophysical Journal*, 609, L87–L90.
- Sano, Y. (1993), The magnetic fields of the planets: a new scaling law of the dipole moments of the planetary magnetism, *J. Geomag. Geoelectr.*, 45, 65.
- Sarris, T.E., X. Li, N. Tsaggas, and N. Paschalidis (2002), Modeling energetic particle injections in dynamic pulse fields with varying propagation speeds, *J. Geophys. Res.*, 107(A3), 1033, doi:10.1029/2001JA900166.
- Scharf, C.A. (2006), The potential for tidally heated icy and temperate moons around exoplanets, *Astrophysical Journal*, 648, 1196–1205.
- Schmitt, J.H.M.M. and C. Liefke (2004), NEXXUS: A comprehensive ROSAT survey of coronal X-ray emission among nearby solar-like stars, *Astronomy and Astrophysics*, 417, 651–665.
- Schneider, J. (2006), The extrasolar planets encyclopedia, <<http://exoplanet.eu>>
- Seager, S. and D. Sasselov (1998), Extrasolar giant planets under strong stellar irradiation, *Astrophysical Journal*, 502, L157.
- Sembach, K.R., et al. (2003), “Cosmic Origins Spectrograph Instrument Mini-Handbook”, Version 2.0, Baltimore: STScI.

- Shay, M.A., J.F. Drake, R.E. Denton, and D. Biskamp (1998), Structure of the dissipation region during collisionless magnetic reconnection, *J. Geophys. Res.*, *103*, 9165–9176.
- Sheldon, R., and D. Hamilton (1993), Ion transport and loss in the Earth's quiet ring current, 1. Data and standard model, *J. Geophys. Res.*, *98(A8)*, 13491–13508
- Shelley, E., R. Johnson, and R. Sharp (1972), Satellite observations of energetic heavy ions during a geomagnetic storm, *J. Geophys. Res.*, *77(31)*, 6104–6110.
- Shelley, E.G. (1985), Circulation of energetic ions of terrestrial origin in the magnetosphere, *Adv. Space Res.* *5(4)*, 401–410.
- Stern, S.A. (1999), Studies of comets in the ultraviolet: the past and the future, *Space Sci. Rev.*, *90*, 355–361.
- Stevens, I.R. (2005), Magnetospheric radio emission from extrasolar giant planets: The role of the host stars, *Mon. Not. R. Astron. Soc.*, *356*, 1053.
- Stevenson, D.J. (1983), Planetary magnetic fields, *Rep. Prog. Phys.* *46*, 555–557.
- Stevenson, D.J. (2001), Mars' core and magnetism, *Nature*, *412*, 214–219.
- Stevenson, D.J. (2003), Planetary magnetic fields, *Earth and Plan. Sci. Letters*, *208*, 1–11.
- Su, Y.-J., et al. (1998), Polar wind survey with Thermal Ion Dynamics Experiment/Plasma Source Instrument suite aboard Polar, *J. Geophys. Res.*, *103(A12)*, 29,305–29,337.
- Thomsen, M., et al. (2001), Two-satellite observations of substorm injections at geosynchronous orbit, *J. Geophys. Res.*, *106(A5)*, 8405–8416.
- Udry, S., D. Fischer and D. Queloz (2007), A decade of radial-velocity discoveries in the exoplanet domain, *Protostars and Planets V*, *951*, 685–699.
- Vidal-Madjar, A., et al. (2003), An extended upper atmosphere around the extrasolar planet HD209458b, *Nature*, *422*, 143–146.
- Vidal-Madjar, A., et al. (2004), Detection of oxygen and carbon in the hydrodynamically escaping atmosphere of the extrasolar planet HD 209458b, *Astrophysical Journal*, *604*, L69.
- Vogiatis, I.I., et al. (2011), THEMIS observations of earthward convected flux ropes triggering field dipolarization/substorm expansion and associated particle energization, *Ann. Geophys.*, *29*, 2117–2130.
- Waite, J.H., et al. (1983), Electron precipitation and related aeronomy of the Jovian thermosphere and ionosphere, *J. Geophys. Res.*, *88*, 6143–6163.
- Waite, J.H., et al. (2001), An auroral flare at Jupiter, *Nature*, *410*, 787–789.

- Walsh, J. (2006), Hubble news update, *Space Telescope European Coordinating Facility Newsletter*, 40, p.2
- Weaver, J.C., T.E. Vaughan T.E. and R.D. Astumian (2000), Biological sensing of small field differences by magnetically sensitive chemical reactions, *Nature*, 405, 707–709.
- Williams, D. (1987), Ring current and radiation belts, *Rev. Geophys.*, 25(3), 570–578.
- Williams, D. J. (1985), Dynamics of the Earth's ring current: Theory and observation, *Space Sci. Rev.*, 42, 375–396.
- Winglee, R. (1998), Multi-fluid simulations of the magnetosphere: The identification of the geopause and its variation with IMF, *Geophys. Res. Lett.*, 25(24), 4441–4444.
- Winglee, R.M. (2003), Circulation of ionospheric and solar wind particle populations during extended southward interplanetary magnetic field, *J. Geophys. Res.*, 108(A10), 1385, doi:10.1029/2002JA009819, 2003.
- Winglee, R.M. (2004), Ion cyclotron and heavy ion effects on reconnection in a global magnetotail, *J. Geophys. Res.*, 109, A09206, doi:10.1029/2004JA010385.
- Winglee, R.M., D. Chua, M. Brittnacher, G.K. Parks, and G. Lu (2002), Global impact of ionospheric outflows on the dynamics of the magnetosphere and cross-polar cap potential, *J. Geophys. Res.*, 107(A9), 1237, doi:10.1029/2001JA000214.
- Winglee, R.M., G.A. Dulk G.A. and T.A. Bastian (1986), A search for cyclotron maser radiation from substellar and planet-like companions of nearby stars, *Astrophysical Journal*, 309, L59.
- Winglee, R.M., E. Harnett, and A. Kidder (2009), Relative timing of substorm processes as derived from multifluid/multiscale simulations: Internally driven substorms, *J. Geophys. Res.*, 114, A09213, doi:10.1029/2008JA013750.
- Winglee, R.M., S. Kokubun, R.P. Lin, and R.P. Lepping (1998), Flux rope structures in the magnetotail: Comparison between Wind/Geotail observations and global simulations, *J. Geophys. Res.*, 103, 135–150.
- Winglee, R.M., W.K. Peterson, A.W. Yau, E. Harnett, and A. Stickle (2008), Model/data comparisons of ionospheric outflow as a function of invariant latitude and magnetic local time, *J. Geophys. Res.*, 113, A06220, doi:10.1029/2007JA012817.
- Wolszczan, A. (1994), Confirmation of Earth-mass planets orbiting the millisecond pulsar PSR B1257+12, *Science*, 264, 538–542.
- Woo, R. (1977), Measuring solar wind velocity with spacecraft phase scintillations, *Nature*, 266, 514.

- Wood, B.E., H.-R. Muller, G.P. Zank, and J.L. Linsky J.L. (2002), Measured mass-loss rates of solar-like stars as a function of age and activity, *Astrophysical Journal*, *574*, 412–425.
- Yau, A., E. Shelley, W. Peterson, and L. Lenchyshyn (1985), Energetic auroral and polar ion outflow at DE 1 altitudes: Magnitude, composition, magnetic activity dependence, and long-term variations, *J. Geophys. Res.*, *90(A9)*, 8417–8432.
- Yau, A.W., and M. Andre (1997), Sources of ion outflow in the high latitude ionosphere, *Space Sci. Rev.*, *80*, 1–25.
- Yelle, R.V. (2004), Aeronomy of extra-solar giant planets at small orbital distances, *Icarus*, *170*, 167–179.
- Zhu, Z.W., and R.M. Winglee (1996), Tearing instability, flux ropes, and the kinetic current sheet kink instability in the Earth's magnetotail: A three-dimensional perspective from particle simulations, *J. Geophys. Res.*, *101*, 4885–4897.

**VITA**

Michele Diane Cash

Bachelor of Science in Physics  
Stanford University  
June 2004

Master of Science in Geophysics  
University of Washington  
August 2006

Doctor of Philosophy  
University of Washington  
June 2012